Dynamic Stall of a NACA 0012 Airfoil in Laminar Flow

by

Sasi K. Digavalli

Submitted to the Department of Aeronautics and Astronautics
in partial fulfillment of the requirements for the degree of

Doctor of Philosophy

at the

MASSACHUSETTS INSTITUTE OF TECHNOLOGY

September 1993 (February 1994)

Signature of Author ... .
Department of Aeronautics and Astronautics
September 2, 1993

Certified by . .....
James E. McCune
Professor
Thesis Supervisor

Certified by .. ..
Eugene E. Covert
Professor
Thesis Supervisor

Certified by .. ..
Mårten T. Landahl
Professor
Thesis Supervisor

Certified by .. ..
R. John Hansman, Jr.
Associate Professor
Thesis Supervisor

Accepted by..... .....
Professor Harold Y. Wachman
Chairman, Department Graduate Committee

Dynamic Stall of a NACA 0012 Airfoil in Laminar Flow

by

Sasi K. Digavalli

Submitted to the Department of
Aeronautics and Astronautics
on September 28, 1993, in partial fulfillment of the
requirements of the Degree of

Doctor of Philosophy

Abstract

The dynamic stall processes of a NACA 0012 airfoil oscillating sinusoidally in pitch and heave in laminar incompressible flow were investigated. The effects of changing the reduced frequency k from 0.6 to 1.2 and the pivot location x_0/c from 1/4 to 3/4 were calculated. The nominal angle of incidence on the airfoil oscillated between 6° and 18° about a mean of 12°.

The incompressible and inviscid external flow around the body was calculated using unsteady Bernoulli and a conformal transformation. The unsteady boundary layers were analyzed by C.C. Lin's asymptotic method applicable when the reduced frequency is "large". An unsteady separation condition, consistent with the Moore-Rott-Sears separation criterion, developed by A. Gioulekas as an extension of Stratford's separation condition for steady flows, was used to calculate the separation points of the boundary layers. The separated free shear layers were represented by discrete vortices. Each vortex was convected force-free (in the inertial frame) throughout the calculation by using the Biot-Savart law.

In all of the calculations we performed, the pressure surface separation point does not move from the trailing edge. For $k = 0.6$ and $x_0/c = 0.5$, as the airfoil pitches up from $\alpha = 6°$, the suction surface separation point remains in the vicinity of the trailing edge until the airfoil attains an angle (14°) well above its static stall angle (12°). It then moves rather abruptly to within 19% of the chord from the leading edge. At this time ($\alpha = 17°$) the separated shear layer starts to roll-up to form a large "primary" vortex. The lift on the airfoil increases monotonically to $C_L = 1.6$ until the airfoil reaches its maximum nominal incidence. The vortex grows to a strength $\frac{\Gamma_{p.v.}}{Uc} = 0.7$ by the time the airfoil pitches down to $\alpha = 17.4°$ when the pitching moment on the airfoil attains a large nose-up value. At this time the vortex detaches from its feeding sheet and drifts downstream at 42% of the freestream speed. As the vortex moves downstream i t carries

with it an intense low pressure region, which helps the airfoil maintain a large C_L even when it is pitching down. As the vortex approaches the trailing edge, the airfoil briefly experiences a nose-up moment of significant magnitude.

As the reduced frequency was increased to 0.9 and 1.2, the upstream propagation of the suction surface separation point is delayed (in angular sense) and the slope of the $C_L - \alpha$ curve increased when the airfoil pitches nose-up. As the airfoil approaches its maximum nominal incidence, the abruptness with which the separation moves towards the leading edge increased. The separation point reached closer to the leading edge, $C_{L_{max}}$ increased and the inception of the primary vortex is delayed (in angular sense). The strength of the vortex and its dwell time (in angular sense) increased while its average streamwise drift speed decreased. During the nose-down pitch, the separation point retreated at a slower rate. The pitching moment at the beginning of the cycle ($\alpha = 6°$) changed from a small nose-up value to a larger nose-down value, mostly due to apparent mass effects. The apparent mass effect on C_m at the top of the cycle ($\alpha = 18°$) is not so significant because of the proximity to leading edge of the dominant primary vortex and its movement.

The primary effect of moving the pivot towards the trailing edge is a delay in the onset of dynamic stall. The upstream movement of the separation point and the time of inception of the primary vortex are delayed. The slope of $C_L - \alpha$ curve, the maximum velocity attained near the leading edge and the $C_{L_{max}}$ decreased. The maximum penetration of the separation point towards the leading edge also decreased. The dwell time of the primary vortex near the leading edge is not altered significantly. Its maximum strength decreased while its average speed increased. Some of these effects of moving the pivot point and increasing k can qualitatively be forecast by analyzing the results from linear potential theory. Such an analysis leads to the definition of "effective angle of incidence".

Dynamic stall characteristics of a heaving airfoil emulated some of the features of dynamic stall of a pitching airfoil with a rearward-pivot. Namely, upstream movement of the separation point and the inception of the primary vortex are delayed. The process of stall is less abrupt on a heaving airfoil than on a pitching airfoil with a forward pivot. The $C_{L_{max}}$ and the strength of the primary vortex are both smaller. Some of these effects can also be deduced from an analysis of the simple linear potential theory. The effects of increasing the reduced frequency on the dynamic stalling of a heaving airfoil are similar to those on pitching airfoils.

Thesis Supervisor: James E. McCune

Title: Professor of Aeronautics and Astronautics

Acknowledgements

I am grateful to Professor McCune for providing me with constant guidance, his unique insights into fluid mechanics and most of all for standing by me through out the course of this research. Without his support and unfailing faith in me, I would not have been able to complete this work. I have learned a great deal about teaching while I was a teaching assistant for him.

I am thankful to Prof. Covert for offering, what have proved to be extremely useful ideas and criticism to my research. I thoroughly enjoyed being a teaching assistant to him and learned more about teaching.

I am thankful to Prof. Landahl for teaching me a lot of fluid mechanics during this research and in several courses.

I am also thankful to Prof. Hansman for taking an active interest in my research and giving useful suggestions. Thanks are also due to Prof. Drela for acting as my thesis reader and for occassional but useful discussions.

I am thankful to Gioulekas, my friend and colleague, for letting me use his ideas and work, which formed the basis for our research.

I am deeply indebted to my parents Gadi Subbayamma and Digavalli Suryaprakasa Rao, and grand mother Gadi Sita Mahalakshmi, for teaching what is right and wrong and for keeping me fed and clothed in spite of overwhelming odds.

During this long stay at M.I.T., I have come across some of the most wonderful people on Earth. First and foremost among them is my fiancee Carol Boyer, who has been a source of happiness, satisfaction and inspiration ever since I have known her.

Dear to my heart also are: Gus, Kathy, Bhat, Nanthi, Ranga, Diana, Ron, Jihad, Vishak, Christina, Vasuki and Mel.

I am also thankful to many of my past and present officemeates for sharing their knowledge with me and for generally being helpful.

Nomenclature

b	semi-chord of airfoil
c	length of airfoil chord
C_L	lift coefficient
$C_{L_{max}}$	maximum C_L attained during an oscillation
C_m	pitching moment coefficient about quarterchord
C_p	pressure coefficient
F	complex flow potential
h	heaving displacement of the airfoil
$\dot{h}$	heaving velocity of the airfoil
k	reduced frequency
l_{pitch}	sectional lift on a pitching airfoil
l_{heave}	sectional lift on a heaving airfoil
M, M_∞	freestream Mach number
$\vec{n}$	outward normal to the body surface
p	pressure
p_∞	freestream pressure
$\vec{q}$	velocity vector
$\vec{q}_\infty$	freestream velocity vector
r_c	radius of core of a discrete Rankine vorex
$\vec{R}$	position vector w.r.t. inertial frame
$\vec{R}_0$	displacement vector of body fixed frame from inertial frame
Re, Re_c	Reynolds number based on chord $=\frac{Uc}{\nu}$
Re, Re_δ	Reynolds number based on boundary layer thickness $=\frac{U\delta}{\nu}$
t	time
u, v, w	velocities in inertial frame or within a boundary layer
u_p, v_p	Prandtl component of boundary layer velocities
$\bar{u}_p, \bar{v}_p$	averaged Prandtl velocities
$\tilde{u}_p, \tilde{v}_p$	fluctuating Prandtl velocities
u_s, v_s	Stokes component of boundary layer velocities
$\bar{u}_s, \bar{v}_s$	averaged Stokes velocities
$\tilde{u}_s, \tilde{v}_s$	fluctuating Stokes velocities
U, U_∞	freestream velocity
U_p, V_p	Prandtl components of external velocity
U_s, V_s	Stokes components of external velocity
$\vec{v}$	velocity on the body surface in inertial frame

w	conjugate of complex velocity in airfoil plane
w_∞	conjugate of complex freestream velocity in airfoil plane
x, y, z	coordinates in body fixed frame
$\acute{x}, \acute{y}, \acute{z}$	coordinates in alternate inertial frame
x_s, y_s	location of separation point
X, Y, Z	coordinates in inertial frame
x_0	distance of pivot point from leading edge
(X_0, Y_0, Z_0)	$= \vec{R_0}$
$z = x + iy$	coordinates in airfoil plane

α	nominal instantaneous angle of incidence
$\dot{\alpha}$	time rate of change of α
$\ddot{\alpha}$	angular acceleration with respect to time
$\bar{\alpha}$	average angle of incidence
$\tilde{\alpha}$	amplitude of oscillation in angle of incidence
α_{eff}	effective angle of incidence on a pitching airfoil
α_{eq}	equivalent angle of incidence on a heaving airfoil
δ	a measure boundary layer thickness
δ_p	a measure of Prandtl layer thickness
δ_s	a measure of Stokes layer thickness
Δt	time-step in numerical scheme
η	coordinate in circle plane
$\eta(x, y, t)$	body surface in body fixed coordinates
ϵ	$\pi\epsilon$ is the trailing edge angle
Γ	circulation of a vortex or in a boundary layer
$\dot{\Gamma}$	flux of circulation
Γ_b	instantaneous bound circulation
Γ_j	circulation of j-th vortex
Γ_0	initial bound circulation
$\Gamma_{p.v}$	circulation of the primary vortex
Γ_w	wake circulation
λ	shifted drift time of a wake element
ϕ	flow potential in body fixed frame
ϕ, ψ, θ	angular position vector of body fixed frame w.r.t. inertial frame
$\dot{\phi}, \dot{\psi}, \dot{\theta}$	angular velocity of body fixed frame w.r.t. inertial frame

Φ flow potential in inertial frame

ω angular rate of change of α or vorticity or angle in circle plane

Ω vorticity

$\vec{\Omega}$ $= (\dot{\phi}, \dot{\psi}, \dot{\theta})$

ρ density of the medium of flight

τ nondimensional time $= \frac{Ut}{c}$ or drift time of a wake element

θ angle in airfoil plane

$\vec{\Theta}$ $= (\phi, \psi, \theta)$

ξ coordinate in circle plane

ζ complex coordinate in circle plane

ζ_j complex coordinate of j-th vortex in circle plane

$\zeta^\star$ complex conjugate of ζ in circle plane

Contents

List of Figures

Chapter 1

Introduction

1.1 What is Dynamic Stall ?

An airfoil oscillating rapidly in pitch or plunge experiences peculiar hysteresis in lift, drag and moment. While executing such a motion, if the angle of incidence of the airfoil exceeds the static stall angle, large gains in lift associated with similarly large increases in drag and negative (nose up) moments are observed. The disparities in the time scales associated with inviscid and viscous phenomena permit a delay of flow separation and an aerodynamic lift temporarily higher than that in the static stall situation. This complex unsteady flow process is referred to in general as dynamic

stall.

Dynamic stall is of importance in various aerodynamic applications including helicopter rotors, aircraft engines, wind turbines and rapidly maneuvering aircraft.

Experiments and some numerical investigations have provided a great deal of information on the flow events which occur during dynamic stall, including their effects on resulting transient aerodynamic forces. Despite this progress, the underlying physical mechanisms which produce the observed unsteady flow behavior are not yet sufficiently understood.

Further advances in understanding and prediction of dynamic stall are hindered not only by the inherent complexity of the flow but also by the many interrelated flow effects. For example, experimental investigations conducted under different conditions by varying Reynolds number, airfoil geometry, incidence angle, oscillation mode, oscillation rate, oscillation amplitude and Mach number have revealed that all of the above flow parameters influence the dynamic stall characters.

Flow phenomena such as unsteady separation, shear layer instability, shock-boundary layer interaction and the interaction of vortical structures with one another and with the airfoil occur during dynamic stall.

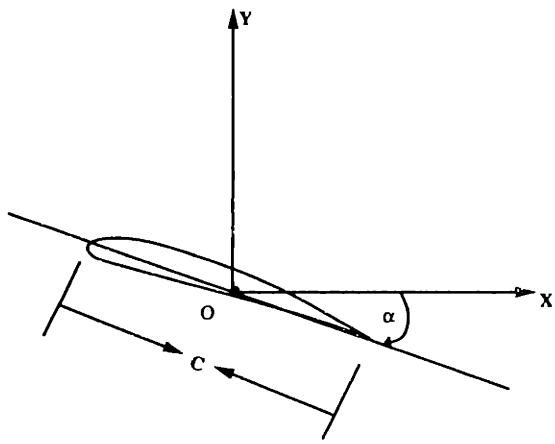

Figure 1.1: Definition of Reduced Frequency.

1.2 Reduced Frequency

1.2.1 Definition

For the case of an airfoil of chord c, pitching as illustrated in Fig. 1.1, say about its midchord, at a constant rate $\dot{\alpha}$ in a uniform stream of speed U, the flow is characterized by a nondimensional pitch rate parameter $k = \dot{\alpha}c/2U$, in addition to Reynolds number and Mach number.

The pitch rate parameter arises from the nondimensionalization of the velocities on the boundary of the airfoil when viewed from an inertial frame. In a frame rotating

with the airfoil the reduced frequency would be proportional to the inverse of the Rossby number which arises out of nondimensionalization of the fictitious body forces appearing in the rotating frame. The interpretation of the pitch rate parameter most useful for our purposes is what gives it the name "reduced frequency". The reduced frequency is the ratio between the convective time scale c/U and the time scale of the forced oscillation $1/\dot{\alpha}$.

Thus when $k\sim1.0$, the convective and unsteady (airfoil motion) time scales are of the same order and the flow is unsteady as far as convective (*i.e.*, such as inviscid or potential) phenomena are concerned.

In some practical cases $k\sim0.05$. Such flows are quasi steady from the convective point of view. Yet, even at these low values of the reduced frequency, significant differences between dynamic and static stall characteristics exist. The source of these differences lies in the large time scales associated with viscous phenomena. Even when an airfoil in unsteady motion does not approach static stall parameters, significant differences between static and dynamic characteristics should be expected, because in most of the flows we call inviscid, the primary effect of viscosity is locked in through the imposition of Kutta condition.

The ratio of the diffusion time to convection time is, as we know, Re_c, based on chord. Then the ratio between the viscous diffusion time scale and the airfoil motion time

scale is kRe_c. The ratio between the corresponding length scales is $k\sqrt{Re_c}$ or kRe_δ where δ is a measure of the boundary layer thickness. Even when $k \simeq 0.01$, both of the above ratios are ≥ 1.0 making the flow necessarily unsteady from viscous perspective.

The dynamic stall problems encountered more often in practice are those that involve periodic oscillations of an airfoil (wing) in pitch and heave rather than constant rate pitch. The airfoil oscillating sinusoidally in pitch will have an instantaneous "nominal" angle of attack[1] given by

$$\alpha(t) = \bar{\alpha} + \tilde{\alpha} \sin \omega t$$

where $\bar{\alpha}$ is the mean angle of attack, $\tilde{\alpha}$ is the magnitude of oscillation and ω is the angular rate of oscillation. For such pitching motions the reduced frequency is usually defined as $k = \omega c/2U$.

The nondimensional pitch-axis location x_0/c, where x_0 is the distance of the pitch-axis from leading edge, is an important geometric parameter for a given airfoil. The velocity of the leading edge relative to the external fluid would be much larger, for the same pitch rate, as the distance between the location of the pitch-axis and the leading edge increases. Thus the leading edge of an airfoil should be expected to experience a "stronger" unsteadiness when the pitch-axis is at midchord than when the pitch-axis is at, say quarterchord.

[1] Please see chs. 5&7 for a discussion on "effective" angle of attack in pitching oscillations.

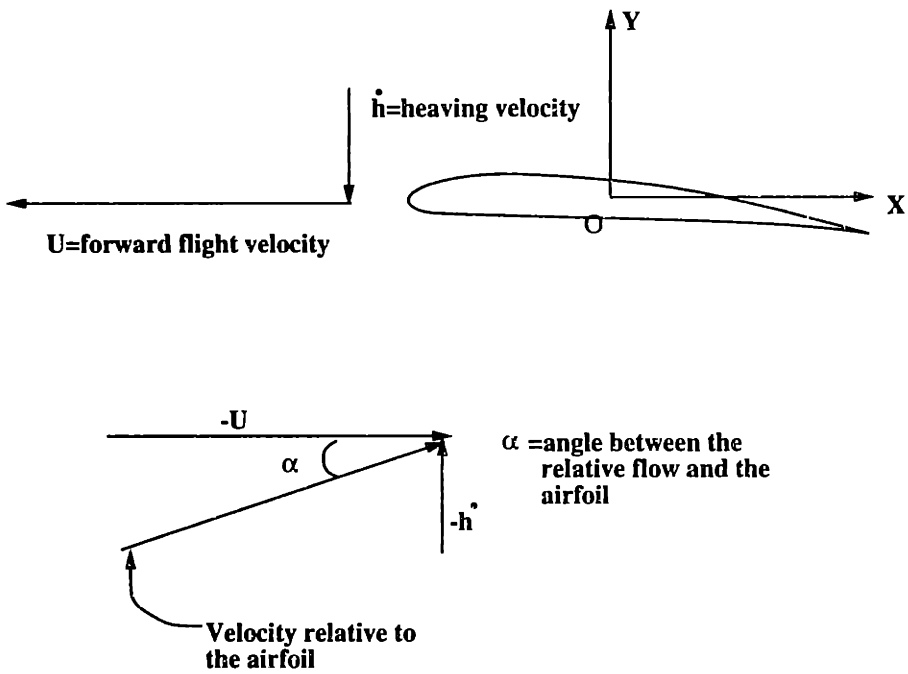

Figure 1.2: Angle Between Relative Flow and a Heaving Airfoil.

The case when $x_0/c \rightarrow \pm\infty$ corresponds to heaving motion. An airfoil oscillating in heave in an otherwise steady freestream would see, as shown in Fig. 1.2, a freestream oscillating in direction (thus in "relative" angle of attack[2]) and magnitude, at the same frequency. Thus, an airfoil oscillating in heave can undergo dynamic stall if the heave is rapid "enough". The reduced frequency for a heaving oscillation is defined in the same way as in the case of a pitching oscillation. Thus, for an airfoil of chord c, heaving at an angular rate ω in an otherwise steady freestream of magnitude U, the reduced frequency is given by $k = \omega c/2U$.

1.2.2 Relevant Range of Reduced Frequency

In this section we will make estimates of reduced frequencies relevant to gas turbine blades, helicopter blades and rapidly maneuvering aircraft.

Consider a typical low speed axial flow engine with an inlet speed of 100m/s, rotational speed of 10,000 rpm, 60 blades in a rotor and 5cm rotor blade chord. The highest frequency unsteadiness felt by a blade (discarding random noise and structural vibrations) in a stator row is that due to the periodic passing of the rotor blades (potential effects and also wake impingement effects). The reduced frequency (ratio between the convective and unsteady time scales) for this case is roughly 6.

[2]Please see chs. 6&7 for a discussion on "effective" angle of attack in heave.

Consider now a helicopter flying at 100 miles/hr. with a rotor rotating at 1,000 rpm. Let the rotor blade have an average chord of 20cm and length of 3m. In this case, the unsteadiness associated with wake chopping is roughly 0.2 and the unsteadiness due to periodic forward and backward sweeping is 0.5.

Finally let us look at a plane with 2m wing-chord, flying at 100 m/s and executing a 60° nose-up maneuver in 1s. The reduced frequency for this maneuver is around 0.05.

It is thus clear that practical applications span a wide range of reduced frequency between ten and zero.

1.3 Literature Survey

The phenomena associated with dynamic stall were first reported in the early fifties by Halfman, Sisto, Rainey, *et. al.* [32, 78, 66]. These studies grew out of stall flutter research on helicopter and aircraft engine blades. From these works the stall flutter mechanism of negative damping, or moment variation so that energy is extracted from the flow, was deduced. Liiva, et al. [49] conducted extensive tests on two-dimensional airfoils pitching and heaving sinusoidally through stall. Both lift overshoot, or lift in excess of maximum static value, and unstable moment variation were found to be

strong functions of frequency, amplitude, mean incidence and Mach number.

In the late sixties and early seventies dynamic stall, by then well recognized, received renewed attention from Ham, Garrelick, Crimi, Carta, Ericcson, Reding, McCroskey and others [34, 16, 12, 18, 54]. Ericcson and Reding [18] employed a quasi-steady approach which uses measured static airfoil characteristics. This approach and some of the concepts proposed by Ericcson and Reding such as "Moving Wall Effect" raised some controversy and are not currently pursued by many researchers. Carta [12] used energy considerations and data from tests of his own and others on two-dimensional oscillating airfoils to analyze stall flutter of rotor blade. Crimi [16] numerically determined the separation points in the boundary layers on two-dimensional airfoils and then used a panel method to model the evolution of the wakes. Ham [34] analyzed analytically a two-dimensional model consisting of discrete vortices shed from both the leading and trailing edges. Ham also conducted experiments on oscillating airfoils that led to stall flutter analysis. McCroskey and Carr [54, 10] concentrated on experimental studies of various airfoil geometries and provided information on flow properties leading to "leading edge stall" and "trailing edge stall". Lorber [51, 52] calculated the dynamic stall characteristics of slender wings and also the effects of Reynolds number on dynamic stall.

Several experimental investigations of dynamic stall at low Reynolds number for airfoils pitching at constant and sinusoidally varying rates have been conducted during

the last decade.

Smoke visualization studies were done on a NACA 0015 airfoil for a range of reduced frequency values and pivot axis locations by Helin and Walker [35] and Walker [89]. Strickland [80] provided surface pressure distributions and force coefficients for an airfoil pitching at rates up to $k = 0.3$. Flow visualizations were also presented by Freymuth [23] who used an innovative vortex tagging technique. Koochefsahani [42] and Acharya [2] also conducted flow visualization experiments and compiled information about the surface vorticity flux and the effects of pitch acceleration $\ddot{\alpha}$. McCroskey, et al. [55] conducted oil-flow visualization experiments on NACA 0012 airfoils. By varying the leading edge profile, three different types of dynamic stall were produced. Vortex shedding "phenomenon" was found to be the predominant feature of each. Vaczy [86] studied the effects on a NACA 0012 airfoil due to a rotating elliptic cylinder placed behind the airfoil in turbulent flow. Stalling behavior of the airfoil at reduced frequencies upto 6 was studied.

The above experimental investigations have provided, by means of flow visualization and pressure measurements, a great deal of information about the sequence of events which characterize the dynamic stall process, as well as their timing and their effect on the aerodynamic coefficients. However, the lack of experimental velocity measurements impairs our ability to understand more completely the underlying physical mechnanisms of unsteady stall, in particular the process by which the distributed

vorticity in the shear layer evolves into coherent vortical structures.

It should be remembered, as pointed out by Ericcson [21], that results from experiments on scaled models can be misleading when extrapolated to full scale vehicles due to the different scaling effects of Reynolds number and reduced frequency[3].

In an effort to describe the complete flow field including the velocities and pressures and the variation with time of these features as the unsteady stall proceeds, computational investigations were undertaken by several researchers. Most of these were costly and time consuming Navier-Stokes solvers [93, 87, 28, 69, 59]. Visbal and Shang [88], Mehta [59], Wu, et al. [93] and Rumsey and Anderson [69] simulated the flow over a NACA 0015 airfoil pitching at a constant rate by solving the full Navier-Stokes equations. Mehta [59] solved the Navier-Stokes equations to simulate the leading edge bubble. Though he could model the growth of the bubble successfully, his code did not capture accurately the "bursting" of the bubble and the initial stages of the vortex sheet evolution. Ono [64] and Geissler [26] included turbulence models in their calculations. Many of the above authors reported qualitative agreement between results from their calculations and experiments. McCroskey and Philippe [56] investigated numerically and experimentally the differences between laminar and turbulent flows over flat plates at several frequencies. They reported having observed important dif-

[3] $Re = Uc/\nu$, $k = \omega c/2U$; If the size of a model is chosen so that k would be the same for the model and the full scale object, then the Reynolds number would be differenrt and vice versa.

ferences (mentioned above) between the two flows and the failure of their numerical scheme to capture these features.

Based on limited comparisons with experimental results, some of the numerical simulations have given satisfactory predictions for such global properties of the flow field as lift, drag, etc. But the simulations have not performed as well when applied to a diversity of problems or when tested for such local properties of the flow field as the exact location of separation, secondary separation, etc.

Semi-analytical methods, though unable to simulate some of the flow features, are more amenable to validation, less uncertain and most importantly, provide insights into the physics of the flow.

Some authors attempted potential external flow calculations coupled with boundary layer analysis or imposed leading edge separation [16, 65, 34] with varying degree of success. In addition to Ham [34] and Crimi [16] as mentioned above, Patay [65] and Woods [92] are among them. Patay analyzed the unsteady boundary layer on a pitching airfoil and concluded that quasi-steady analysis was sufficient up to $k = 0.05$. Woods derived the unsteady load on an oscillating stalled airfoil with a prescribed separation point by extending the classical unsteady thin airfoil theory.

1.4 The Dynamic Stall Process

Let us now attempt to describe in sequential order the key flow features that make up the dynamic stall cycle, as it happens to be understood today. All the flow events are generally accepted and experimentally evidenced in the literature described above.

In most of the practical situations, the Reynolds number is large enough ($Re_c \geq 10^6$) to cause transition into turbulence at some location on the body surface. Nonetheless, much can be learned about the physical mechanisms of unsteady stall from careful studies in the low (laminar) Reynolds number ($Re \leq 10^5$) regime, since most of the basic features of dynamic stall are retained over a wide range of Reynolds number, in particular in laminar flow. Moreover, laminar flow studies are free of the uncertainties and emiricism associated with the turbulence modeling.

For experimental investigations, low speed flows are more amenable to flow visualization methods than are flows at higher speeds. Also, lower values of U permit studies at higher reduced frequencies. For computational investigations low speed flows require less resolution and are free of uncertainties associated with turbulence models.

In the following discussion we will concentrate mostly on studies of dynamic stall at low Reynolds number and zero Mach number, though the effects of transition

and compressibility are also visited. The discussion is applicable to an airfoil with a smooth leading edge pitching at $0.1 \leq k \leq 1.0$, with the pitching axis located aft of the leading edge and not too far behind the trailing edge. (When the pitch axis is located upstream of the leading edge, clockwise rotation will be associated with a decreasing angle of incidence and vice versa. If the pitch axis is located too far behind the trailing edge, the nature of the flow will be more like that during a heaving oscillation.) It is assumed that the maximum nominal angle of attack attained by the airfoil during the motion is above the steady state stall angle and the minimum angle attained is above zero.

1.4.1 Dynamic Stall at Laminar Reynolds Numbers

Consider now, an airfoil pitching about its midchord at a reduced frequency $k \simeq 0.3$. At minimum incidence, the flow displays a small trailing edge separation. As the airfoil pitches up (angle of attack increases), the boundary layer becomes fully attached on the airfoil lower surface, while on the upper surface the separation point moves upstream. A free shear layer wake forms at the trailing edge and a net positive (counterclockwise) vorticity is shed into the wake consistent with the increasing bound circulation on the airfoil. Please see Fig. 1.3 for a conceptual illustration of this process. During this phase of the oscillation, the separation position on the suction surface remains well downstream of the separation position on a quasi-steady airfoil

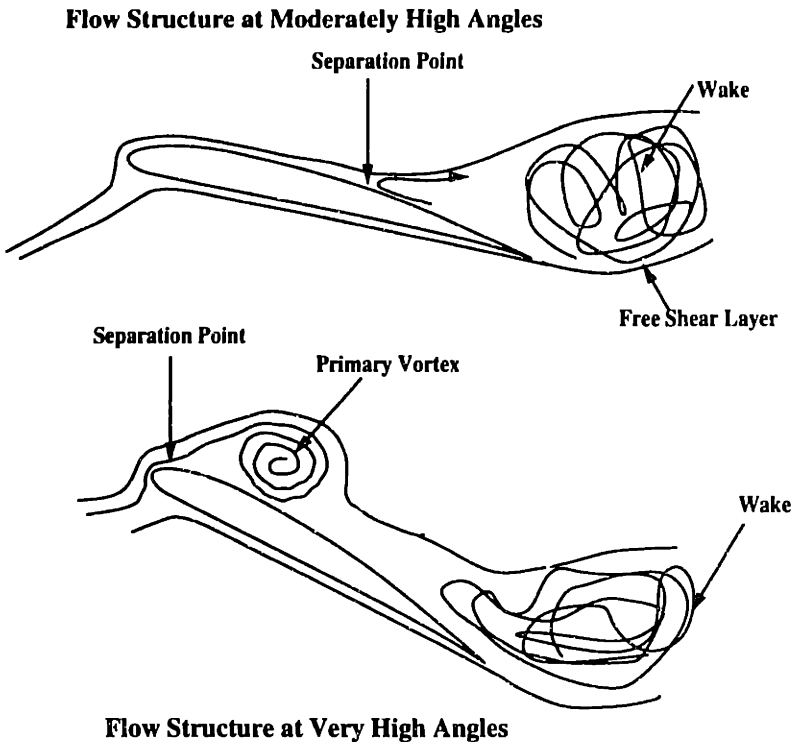

Figure 1.3: Flow Structure on an Airfoil Undergoing Dynamic Stall.

at the same nominal angle of incidence.

As the angle of attack is further increased, the separated region on the upper surface eventually spreads to the vicinity of the leading edge. The separated shear layer on the upper surface rolls-up, resulting in the formation of the "dynamic stall" or "primary" vortex. This process is also shown in Fig. 1.3. The dynamic stall vortex grows in size as it moves away from the airfoil surface and eventually detaches from its feeding sheet. During the same time, the free shear layer emanating from the trailing edge becomes more intense and in some cases rolls up to form a counterclockwise "trailing edge" vortex. The detachment of the primary vortex occurs shortly after the airfoil attains its maximum angle of attack. Then the vortex continues to move downstream.

As the airfoil pitches down (angle of attack decreases), the primary vortex moves farther downstream and the separation point on the upper surface moves back towards the trailing edge. Shortly after the airfoil commences downward pitching motion, the trailing edge vortex, if previously formed, detaches and drifts downstream.

The separation point of the upper surface reaches the proximity of the trailing edge well before the airfoil reaches the minimum incidence. By the time the airfoil reaches this incidence, both the primary vortex and the trailing edge vortex, if present, have drifted well into the downstream and shear layer of small negative vorticity is being

shed from the trailing edge.

1.4.2 Effects of Turbulence

The presence of turbulence can lead to different types of separation processes on the upper surface. But regardless of the specific separation process, the separated shear layer rolls-up to form the dynamic stall vortex in all cases and the subsequent events proceed in much the same way as in the case of laminar stall.

For very high Reynolds numbers the flow on airfoils with smooth leading edges separates at the trailing edge and propagates towards the leading edge. This situation is very similar to the laminar case, except that the boundary layer is turbulent and the propagation speed of the separation point is higher and becomes abrupt when the separation reaches the midchord. For slightly lower Reynolds numbers, but still larger than 10^6, most airfoils display a typical small leading edge laminar separation bubble, as shown in Fig. 1.4. The shear layer goes through transition and becomes turbulent before it reattaches to complete the bubble. Further downstream the turbulent boundary layer separates again. As the angle of attack is increased, the bubble grows only by a small amount due to the downstream movement of the reattachment point while at the same time the turbulent separation point moves upstream. In this case, though the separation bubble modifies the flow around the leading edge, it does

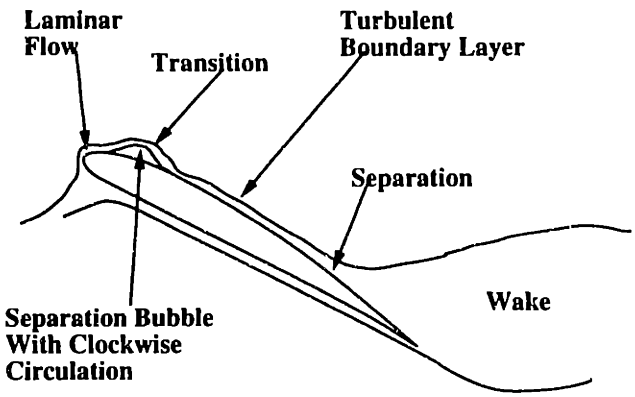

Figure 1.4: Formation of the Leading Edge Bubble on a Pitching Airfoil.

not alter the overall nature of the flow or the separation conditions significantly.

For Reynolds numbers around transition the flow is much more complex due to the presence of a large leading edge bubble which can grow to encompass a large fraction ($\sim$25%) of the chord. The bubble not only modifies the overall flow, but also controls the separation onset and the formation of the dynamic stall vortex. The formation, evolution and the subsequent "bursting" of the bubble have proven to be difficult to model both numerically and analytically. For a more complete discussion on the effects of turbulence on dynamic stall see McCroskey & Philippe [56] and Lorber & Carta [51, 52].

1.4.3 Effects of Compressibility

When the subsonic freestream Mach number and the angle of attack are increased beyond certain values, a local region of supersonic flow develops over the airfoil [63]. This supersonic region is usually terminated by a nearly normal shock wave which interacts with the boundary layer. For sufficiently strong shocks, boundary layer separation occurs at the foot of the shock and unsteady flow phenomena such as buffeting are initiated. These processes occur under similar conditions on oscillating airfoils also and make the calculation of the separation point and the evolution of the vortex sheet more complex.

A considerably less explored area of unsteady transonic flows pertains to airfoils in severe maneuvers. Even for M_∞ as low as 0.2, a temporary transonic/supersonic region can appear over a pitching airfoil. The maximum attainable lift and the static stall angle are reduced in transonic flows [1]. The magnitude of these effects depends on the airfoil geometry and the frequency and the magnitude of the oscillations of the airfoil motion [85].

A more comprehensive discussion on the effects of compressibility on dynamic stall can be found in [49, 70].

Many other factors, as mentioned in the first section of this chapter, such as the

geometry of the leading edge, rate, magnitude and mode of oscillation, location of the axis of pitch, etc. all affect the dynamic stall characters. Some of these are discussed in latter chapters.

1.5 Motivation for the Present Work

The literature survey presented above makes clear that despite the substantial progress made towards the understanding and prediction of dynamic stall, a lot remains to be done. Particularly the physical mechanisms producing dynamic stall are not clearly understood. Most of the methods available for calculating dynamic stall are expensive and time consuming Navier-Stokes solvers. These methods contain considerable uncertainty, numerical inaccuracies and empiricism. In addition, because of the several case-specific models contained in these solvers, many of them have proven to be inapplicable for problems of any considerable diversity.

Our aim has been to compute analytically (with the "assistance" of computer limited to solving simplified equations) the dynamic stall characters of two dimensional airfoils oscillating in both pitch and heave in a laminar flow at relatively high reduced frequencies. We have chosen to adopt analytical methods to model the flow so that considerable understanding of the flow physics may result from our work. As mentioned above laminar flows are more amenable to analytical methods than turbulent

flows. As noted in the previous section, though most real world flows are turbulent, laminar flows retain most of the important dynamic stall features and so the analysis of laminar flows can provide valuable information relevant for practical applications.

1.6 Synopsis of the Thesis

As mentioned earlier, the objective of our research has been to predict the Dynamic stall characteristics of two-dimensional airfoils executing large amplitude oscillations in pitch and heave. This required the calculation of the potential flow around the airfoil undergoing such a motion, locations of the unsteady separation points on the upper and lower surfaces of the airfoil, the subsequent evolution of the separated free vortex layer and the influence of the free vortex layers on airfoil circulation and separation points. We have chosen to use NACA 0012 in our calculations because of the availability of experimental data on NACA 0012 in literature for testing our method and comparing the results.

1.6.1 Potential Flow

First the unsteady potential flow on the airfoil is calculated assuming incompressible and inviscid ($Re \rightarrow \infty$) flow around the body. A modern variant of Theodorsen's [84]

transformation was used to transform the airfoil to a unit circle. Unsteady Bernoulli equation and a suitable body frame of reference were used for calculation of velocities and pressures on the body. In the first iteration the flow is assumed to be attached to the body. In the subsequent iterations, after the separation points are determined as explained below, the wake vortices and their images are included in the potential calculation.

1.6.2 Unsteady Boundary Layers and Separation

For the analysis of unsteady flow in the vicinity of the body, an asymptotic method developed by C.C. Lin and advanced by Gibson and Gioulekas [50, 29, 30] was used. This method is applicable in the asymptotic limit when a parameter proportional to the square root of the reduced frequency becomes large. Using this asymptotic expansion the boundary layer flow is separated into "Prandtl flow" and "Stokes flow" coupled through the wall boundary conditions. The expansion results in a set of simple equations which were solved to obtain the velocities in the boundary layer.

An unsteady separation criterion developed by [30], an extension of Stratford's [79] separation criterion for steady flows, was used to calculate the separation points in the boundary layers. This separation condition is consistent with the Moore-Rott-Sears [74] separation criterion and involves the identification of a saddle point in

the "Prandtl velocity" profile, viewed from a frame of reference moving with the separation point. It was shown by [30] that a local and instantaneous reversal in the direction of the Stokes component of the streamwise velocity does not indicate separation.

1.6.3 Convection of Shear Layers and Interaction with Airfoil

The separated boundary layers, *i.e.* free shear layers, are represented by discrete vortices. Each vortex is convected by the velocity imposed at its location by the airfoil and all other vortices and so all free vortices remain force free throughout the calculation. Thus the entire flow field is updated at each time step using the Biot-Savart law. This procedure results in new locations for the separation points and more amount of vorticity to be shed due to the changed bound circulation.

1.6.4 Results

First the method was validated by comparing our results to those from relevant experiments and calculations.

Then results for a NACA 0012 airfoil oscillating in pitch and heave are presented for

a range of reduced frequencies. The lift, drag and moment hysteresis characteristics were calculated. The motion of the separation points on the upper and lower surfaces were tracked. The evolution and movement of the primary vortex were shown. The surface pressure distributions were also presented. All these results were compared with available experimental results.

Using the results from our calculations, a sequence of processes leading to dynamic stall were constructed.

Variations in flow characteristics due to changes in the reduced frequency were investigated. The effects of moving the axis of pitching were also presented. Finally the similarities and differences between dynamic stall due to oscillations in pitch and in heave were explored.

1.6.5 Calculation Procedure

Initially the airfoil is assumed to be at rest in a steady and uniform flow. The potential perturbations to the freestream caused by the presence of the airfoil are calulated using conformal mapping. Then the growth of the boundary layers and their separation locations are calculated by employing Stratford's [79] method. Then the separated vortex layers are convected force-free and the associated velocities are calculated according to the Biot-Savart [61] law. The wake associated velocities are included in

the next iteration while calculating the new external flow, separation points, bound circulation and additions to wakes. This procedure is repeated over several cycles of oscillations until convergence is reached (typically, six to ten oscillations). The separation points in the unsteady flow are calculated by using the extended Stratford's method developed by Gioulekas [30].

1.7 Overview of the Thesis

In chapter 1 we have presented the fundamentals of dynamic stall. We also included a literature survey with focus on dynamic stall in laminar flows. Then we have given a brief synopsis of the thesis and finally an overview.

In chapter 2 we have discussed in detail the procedure followed for calculating the external potential flow. The unsteady Bernoulli equation in an appropriate body frame of reference is derived. The conformal transformation used to map the airfoil into circle plane is also presented.

Chapter 3 gives the details of how the unsteady boundary layers are analyzed for calculating the separation points. The evolution of the separated vortex layers is also discussed here.

In chapter 4 we have validated our method by comparing our results with experiments for several test cases.

Chapter 5 presents the results for a sinusoidally pitching airfoil for several reduced frequencies. Effects of changing the axis of pitching are also presented.

In chapter 6 we have presented the results for an airfoil oscillating in heave. Effects of changing the reduced frequency are also included. We have investigated the differences and similarities between dynamic stall due to pitch and heave also.

In chapter 7 we have summarized the conclusions of our work. Some suggestions for future work are also included.

Chapter 2

Calculation of the External (Unsteady, Incompressible and Potential) Flow

2.1 Formulation of the Problem and Choice of Coordinates

When treating time-dependent motions of bodies, the selection of the coordinate systems becomes very important. It is useful to describe the unsteady motion of the

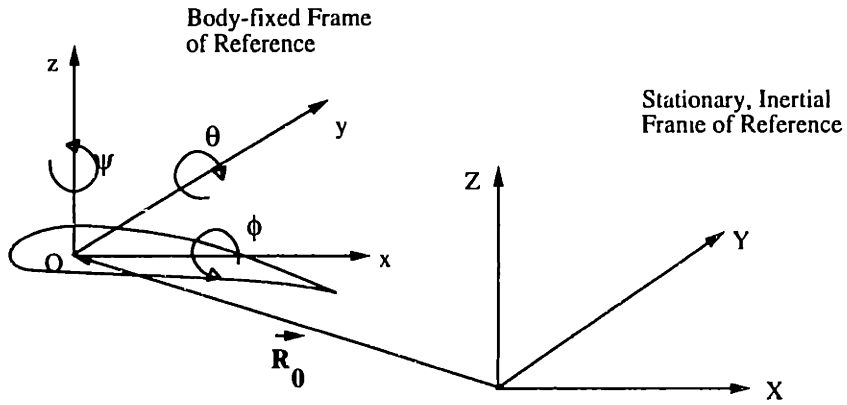

Figure 2.1: Inertial and body coordinates used to describe the motion of the body.

surface on which the "zero normal flow" boundary condition is applied in a body-fixed coordinate system (x, y, z), as shown for the example of a maneuvering airfoil in Fig. 2.1.

The motion of the origin O of this coordinate system (x, y, z) is then described in an inertial frame of reference (X, Y, Z) and is assumed to be known. For simplicity, assume without loss of generality, that at $t = 0$ the inertial frame (X, Y, Z) coincides with the frame (x, y, z). Then at $t > 0$, the relative motion of the origin (X_0, Y_0, Z_0) of the body fixed frame (x, y, z) is prescribed by its location $\vec{R}_0(t)$ and the instantaneous orientation of this frame, $\vec{\Theta}(t)$, where (ϕ, θ, ψ) are the rotation angles. Therefore

$$(X_0, Y_0, Z_0) = \vec{R}_0(t) \tag{2.1}$$

$$(\phi, \theta, \psi) = \vec{\Theta}(t) \tag{2.2}$$

The fluid surrounding the body is assumed to be inviscid, irrotational and incompressible over the entire flow field, excluding the body's solid boundaries and its wakes. Therefore, a velocity potential $\Phi(X, Y, Z, t)$ can be defined in the inertial frame and the continuity equation, in this frame of reference, becomes

$$\nabla^2\Phi(X, Y, Z, t) = 0 \tag{2.3}$$

A derivation of the above equation can be found in any basic aerodynamics book, such as [45].

Let $-\vec{v}(X, Y, Z, t)$ be the surface's velocity and $\vec{n}(X, Y, Z, t)$ the vector normal to this moving surface, as viewed from the inertial frame of reference. The boundary condition requiring zero normal velocity across the body's solid boundaries is

$$(\nabla\Phi + \vec{v}) \cdot \vec{n}|_{X,Y,Z} = 0 \tag{2.4}$$

Note that $\vec{v}$ is defined with a minus so that the surface velocity will be positive in the body's frame of reference. Since equation 2.3 does not depend directly on time, the time dependency of Φ is introduced through this boundary condition. It is interesting to point out that Φ is the total velocity potential, but as a result of its definition in a frame that is attached to the undisturbed fluid its magnitude can be, or often is small (in fact it is similar to the perturbation potential).

The second boundary condition requires that the flow disturbance, due to the body's

motion through the fluid, should approach zero far from the body:

$$\lim_{|\vec{R}-\vec{R}_0|\to\infty} \nabla\Phi = 0 \tag{2.5}$$

where $\vec{R} = (X, Y, Z)$.

Note that the two boundary conditions described above can uniquely determine an unsteady potential flow only in conjunction with the Kelvin condition [3] on circulation. In general, it states that the angular momentum in the flow be preserved. In particular, for a flow with no net torque and zero perturbations at large distances, the theorem states that for all times the circulation Γ around a fluid curve enclosing the airfoil and its wake is conserved:

$$\frac{d\Gamma}{dt} = 0 \tag{2.6}$$

The solution of this problem, which becomes time dependent because of the boundary condition (equation 2.4), is easier in the body-fixed coordinate system. Consequently, a transformation f between the coordinate systems has to be established, based on the flight path information given by equations 2.2:

$$\begin{pmatrix} x \\ y \\ z \end{pmatrix} = f(X_0, Y_0, Z_0, \phi, \theta, \psi) \begin{pmatrix} X \\ Y \\ Z \end{pmatrix}$$

Such a transform should include the translation and the rotation of the (x, y, z) system. The transform can be found in any basic rigid body dynamics book, such as

[77] and can be written out as:

$$\begin{pmatrix} x \\ y \\ z \end{pmatrix} = \begin{pmatrix} 1 & 0 & 0 \\ 0 & cos\phi(t) & -sin\phi(t) \\ 0 & sin\phi(t) & cos\phi(t) \end{pmatrix} \begin{pmatrix} cos\theta(t) & 0 & sin\theta(t) \\ 0 & 1 & 0 \\ -sin\theta(t) & 0 & cos\theta(t) \end{pmatrix} \begin{pmatrix} cos\psi(t) & -sin\psi(t) & 0 \\ sin\psi(t) & cos\psi(t) & 0 \\ 0 & 0 & 1 \end{pmatrix} \begin{pmatrix} X - X_0 \\ Y - Y_0 \\ Z - Z_0 \end{pmatrix} \tag{2.7}$$

Similarly, the kinematic velocity $\vec{v}$ of the surface due the motion of the airfoil in Fig. 2.1, as viewed in the body frame of reference, is given by

$$\vec{v} = -\left(\vec{V_0} + \vec{\Omega} \times \vec{r}\right) \tag{2.8}$$

where $\vec{V_0}$ is the velocity of the (x, y, z) system's origin, resolved into the instantaneous (x, y, z) directions

$$\vec{V_0} = (\dot{X}_0, \dot{Y}_0, \dot{Z}_0)$$

Here $\vec{r} = (x, y, z)$ is the position vector and $\vec{\Omega}$ is the rate of rotation of the body's frame of reference, as shown in Fig. 2.1,

$$\vec{\Omega} = \dot{\vec{\Theta}}(t) = (\dot{\phi}, \dot{\theta}, \dot{\psi})$$

To an observer in the (x, y, z) frame, the velocity direction is opposite to the flight

direction (as derived in the (X, Y, Z) frame) and therefore a minus appears in equation 2.8.

The proper transformation of equations 2.3-2.5 into the body's frame of reference requires the evaluation of the various derivatives in the (x, y, z) system. This can be found using the standard chain rule of differentiation and for example $\partial/\partial X$ becomes

$$\frac{\partial \Phi}{\partial X} = \frac{\partial x}{\partial X}\frac{\partial \Phi}{\partial x} + \frac{\partial y}{\partial X}\frac{\partial \Phi}{\partial y} + \frac{\partial z}{\partial X}\frac{\partial \Phi}{\partial z}$$

The time derivative in the (x, y, z) can be obtained from the chain rule also:

$$\frac{\partial \Phi}{\partial t_{inertial}} = -\left(\vec{V}_0 + \vec{\Omega} \times \vec{r}\right) \cdot \left(\frac{\partial}{\partial x}, \frac{\partial}{\partial y}, \frac{\partial}{\partial z}\right) \Phi + \frac{\partial \Phi}{\partial t_{body}} \tag{2.9}$$

But it is possible to transform equations 2.3-2.5 into the body's frame of reference without explicitly knowing equation 2.7 and still arrive at the same conclusions. For example, at any moment the continuity equation is independent of the coordinate system and the mass should be conserved. Therefore, the quantity $\nabla^2\Phi$ is independent of the instantaneous coordinate system and the continuity equation in terms of (x, y, z) remains unchanged:

$$\nabla^2\Phi(x, y, z, t) = 0 \tag{2.10}$$

Also, the two boundary conditions, equations 2.4 and 2.5, should state the same

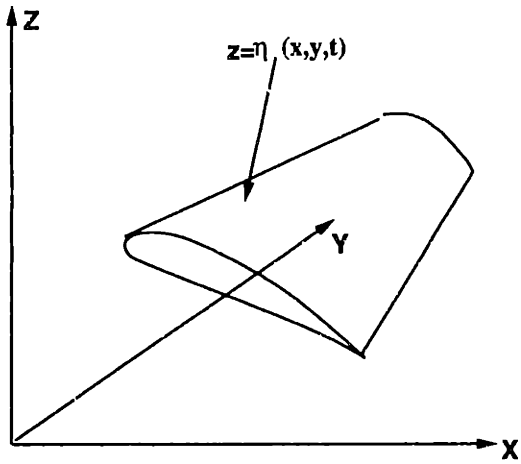

Figure 2.2: Equation for Body Surface in Body Coordinates.

physical conditions. The gradient $\nabla\Phi$ will have the same magnitude and direction and the kinematic velocity $\vec{v}$ is given by equation 2.8 and therefore the "zero-velocity normal to a solid surface" boundary condition, in the body frame becomes

$$(\nabla\Phi + \vec{v}) \cdot \vec{n}|_{x,y,z} = 0$$

Here $\vec{n}$ is in terms of the body coordinates.

By using equation 2.8, the above equation can be written as

$$(\nabla\Phi - \vec{V_0} - \vec{\Omega} \times \vec{r}) \cdot \vec{n} = 0 \tag{2.11}$$

Note that this boundary condition can be derived directly from the more common terminology [3], in which the surface is defined in the body frame of reference by a

function η as shown in the Fig. 2.2. The equation for the surface η can be written as

$$z = \eta(x, y, t)$$

Another function F, also in the body coordinates (x, y, z) can be formulated as

$$F(x, y, z, t) = z - \eta(x, y, t) = 0 \qquad \text{on the body surface.}$$

Particles on the surface move such that F remains zero. Therefore the derivative of F following the surface particles must be zero:

$$\frac{DF}{Dt_{X,Y,Z}} = \frac{\partial F}{\partial t_{X,Y,Z}} + \nabla\Phi \cdot \nabla F|_{X,Y,Z} = 0$$

Since the normal is proportional the the gradient of F

$$\vec{n} = \frac{\nabla F}{|\nabla F|}$$

Transforming the equation for $\frac{DF}{Dt_{X,Y,Z}}$ into the body coordinates (x, y, z) requires the use of equation 2.9 for the $\frac{\partial F}{\partial t_{X,Y,Z}}$ term. With the second term remaining unchanged the equation for $\frac{DF}{Dt_{X,Y,Z}}$ in the body coordinates (x, y, z) becomes

$$\frac{\partial F}{\partial t_{x,y,z}} - (\vec{V_0} + \vec{\Omega} \times \vec{r}) \cdot \nabla F\Big|_{x,y,z} + \nabla\Phi \cdot \nabla F|_{x,y,z} = 0$$

If no relative motion occurs within the body frame, as is the case in the present formulation

$$\frac{\partial F}{\partial t} = -\frac{\partial \eta}{\partial t} = 0$$

After dividing through by $|\nabla F|$, the above equation can be written in (x, y, z) as

$$(\nabla \Phi - \vec{V_0} - \vec{\Omega} \times \vec{r}) \cdot \vec{n} = 0$$

thus recovering equation 2.11.

2.2 Computation of Pressures

Solution of equation 2.10 will provide the velocity potential and the velocity components. Once the flow field is determined the resulting pressures can be computed by the Bernoulli equation, [40]. In the inertial frame of reference this equation is (in X, Y, Z coordinates):

$$\frac{p - p_\infty}{\rho} = -\frac{1}{2}|\nabla \Phi|^2 - \frac{\partial \Phi}{\partial t} \tag{2.12}$$

The magnitude of the velocity $\nabla \Phi$ is independent of the frame of reference and therefore the form of the first term on the right hand side of this equation remains unchanged. The time derivative of the velocity potential, however, is affected by the frame of reference and must be evaluated by using equation 2.9. Therefore, the

pressure $p - p_\infty$ will have the form (in x, y, z coordinates):

$$\frac{p - p_\infty}{\rho} = -\frac{1}{2}|\nabla\Phi|^2 + \left(\vec{V}_0 + \vec{\Omega} \times \vec{r}\right) \cdot \nabla\Phi - \frac{\partial\Phi}{\partial t} \tag{2.13}$$

Viewed from the origin of the body reference frame, fluid far upstream will appear to be moving towards the frame at a velocity $-\vec{V}_0$. Or viewing from the inertial frame, the origin of the body reference frame has a velocity $\vec{V}_0$. Therefore the pressure coefficient C_p can be defined as (in x, y, z coordinates):

$$C_p = \frac{p - p_\infty}{\frac{1}{2}\rho\left|\vec{V}_0\right|^2} = -\frac{|\nabla\Phi|^2}{\left|\vec{V}_0\right|^2} + \frac{2}{\left|\vec{V}_0\right|^2}\left(\vec{V}_0 + \vec{\Omega} \times \vec{r}\right) \cdot \nabla\Phi - \frac{2}{\left|\vec{V}_0\right|^2}\frac{\partial\Phi}{\partial t} \tag{2.14}$$

2.3 Conditions Far Away from the Body

Far away from the body the perturbations decay and so

$$|\nabla\Phi| \rightarrow 0$$

The term $\frac{\partial\Phi}{\partial t}$ may not necessarily approach zero as would be the case for a moving vortex. Far away from the body the gradient of the pressure can be written as

$$\nabla p \sim \nabla\left[\left(\vec{V}_0 + \vec{\Omega} \times \vec{r}\right) \cdot \nabla\Phi\right] - \frac{\partial}{\partial t}(\nabla\Phi)$$

Since $\vec{V}_0$ is not a function of space and $\nabla\Phi \rightarrow 0$, the above equation reduces to

$$\nabla p \sim \nabla\left[\left(\vec{\Omega} \times \vec{r}\right) \cdot \nabla\Phi\right]$$

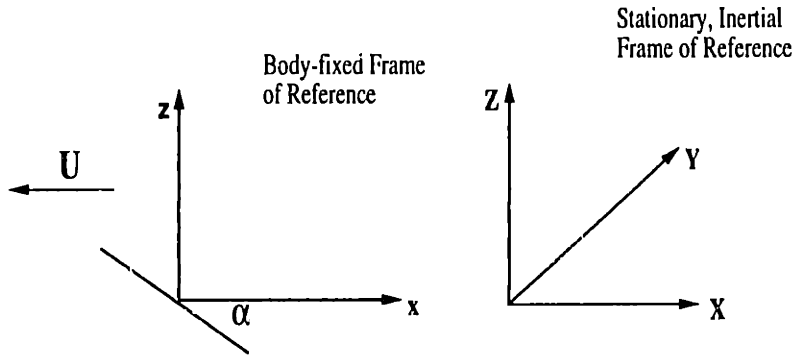

Figure 2.3: Translation of Airfoil Fixed to the (x, y, z) Frame at $-U_\infty$

The term on the right hand side of the above equation behaves, again far away from body, as

$$\nabla\left[\left(\vec{\Omega}\times\vec{r}\right)\cdot\nabla\Phi\right] \sim \frac{1}{r}\, r\, \frac{\Phi}{r} \sim \frac{\Phi}{r}$$

Therefore, $\nabla p \to 0$ as $r \to \infty$ for all kinds of perturbations. In other words pressure tends to a constant p_∞ at large distances from the body.

2.4 Examples of Unsteady Boundary Conditions

2.4.1 Flat Plate at Constant Speed

Consider a flat plate at an angle of attack α moving at a constant velocity U_∞ in the negative X direction, as shown in Fig. 2.3. The translation and rotation of the origin of the body fixed frame (x, y, z) are given by:

$$\vec{V_0} = (\dot{X}_0, \dot{Y}_0, \dot{Z}_0) = (-U_\infty, 0, 0)$$

$$\Omega = 0$$

The vector $\vec{n}$ on the flat plate and in the body frame is

$$\vec{n} = (\sin\alpha, 0, \cos\alpha)$$

Substitution of these values into equations 2.11 and 2.14 yields

$$\frac{\partial\Phi}{\partial z} = -(U_\infty + \frac{\partial\Phi}{\partial x})\tan\alpha$$

$$C_p = 1 - \frac{(U_\infty + \Phi_x)^2 + {\Phi_z}^2}{{U_\infty}^2} - \frac{2}{{U_\infty}^2}\frac{\partial\Phi}{\partial t}$$

which are the well known classical results [45].

2.4.2 Flat Plate Accelerating at a Constant Rate

Consider now the case where the plate accelerates at a uniform rate a in the negative X direction. In this case, at a time t after the airfoil started its motion:

$$\vec{V_0} = (-at, 0, 0)$$

$$\vec{\Omega} = (0, 0, 0)$$

$$\vec{n} = (\sin\alpha, 0, \cos\alpha)$$

$$\frac{\partial\Phi}{\partial z} = -(at + \frac{\partial\Phi}{\partial x})\tan\alpha$$

$$C_p = 1 - \frac{(at + \Phi_x)^2 + {\Phi_z}^2}{(at_0)^2} - \frac{2}{(at_0)^2}\frac{\partial\Phi}{\partial t}$$

where the speed at a reference time t_0 is used to nondimensionalize the pressure.

2.4.3 Flat Plate in Sinusoidal Heave and Uniform Forward Flight

Consider an airfoil moving with a constant speed U_∞, at an angle of attack α in the negative X direction and undergoing sinusoidal heaving displacement in the Z direction given by:

$$h = h_0 \sin\omega t$$

$$\dot{h} = h_0\omega\cos\omega t$$

Therefore

$$\vec{V_0} = (-U_\infty, 0, -h_0\omega\cos\omega t)$$

$$\vec{\Omega} = (0, 0, 0)$$

Then the zero normal flow boundary condition becomes

$$\vec{n} = (\sin\alpha, 0, \cos\alpha)$$

$$\frac{\partial\Phi}{\partial z} = -(U_\infty + \frac{\partial\Phi}{\partial x})\tan\alpha + h_0\omega\cos\omega t$$

The the C_p is calculated to be:

$$C_p = 1 - \frac{(U_\infty + \Phi_x)^2 + {\Phi_z}^2}{{U_\infty}^2} + \frac{2}{{U_\infty}^2}h_0\omega\cos\omega t\frac{\partial\Phi}{\partial z} - \frac{2}{{U_\infty}^2}\frac{\partial\Phi}{\partial t}$$

2.4.4 Flat Plate in Sinusoidal Pitch and Uniform Forward Flight

The pitching motion of the airfoil is described by:

$$\alpha(t) = \bar{\alpha} + \tilde{\alpha}\sin\omega t$$

Therefore

$$\vec{V_0} = (-U_\infty, 0, 0)$$

$$\dot{\alpha} = \tilde{\alpha}\omega\cos\omega t$$

$$\vec{\Omega} = (0, \dot{\alpha}, 0)$$

$$\vec{n} = (\sin\alpha, 0, \cos\alpha)$$

$$\vec{r} = (x, y, z)$$

The zero normal flow condition yields

$$\frac{\partial \Phi}{\partial z} = -(U_\infty + \frac{\partial \Phi}{\partial x}) \tan \alpha + \dot{\alpha}(z \tan \alpha - x)$$

We can see that if the airfoil is pitching about its midchord and the chord is $2b$, then for $\alpha(t) = 0$, the upwash at the leading edge is

$$\left.\frac{\partial \Phi}{\partial z}\right|_{at\ leading\ edge} = \dot{\alpha} b$$

which is the correct result. The C_p is calculated to be

$$C_p = 1 - \frac{(U_\infty + \Phi_x)^2 + {\Phi_z}^2}{{U_\infty}^2} + \frac{2}{{U_\infty}^2}\dot{\alpha}(z\frac{\partial \Phi}{\partial x} - x\frac{\partial \Phi}{\partial z}) - \frac{2}{{U_\infty}^2}\frac{\partial \Phi}{\partial t}$$

2.5 An Alternate Frame of Reference

Consider now a different flow in which the flat plate is at rest in a spatially uniform unsteady flow given by

$$\vec{q}_\infty = (U_\infty, V_\infty, W_\infty)$$

If $(\acute{x}, \acute{y}, \acute{z})$ is a coordinate system fixed in the stationary (inertial) body, then the free stream potential ϕ for this flow is

$$\phi = (\acute{x}, \acute{y}, \acute{z}) \cdot \vec{q}_\infty = \acute{x} U_\infty(t) + \acute{z} W_\infty(t)$$

where two dimensional flow in $\acute{x} - \acute{z}$ space was assumed for simplicity. The unsteady Bernoulli equation relates the pressures and velocities at two different points $(\acute{x}_1, \acute{z}_1)$

and $(\acute{x}_2, \acute{z}_2)$ according to the following equation:

$$\frac{p_1}{\rho} + \frac{1}{2}|\nabla\phi|_1^2 + \frac{\partial\phi_1}{\partial t} = \frac{p_2}{\rho} + \frac{1}{2}|\nabla\phi|_2^2 + \frac{\partial\phi_2}{\partial t}$$

Observing that

$$|\nabla\phi|_1 = |\nabla\phi|_2 = |\vec{q}_\infty|$$

the above Bernoulli can be rewritten as

$$\begin{aligned} p_2 - p_1 &= -\rho\frac{\partial}{\partial t}(\phi_2 - \phi_1) \\ \Longrightarrow \quad \nabla p &= -\rho\frac{\partial}{\partial t}(\nabla\phi) \\ \Longrightarrow \quad \nabla p &= -\rho\frac{d\vec{q}_\infty}{dt} \end{aligned}$$

It can be seen from the above equation that this pressure gradient provides the force which accelerates the fluid. The pressure gradient resembles a buoyancy force and acts on the center of geometry of the airfoil in the direction of the freestream.

Therefore, an airfoil undergoing an arbitrary motion relative to an otherwise still fluid can be replaced, *for the purpose of potential calculations*, by a stationary airfoil placed in a fluid undergoing exactly the same motion but of opposite sign far away from the body *if* the aforementioned "buoyancy forces" are accounted for.

Thus the airfoil (discussed in the previous section) moving in the negative X direction with an acceleration a into an otherwise still fluid can be replaced, for the purposes of potential flow calculations, by a stationary airfoil in a spatially uniform unsteady

flow $\vec{q}_\infty = (at, 0, 0)$, if the forces arising due to the pressure gradient

$$\frac{\partial p}{\partial x} = -\rho \frac{d}{dt}(at) = -\rho a$$

are accounted for.

Similarly the airfoil executing sinusoidal heave $h(t)$ in the Z direction and a uniform flight at speed U_∞ in the negative X direction can be replaced, for the purpose of potential flow calculations, by a stationary airfoil in a spatially uniform unsteady flow $\vec{q}_\infty = (U_\infty, 0, -\dot{h})$ by accounting for the buoyancy forces arising from the pressure gradient as discussed above. The pressure gradient for this case is

$$\frac{\partial p}{\partial \acute{z}} = \rho \frac{d\dot{h}}{dt} = \rho \ddot{h}$$

For the case of a pitching airfoil in uniform flight, (also discussed in the previous section) such a construction would be unphysical as it makes pressure a multivalued function except when the rate of pitch is a constant.

2.6 Theodorsen's Transformation

2.6.1 General Mapping Function

Any arbitrarily shaped simply connected body can be mapped into a unit circle by using a suitable conformal transformation [38]. This procedure is well developed and

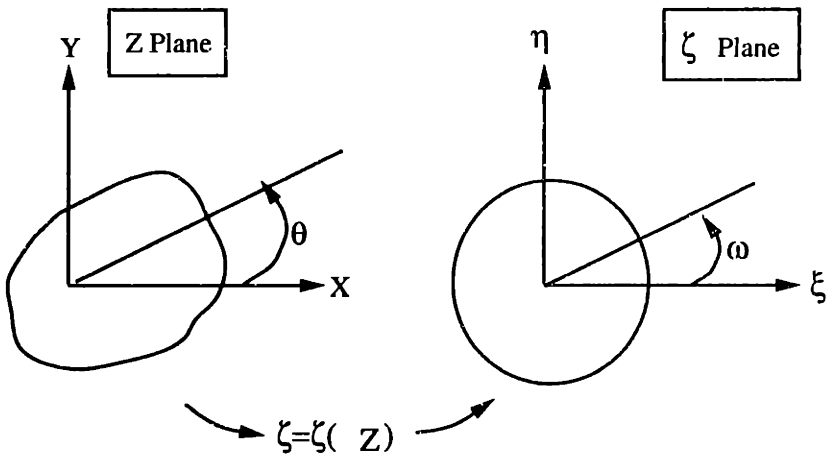

Figure 2.4: Conformal Mapping of an Arbitrarily Shaped Simply Connected Body into a Unit Circle.

documented [84, 1, 20, 38]. The particular method used here closely follows [20]. An illustration of the procedure is presented in Fig. 2.4.

Let ζ be the complex variable in the circle plane and z in the physical (airfoil) plane. So $z(\zeta)$ becomes the analytic function that relates the circle plane to the physical one. Let the complex potential of the flow in the circle plane be denoted by $F(\zeta, t) = \phi + i\psi$, where ϕ and ψ are the flow potential and the stream function, respectively. Then the complex velocity $w(\zeta, t)$ in the circle plane is given by

$$w(\zeta, t) = u - iv = \frac{\partial F}{\partial \zeta} \tag{2.15}$$

where u and v are the speeds along the real and imaginary axes, respectively.

Then the velocity in the physical plane is calculated from

$$W(z, t) = w(\zeta, t)\frac{1}{dz/d\zeta} \tag{2.16}$$

Since the perturbations should vanish far away from the body, we require of the transformation that the velocities in the two planes be equal at infinity. *i.e.*,

$$\frac{dz}{d\zeta} \to 1 \quad : \quad \zeta \to \infty$$

Then the transformation may be expressed as

$$z = \zeta + \frac{C_1}{\zeta} + \frac{C_2}{\zeta^2} + \frac{C_3}{\zeta^3} + \cdots \tag{2.17}$$

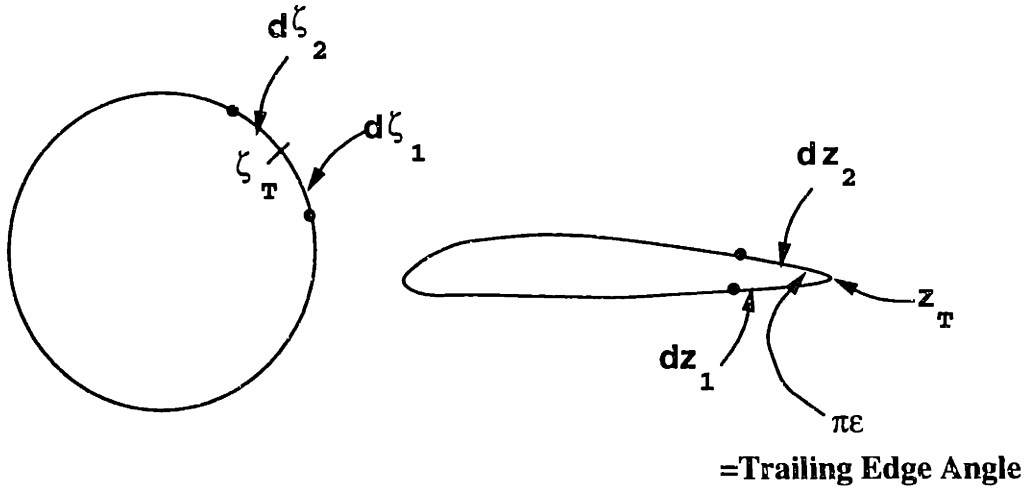

Figure 2.5: Mapping of the Trailing Edge.

Thus the problem of mapping the flow past an arbitrarily shaped object is reduced to finding the constants in the above series which can be recognized as the Laurent expanson of $z(\zeta)$ about the point at infinity in the ζ plane.

2.6.2 Mapping of the Trailing Edge

Though the above mentioned series, in theory, is adequate to find the transformation, accurate numerical implementation will be difficult if the trailing edge is sharp.

Let $z = z_T$ denote the trailing edge and let the point on the circle corresponding to z_T be denoted by ζ_T. Consider the elements dz_1 and dz_2 of the airfoil curve passing

through the point z_T, as shown in Fig. 2.5. Let $d\zeta_1$ and Let $d\zeta_2$ be the corresponding image elements at the image point ζ_T. The angle between dz_1 and dz_2, *i.e.*, the trailing edge angle, is required to be different from π if the airfoil has a sharp (or a cusped) trailing edge, as is usually the case. The angle between the image elements $d\zeta_1$ and $d\zeta_2$ is, however, equal to π. This means that the mapping should not preserve the angles at the trailing edge, that is, must be singular. This, in turn, means that the point $\zeta = \zeta_T$ should be a singular point of the transformation $z = z(\zeta)$.

All the singular points of the transformation are given by the equation $\frac{dz}{d\zeta} = 0$. Thus the mapping should be such that one of its singular points should lie on the circle while all the rest of them are included in the interior of the circle so as to leave the regions exterior to the circle and the airfoil conformal to each other. The singular point on the circle goes into the sharp trailing edge of the airfoil.

From the theorem of residues of complex functions [44] it can be shown that if the first n derivatives of the transformation function $z(\zeta)$ are zero at the point ζ_T, then the trailing edge angle $\pi\epsilon$ is given by

$$\pi\epsilon = \pi(1 - n) \tag{2.18}$$

Using this knowledge, the Laurent series in equation 2.17 can be written as

$$\frac{dz}{d\zeta} = \left(1 - \frac{1}{\zeta}\right)^{1-\epsilon} exp\left(\sum_{n=0}^{\infty} C_n \zeta^{-n}\right) \tag{2.19}$$

where C_n are the mapping coefficients determined by the shape of the airfoil being

transformed. This choice of the mapping function ensures that the trailing edge angle is accurately mapped and does not cause any loss of generality [20]. The constant of integration that results when the above equation is integrated was chosen so that $z = 0$ transforms into $\zeta = 0$.

2.6.3 Mapping Coefficient Calculation

The constant e^{C_0} in the above equation 2.19 multiplys the entire righthand side. $\Im C_0$ affects only the orientation of the airfoil and is set so that the airfoil chord lies on the x-axis. $\Re C_0$ affects only the size of the airfoil and is chosen so that the airfoil chord is of unit length.

An efficient and accurate method for determining the mapping coefficients is detailed in [20] and is not reproduced here. Calculation of only 18 coefficients (including c_{18}) was sufficient for transforming NACA 0012.

2.6.4 Velocity Field Representation

Though at the first time step there are no wake vortices in the flow field, at subsequent times the wakes drifting freely with the local velocity are represented by discrete vortices. Consider now the flow field at a time t when there are a total of N free

(wake related) vortices in the flow field. Let z_j be the location of the j-th vortex in the airfoil plane and ζ_j be the corresponding location of the j-th vortex in the circle plane. Using the knowledge of conjugate functions and images [61], we can write the complex potential for the instantaneous velocity field in the circle plane as:

$$F(\zeta,t) = w_\infty(t)(\zeta + \frac{1}{\zeta}) + \frac{i}{2\pi}\Gamma_0 \ln\zeta + \frac{i}{2\pi}\sum_{j=1}^{N}\Gamma_j\left\{\ln(\zeta-\zeta_j) - \ln(\zeta - \frac{1}{\zeta_j^\star})\right\} \quad (2.20)$$

where $w_\infty(t)$ is the instantaneous freestream complex velocity in the circle plane, *i.e.*,

$$w_\infty(t) = u_\infty - iv_\infty = \lim_{\zeta\to\infty} w(\zeta,t),$$

Γ_0 is the initial bound circulation, Γ_j is the circulation of the j-th wake element and $\zeta^\star$ is the complex conjugate of ζ. Thus $1/\zeta_j^\star$ is the location of the image vortex corresponding to a vortex at ζ_j. The positioning of the j-th vortex and its image in the circle plane is shown in Fig. 2.6.

The complex potential in the physical plane is given by $F(z(\zeta),t)$. The complex velocity in the physical plane is given, as before, by equation 2.16.

The term $\frac{\partial F}{\partial \zeta}$ in equation 2.16 is calculated as:

$$w(\zeta,t) = \frac{\partial F}{\partial \zeta} = w_\infty(1 - \frac{1}{\zeta^2}) + \frac{i\Gamma_0}{2\pi\zeta} + \frac{1}{2\pi}\sum_{j=1}^{N}\Gamma_j\left\{\frac{1}{\zeta-\zeta_j} - \frac{1}{\zeta - \frac{1}{\zeta_j^\star}}\right\}$$

The time derivative of the complex potential is:

$$\frac{\partial F}{\partial t} = \frac{dw_\infty}{dt}(\zeta + \frac{1}{\zeta}) + \frac{i}{2\pi}\sum_{j=1}^{N}\Gamma_j\left\{-\frac{\dot\zeta_j}{\zeta-\zeta_j} - \frac{1}{\zeta - \frac{1}{\zeta_j^\star}}(\frac{\dot\zeta_j^\star}{\zeta_j^{\star 2}})\right\}$$

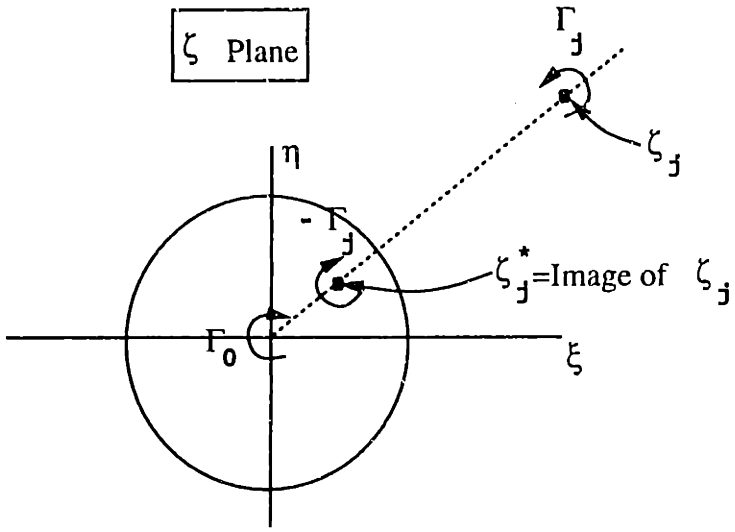

Figure 2.6: Positioning of Wake Vortices and images in the Circle Plane.

Once the velocities on the airfoil are calculated as shown above, the pressures in the inertial frame are derived by employing equation 2.14 from which forces and moments are calculated by simple integration.

Chapter 3

Calculation of the Separated Flow Field

3.1 Unsteady Boundary Layers

Once the external potential flow (with no separation assumed) is calculated as explained above, the conditions at the outer edge of the unseparated boundary layers on the body are known. The unsteady boundary layer equations applicable for this problem are [67]:

$$\frac{\partial u}{\partial t} + u\frac{\partial u}{\partial x} + v\frac{\partial u}{\partial y} - \nu\frac{\partial^2 u}{\partial y^2} = \frac{\partial U}{\partial t} + U\frac{\partial U}{\partial x}$$

$$\frac{\partial u}{\partial x} + \frac{\partial v}{\partial y} = 0$$

$$u = U(x,t) \; : \; y \; \rightarrow \; \infty; \;\; u = v = 0 \; : \; y = 0 \tag{3.1}$$

where u and v represent the velocities in the boundary layer along the body surface and perpendicular to it and U is the velocity external to the boundary layer.

These equations are derived from the Navier-Stokes equations [90] by neglecting the curvature of the airfoil, the variation of pressure across the boundary layer and the streamwise diffusion.

The inertia terms in the general equation of motion make an analysis extremely hard, because they give rise to periodic variations at higher harmonics of the frequency of the fluctuating external stream. But when the reduced frequency of the external oscillation is high enough, the local acceleration is much larger than the unsteady part of the convection of momentum. Then to a first approximation the fluctuation part of the motion can be treated as in Stokes second problem, [72]. Based on this idea C. C. Lin [50] developed an asymptotic method for analyzing the boundary layer which was later used by Gioulekas [30] to calculate the separation point of the boundary layer in an unsteady external flow.

Let the free stream velocity $U(x,t)$ have a mean component $\bar{U}(x)$ and an oscillating component $\tilde{U}(x,t)$.

Because of the no-slip condition at its surface, the airfoil resists the outer fluid motion at an average speed $\bar{U}$. Vorticity is thus generated at the body surface and forms a vortical layer that expands into the outer flow as the vorticity simultaneously diffuses away from the wall and is carried downstream by the external flow. The time required for vorticity to diffuse through a distance δ_p is of the order of δ_p^2/ν, the diffusion time. The time required for the vorticity to be convected through a distance c in the streamwise direction is $c/\bar{U}$, the convection time. In the thin boundary layer approximation these two time scales are of the same order. So we can write the boundary layer thickness associated with the mean flow, "Prandtl thickness", as

$$\delta_p \;=\; \delta_{B.L.} \sim \sqrt{\frac{\nu c}{\bar{U}}} = \frac{c}{\sqrt{Re_c}} \tag{3.2}$$

where Re_c is the Reynolds number based on chord c and the mean external velocity $\bar{U}$. In the unsteady part of the flow, the velocity changes from $-\tilde{U}$ to $\tilde{U}$ in time π/ω, where ω is angular rate of oscillation of the external flow. If δ_s is the diffusion length scale for this time, then we have, by equating the unsteady time scale to the diffusion time scale:

$$\delta_s \sim \sqrt{\frac{\nu}{\omega}} \tag{3.3}$$

where the factor π was ignored. The Prandtl and Stokes velocities are shown conceptually in Fig. 3.1.

The ratio of the "Prandtl thickness" δ_p and the "Stokes thickness" δ_s is thus propor-

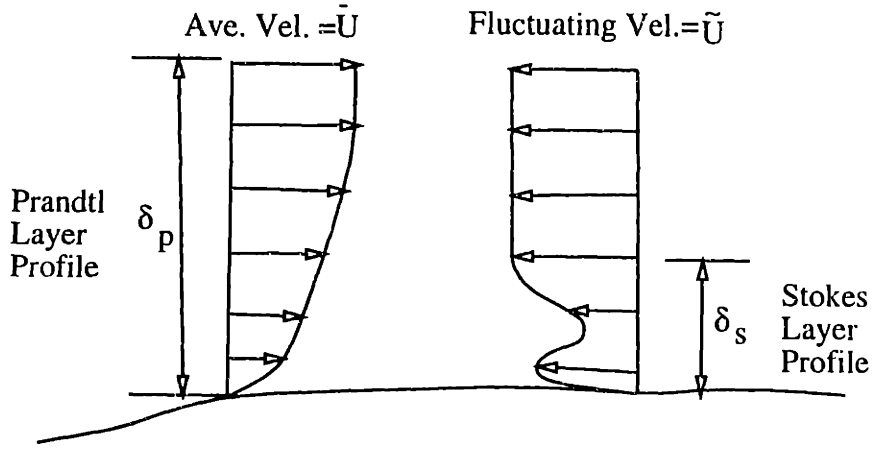

Figure 3.1: Velocity Profiles in Prandtl and Stokes Layers.

tional to the square root of the reduced frequency k

$$\frac{\delta_p}{\delta_s} \sim \sqrt{\frac{c\omega}{\bar{U}}} \propto \sqrt{k} \tag{3.4}$$

When the reduced frequency is high ($\frac{\delta_p}{\delta_s} > 1$), the outer part of the boundary layer reacts to the external oscillation in an inviscid fashion, because viscosity has insufficient time to counter the temporal changes in the freestream velocity.

When the reduced frequency is low ($\frac{\delta_p}{\delta_s} < 1$), the vorticity which is generated as the wall resists the imposed unsteadiness is convected away and does not accumulate to form a secondary layer of vorticity. In this case, the "Stokes layer" does not exist and the present method will not be applicable.

Turning back to the case where $\frac{\delta_p}{\delta_s} > 1$, we note that for much of its thickness above the "Stokes layer", the boundary layer responds to the external oscillations in an inviscid fashion. The presence of the solid boundary changes the unsteady component of the velocity from its potential value only within the secondary layer of vorticity. Thus the situation is similar to the one present in Stokes' second problem. If this velocity field is subtracted from the boundary layer velocity, what remains is a velocity field of predominantly steady character, which at large distances from the body surface tends to the mean value of the freestream velocity.

A similar analysis lead [50] to divide the boundary layer velocity (u, v) into the "Stokes velocity" (u_s, v_s) corresponding to the fluctuating component $\tilde{U}(x,t)$ and the "Prandtl velocity" (u_p, v_p) corresponding to the mean component $\bar{U}(x)$. Thus;

$$y \to \infty \ : \ u_p = \bar{U}(x), \ u_s = \tilde{U}(x,t)$$

At the wall, the two components together satisfy the no-slip condition:

$$y = 0 \ : \ u_p + u_s = 0, \ v_p = v_s = 0$$

In the region that lies between the edges of the two layers, the "Stokes flow" has attained its freestream value. Therefore for

$$y > \delta_s \ : \ u = u_p + \tilde{U}, \ v = v_p + V_s$$

where V_s is the value of the normal velocity corresponding to $\tilde{U}$, consistent with the equation of continuity for the "Stokes component" (u_s, v_s). For the flow within the

"Stokes layer" we have, as mentioned before,

$$y < \delta_s \; : \; u = u_p + u_s, \; v = v_p + v_s$$

Thus the equations 3.1 for boundary layer flow can be divided into those for "Prandtl flow", given by:

$$\frac{\partial u_p}{\partial t} + u_p\frac{\partial u_p}{\partial x} + v_p\frac{\partial u_p}{\partial y} + u_p\frac{\partial \tilde{U}}{\partial x} + v_p\frac{\partial \tilde{U}}{\partial y} + \tilde{U}\frac{\partial u_p}{\partial x} + V_s\frac{\partial u_p}{\partial y}$$
$$-\nu\frac{\partial^2 u_p}{\partial y^2} = \bar{U}\frac{\partial \bar{U}}{\partial x} + \frac{\partial}{\partial x}(\bar{U}\bar{U})$$
$$\frac{\partial u_p}{\partial x} + \frac{\partial v_p}{\partial y} = 0$$

$$u_p = \bar{U}(x) \; : \; y \rightarrow \infty; \;\; u_p + u_s = 0, \; v_p = 0 \; : y = 0 \tag{3.5}$$

The corresponding equations for "Stokes flow" are:

$$\frac{\partial u_s}{\partial t} + u_s\frac{\partial u_s}{\partial x} + v_s\frac{\partial u_s}{\partial y} + \left[(u_s - \bar{U})\frac{\partial}{\partial x} + (v_s - V_s)\frac{\partial}{\partial y}\right]u_p$$
$$+(u_p\frac{\partial}{\partial x} + v_p\frac{\partial}{\partial y})(u_s - \tilde{U}) - \nu\frac{\partial^2 u_s}{\partial y^2} = \frac{\partial \tilde{U}}{\partial t} + \tilde{U}\frac{\partial \tilde{U}}{\partial x}$$
$$\frac{\partial u_s}{\partial x} + \frac{\partial v_s}{\partial y} = 0$$

$$u_s = \tilde{U}(x,t) \; : \; y \rightarrow \infty; \;\; u_p + u_s = 0, \; v_s = 0 \; : y = 0 \tag{3.6}$$

Since we are looking to solve the above sets of equations for high reduced frequency cases *i.e.*, for ($\frac{\delta_p}{\delta_s} > 1$), the "Prandtl velocities" within the "Stokes layer" can be

replaced by their Taylor expansions about the point $(x, y_p = 0)$:

$$u_p = \sum_{n=0}^{\infty} \frac{y_p^n}{n!} \frac{\partial^n u_p}{\partial y_p^n}(x, 0)$$
$$v_p = \sum_{n=0}^{\infty} \frac{y_p^n}{n!} \frac{\partial^n v_p}{\partial y_p^n}(x, 0)$$

Then the velocities (u_p, v_p) and (u_s, v_s) are expanded in inverse powers of the reduced frequency k:

$$u_p = \sum_{n=0}^{\infty} \frac{1}{k^n} u_{p,n}$$
$$u_s = \sum_{n=0}^{\infty} \frac{1}{k^n} u_{s,n}$$
$$v_p = \sum_{n=0}^{\infty} \frac{1}{k^n} v_{p,n}$$
$$v_s = \sum_{n=0}^{\infty} \frac{1}{k^n} v_{s,n}$$

At each level of approximation, the velocity distributions are expressed in terms of their mean and fluctuating parts, for example

$$u_{p,n} = \bar{u}_{p,n} + \tilde{u}_{p,n}$$

The equations for the mean flow are found by taking the time average of the equation systems 3.5, 3.6. Then, the equations for the mean parts are subtracted from the original equations to get the equations for the fluctuating parts of the flow. The equations for the oscillating part had to be solved before the equations for the mean parts of the flow.

A complete description of the mathematical details of the solution procedure is supplied by Gioulekas [30] and is not reproduced here. The systems of equations 3.5, 3.6 are solved up to and including the third approximation (terms corresponding to k^{-2}).

The zeroth order "Prandtl components" and the "Stokes components" and their respective boundary conditions are completely decoupled.

The unsteady part of the zeroth order "Prandtl velocity" $\tilde{u}_{p,0}$ comes out be identically zero. The steady part of the zeroth order "Prandtl velocity" $\bar{u}_{p,0}$ becomes equal to the steady profile corresponding to the mean component of the external velocity $\bar{U}$ and the associated pressure gradient.

Similarly, the steady part of the zeroth order "Stokes velocity" $\bar{u}_{s,0}$ is identically zero and the unsteady zeroth order "Stokes velocity" is the solution to Stokes second problem when the external oscillating flow is of the magnitude $\tilde{U}$. This was derived also by Lighthill [48].

The higher order solutions are not so readily distinguishable and are coupled through boundary conditions at the wall.

3.2 Boundary Layer Separation

3.2.1 Conditions at Unsteady Separation

Flow separation is generally understood [47, 5, 72, 82] as a sharp increase in the normal component of the velocity in the boundary layer or as a sharp increase in the displacement thickness δ^*. It is easy to verify, from the basic definition of δ^*, that the two definitions are equivalent to each other.

In steady flows, flow separation is always associated with reversal of the flow direction immediately downstream of the separation point, as explained in [67]. On the other hand, in the Stokes second problem the flow direction oscillates in time continuously. But there is no sign of flow separation in a purely oscillatory flow, like the Stokes second problem. The implication is that while flow reversal in a steady boundary layer necessarily indicates separation, instantaneous flow reversal in an unsteady boundary layer does not indicate separation.

It is also known [31, 9, 19] that the boundary layer equations exhibit a singular behavior as the separation point $x = x_s$ is approached. Within the thin boundary layer approximation, the scaled skin friction, *i.e.*,

$$\lim_{Re\to\infty}(Re^{1/2}\tau)$$

is generally bounded upstream of the separation point, but becomes nonanalytic as the separation point is approached, *i.e.*

$$Re^{1/2} \left.\frac{\partial u}{\partial y}\right|_{y=0} \propto (x_s - x)^{1/2}$$

where Re is the Reynolds number and τ is the skin friction. The skin friction in the Stokes second problem does not exhibit any such singular behavior.

Experiments conducted by [43, 60, 53] extend support to the argument that temporal flow direction reversals present in unsteady boundary layers do not indicate and are not associated with separation.

The behavior of the "Stokes velocities" and the associated skin friction are similar to that of the corresponding flow variables in the Stokes second problem. All the "Stokes velocities" in the asymptotic expansion of the boundary layer velocities of the previous section are governed by diffusion-like equations and are thus nonsingular. The associated displacement thickness is bounded and remains analytic throughout the flow field.

Led by an analysis similar to the one presented here, Gioulekas [30] concluded that attention should be focused on "Prandtl flow" to determine the location of the separation point.

With reference to the "Prandtl flow" (equations 3.5) and the analysis presented by

Goldstein [31], far upstream of the point of separation

$$\frac{v_p}{u_p} \sim O(\frac{1}{\sqrt{Re}}); \quad \frac{\partial}{\partial x^*} \sim O(1) \tag{3.7}$$

As the separation point $x = x_s$ is approached

$$\frac{v_p}{u_p} \sim O(1); \quad \frac{\partial}{\partial x^*} \sim O(\sqrt{Re}) \tag{3.8}$$

where $x^* = x/c$ is the nondimensionalized streamwise coordinate.

Therefore, changes in the x-direction become pronounced near separation, as shown by [31]. This means that the boundary layer approximation fails, streamwise diffusion becomes important and the governing momentum equation becomes elliptic (in $x - y$ space, though it remains parabolic in the $t - x/y$ space). Then there is upstream influence and in order to continue the solution beyond the separation point, the influence of the ejected boundary layer flow on the imposed pressure gradient has to be accounted for.

For steady flows the triple deck theory developed by Sychev [81] and subsequently advanced by Stewertson [9] explains this local interaction. No such comprehensive theory exists for unsteady separation.

Analogous to steady separation, Gioulekas [30] defined the separation point in unsteady flow as the point where the boundary layer equations become singular. This singularity, as explained above, appears in the "Prandtl component" of the boundary

layer flow. As proved by [30, 82] this singularity appears at a point (x_s, y_s) in the flow at which the following conditions are satisfied:

$$\frac{\partial u_p}{\partial y} = 0$$
$$u_p + \tilde{U} - \frac{dx_s}{dt} = 0 \tag{3.9}$$

where u_p stands, as before, for the "Prandtl component" of the streamwise velocity.

According to these conditions an observer moving with a speed equal to the difference between the speed of the separation point and the oscillating part of the freestream velocity, sees a stagnation point within the "Prandtl component" of the velocity field. Such an observer sees the fluid particles being decelerated as they approach the separation point. In order to satisfy continuity, they exchange the streamwise velocity for normal velocity and this causes the dramatic increase in the transverse velocity component at separation.

Moore, Rott and Sears [74] proposed as conditions for unsteady separation the simultaneous vanishing of the shear and the velocity at a point within the boundary layer and in a frame of reference moving with separation. The conditions, to be satisfied at the separation point are:

$$\frac{\partial u}{\partial y} = 0$$
$$u = \frac{dx_s}{dt}$$

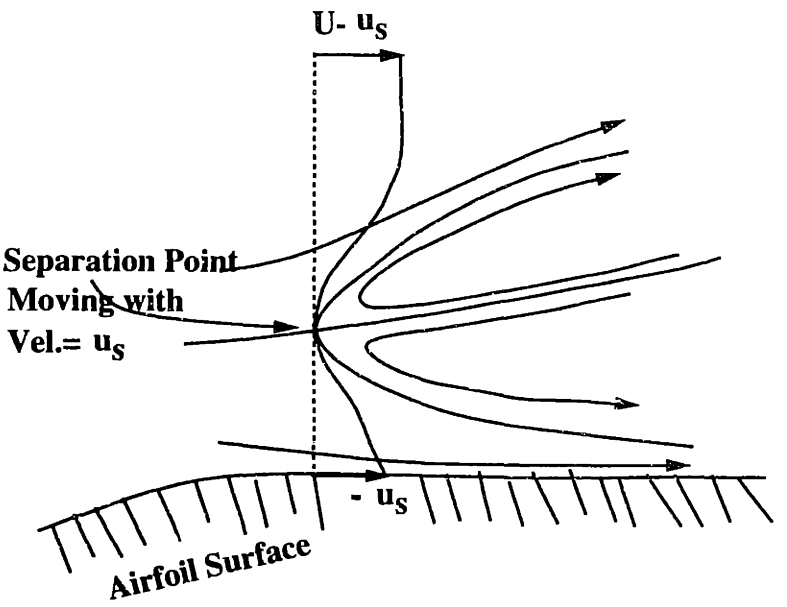

Figure 3.2: The Prandtl Velocity Field at Separation, Viewed by an Observer Moving with the Separation Point.

It is easy to verify that the two conditions are consistent with each other and for "large" reduced frequency, they are in fact identical. The streamlines at an unsteady separation point are shown in Fig. 3.2.

If we replace the boundary layer velocity $u = u_p + u_s$ in the MRS conditions with $u = u_p + \tilde{U}$, we can in fact see the equivalency between the two conditions. The above replacement is possible, because, as explained in the previous section, for high

reduced frequency k

$$\frac{\delta_s}{\delta_p} \ll 1$$

which means that for most of the "Prandtl layer", $u_s \simeq \tilde{U}$. This approximation becomes more and more accurate as k increases.

3.2.2 Criterion for Predicting Separation

For steady flows there are a variety [17] of well established approximate conditions for predicting the separation point. Of particular interest to us is the method put forward by Stratford [79].

It is based on a division of the boundary layer into two parts, one towards the outer edge of the layer and the other adjacent to the wall. In the outer part of the boundary layer the loss of total head due to viscosity is small and and is assumed to be independent of the pressure gradient. Then the total head loss along any particular streamline can be approximated by the total head loss along a corresponding streamline in a Blasius flow at the same external speed. Since the loss of total head can be calculated for a Balsius profile, the above approximation determines the shape of the outer profile.

In the inner part of the boundary layer the convection terms are small and can

be neglected in the momentum balance. The inner profile is approximated by a polynomial of third order in the normal coordinate. Then the two velocity profiles are patched together so that the velocity and its first and second derivatives are continuous at a point automatically determined by the conditions imposed. This model yields, for the pressure coefficient c_p

$$c_p \left(x \frac{dc_p}{dx} \right)^2 = 0.0104(1 - \frac{\tau_w}{\tau_b})^2(1 + 2\frac{\tau_w}{\tau_b}) \tag{3.10}$$

where, τ_w is the wall shear at x and τ_b is the shear in Blasius flow at the corresponding point. At separation $x = x_s$, $\tau_w = 0$, therefore

$$c_p \left(x_s \frac{dc_p}{dx}|_{x=x_s} \right)^2 = 0.0104 \tag{3.11}$$

Stratford's original proposal for the number on the right hand side was 0.0108, but it was noted in [17] that 0.0104 resulted in more accurate predictions for a wider variety of flows. The method is designed for flows in which the pressure remains constant from the leading edge for some distance, after which the pressure rises steeply. The presence of a favorable pressure gradient from the stagnation point to the suction peak is taken into account by using the "equivalent constant pressure region" concept explained in [67]. The method is applicable if the pressure coefficient at the separation

point $C_{p,s} < 1/8$ and becomes increasingly accurate as the adverse pressure gradient increases or equivalently, $C_{p,s}$ decreases.

Gioulekas [30] derived a condition for flow separation in unsteady boundary layers. This method depends on the ideas used in the Stratford's method for modeling the variation of the "Prandtl component" of the streamwise velocity along the airfoil contour.

We have shown above that the occurence of unsteady separation can be identified by focusing attention on the behavior of the "Prandtl" part of the flow. It was shown by Gioulekas [30] that the basic or the zeroeth order "Prandtl" component and the unsteady part of the external flow alone are sufficient to construct the "Prandtl" velocity distribution along the blade surface. Therefore, if variation along the blade surface of the basic velocity is known, then we will be able to construct the whole "Prandtl Velocity" using the former as the building block and the separation point can then be located by solving the conditions given in equations 3.9. In order to find how the mean "Prandtl" velocity changes with streamwise location under the influence of the adverse pressure gradient, a variation of Stratford's [79] ideas were used to derive a relation which describes how the wall stress τ_w changes with x. The wall stress determines the basic velocity profile $u_b(x,y)$ uniquely. Then, as mentioned above, $u_b(x,y)$ is used, in conjunction with parameters of the external flow, to construct the whole "Prandtl" flow and then the latter is used in the separation conditions 3.9 to

calculate unsteady separation point.

In the unsteady case, by modeling the development of the mean "Prandtl" velocity as outlined aboe, an equation is obtained, which in functional nondimensional form can be written out as:

$$F(x, \frac{\tau_w}{\tau_b}, c_p, \frac{dc_p}{dx}, \frac{\overline{\tilde{U}\tilde{U}'}}{k}) = 0 \tag{3.12}$$

where, the velocities aıe nondimensionalized by the velocity at the suction peak and $c_p = 1 - (\tilde{U})^2$. The above equation describes essentially how the wall shear τ_w, which uniquely determines the basic and thus the "Prandtl" velocities, varies with the streamwise location x.

The instantaneous location of separation is found by combining this algebraic equation with the separation conditions, 3.9.

3.3 Evolution of the Free Vortex Layers and Interaction with the Airfoil

In the immediate neighborhood of the separation point, the shear layer "lifts off" or moves away from the wall. The shear layer leaves the surface of the airfoil tangentially, as pointed out by Batchelor [4]. After leaving the surface the vortex layer

gets convected into the external flow in a force free manner, *i.e.*, such that there is no pressure jump across the shear layer. This separated, freely drifting vortex layer affects, in turn, the circulation and the location of the separation points on the airfoil. The velocity field associated with the wakes is calculated by using the familiar Biot-Savart law [61].

3.3.1 Bound and Wake Circulations

As pointed out in equation 2.6, Kelvin's theorem requires that the angular momentum in the flow be preserved. In particular, for a flow with no net torque and zero perturbations at large distances, the theorem states that for all times:

$$\frac{d\Gamma}{dt} = 0$$

where $\Gamma(t)$ is the total circulation along a material curve in the flow. At any instant, a material curve enclosing the body and its wake has zero net circulation because, the same material was far upstream at an earlier time, where the velocity field is uniform with zero vorticity. If $\Gamma_b(t)$ and $\Gamma_w(t)$ represent the bound and wake circulations respectively, then

$$\Gamma = \Gamma_b(t) + \Gamma_w(t)$$

$$\dot{\Gamma}_b(t) + \dot{\Gamma}_w(t) = 0 \tag{3.13}$$

Borrowing the notation used by Sears in [76], let $u_A(y)$ and $u_B(y)$ be the boundary layer velocities at the separation points $x = x_A$ and $x = x_B$ on the upper and lower surfaces respectively. And let U_A and U_B be the corresponding velocities at the boundary layer edges. Also, let $u_{sep.A}$ and $u_{sep.B}$ be the velocities of the separation points at $x = x_A$ and $x = x_B$. Then at any time the amount of circulation shed into the wake, or equivalently the negative of the change in the bound circulation, is:

$$\begin{aligned}\frac{d\Gamma_b}{dt} &= \int_0^{\delta_A} \frac{\partial u}{\partial y}(u_A - u_{sep.A})dy - \int_0^{\delta_B} \frac{\partial u}{\partial y}(u_B - u_{sep.B})dy \\ &= \frac{1}{2}U_A^2 - U_A u_{sep.A} - \frac{1}{2}U_B^2 + U_B u_{sep.B} \qquad (3.14)\end{aligned}$$

where $y = \delta_A$ and $y = -\delta_B$ are the boundary layer edges on the upper and lower surfaces respectively. In the above equation the vorticity in the boundary layer ω, given by

$$\omega = \frac{\partial v}{\partial x} - \frac{\partial u}{\partial y}$$

was approximated by $-\partial u/\partial y$ by ignoring $\partial v/\partial x$.

Though it is true that $\frac{\partial v}{\partial x}/\frac{\partial u}{\partial y}$ is small upstream of the separation location, it is not so in the neighborhood of separation, as explained in equations 3.7, 3.8. But this approximation alone has been used throughout the literature [76, 82, 53, 30, 87, 16] because of the difficulty in modeling analytically the $\partial v/\partial x$ term. Results from experiments [53] indicate that the above approximation is accurate to within 5%, however unlikely it may seem.

The asymptotic theory developed by Dean and Goldstein [19, 31], as indicated before, shows that the terms $\frac{\partial v}{\partial x}$ and $\frac{\partial u}{\partial y}$ are of the same order in the vicinity of the separation point. However, the exact ratio of the two terms depends on the nature of the external flow. Estimates of the ratio $\frac{\partial v}{\partial x}/\frac{\partial u}{\partial y}$ made for one flow would not be applicable for others. In effect, due to the lack of a better model, we also have used the same approximation by neglecting the contribution of $\frac{\partial v}{\partial x}$ to the vorticity in the boundary layer. The validity of this approximation is verified *aposteriori* in chapter 4 as a part of validation of the method.

Clearly, in steady flow, the velocities of the separation points $u_{sep.A}, u_{sep.B}$ and $d\Gamma/dt$ are zero and the above equation becomes identical to Howarth's criterion [36].

In the above equation $U_A - u_{sep.A}$ is the speed at which vorticity is released from the airfoil surface into the external flow. If $u_{sep.A} = 0$, all the vorticity in the boundary layer at the separation location x_A becomes free vorticity. On the other hand, if $U_A = u_{sep.A}$, then the vorticity contained in the boundary layer at the separation location x_A travels at the same speed as the separation point and remains part of the bound vorticity.

A discrete form of the above equation was used to calculate the bound circulation at a new time step using the values from the previous time step of the variables on the right hand side of that equation.

3.3.2 Evolution of the Wakes

In this section the kinematics and dynamics of free convection of the vortical wakes is described, making use of the characteristic variable technique given in [57, 83]. The characteristic variable concept is applicable to fully three dimensional flows and is discussed in more general terms in the references cited above. For our purposes it suffices to confine the discussion to the unsteady covection of two dimensional wake traces.

Kinematics

Helmholtz law [61] (Kelvin's circulation condition can be obtained by integrating Helmholtz equation.) requires that free vorticity Ω in two dimensional incompressible flow obey the equation

$$\frac{d\Omega}{dt} = \frac{\partial \Omega}{\partial t} + \vec{V} \cdot \nabla \Omega = 0 \tag{3.15}$$

where $\vec{V}$ is the total local velocity.

If $\mathcal{A}^1 = \lambda(x, y, t)$ and $\mathcal{A}^2 = \eta(x, y, t)$ are two independent characteristic solutions to the equation

$$\frac{d\mathcal{A}^n}{dt} = 0$$

with appropriate boundary and initial conditions, then, from [11],

$$\Omega(x,y,t) = \Omega(\eta,\lambda)$$

Boundary conditions are specified so that one of these variables, η say, is constant on streaklines (and thus on the airfoil wakes) drawn at fixed time t. The remaining variable λ is then chosen to be the shifted time

$$\lambda = t - \tau$$

so that

$$\frac{d\tau}{dt} = 1$$

and τ is the Eulerian drift time of a wake element

When a concentrated vortex sheet is embedded in an otherwise potential flow (except for the boundary layers) the variables η and λ defined above will generally be discontinuous at the sheet. In such a case it is useful to replace η by a continuous function, η_c say, which instead of $d\eta/dt = 0$ satisfies,

$$\frac{\bar{d}\eta_c}{dt} = \frac{\partial \eta_c}{\partial t} + < \vec{V} > \cdot \nabla \eta_c = 0 \tag{3.16}$$

and

$$\Delta \vec{V} \cdot \nabla \eta_c = 0 \tag{3.17}$$

where

$$< \vec{V} > = \frac{1}{2}(\vec{V}^+ + \vec{V}^-); \;\; \Delta \vec{V} = (\vec{V}^+ - \vec{V}^-)$$

with $\vec{V}^+$ and $\vec{V}^-$ representing the velocity vectors on the upper and lower sides of a wake.

The statement that $\eta_c(x,y,t) =$ constant, then describes a sheet (or streakline) whose deformation is controlled by convection at the mean velocity $< \vec{V} >$ at the sheet. Also, the last equation states that the velocity jump $\Delta\vec{V}$ has no component perpendicular to the sheet at any time, which is one of the boundary conditions appropriate to the evolution of a free vortex sheet.

In the same framework, the second characteristic variable needed at and along the sheet can be chosen to be the mean shifted time

$$\bar{\lambda} = t - \bar{\tau}$$

such that

$$\frac{\bar{d}\bar{\tau}}{dt} = \frac{\partial\bar{\tau}}{\partial t} + < \vec{V} > \cdot\nabla\bar{\tau} = 1 \tag{3.18}$$

where $\bar{\tau}$ represents the mean drift time of fluid elements within the vortex sheet.

The variable $\bar{\lambda}$ provides the coordinate along the wake; in fact, it identifies each fluid element in the wake according to when it left a specified upstream location such as a separation point on the airfoil surface.

Dynamics

If the flow potential above and below a vortex sheet is denoted by ϕ^+ and ϕ^-, then the potential jump

$$\Delta\phi = \phi^+ - \phi^-$$

occuring at the sheet, a function of both x and t, must be determined. In the present case, application of the unsteady Bernoulli equation 2.14 on either side of the sheet, together with the boundary condition that there be no jump in static pressure across the sheet, yields:

$$\frac{\bar{d}}{dt}(\Delta\phi) = \frac{\partial}{\partial t}(\Delta\phi) + < \vec{V} > \cdot\nabla(\Delta\phi) = 0 \tag{3.19}$$

This relation determining $\Delta\phi$ emphasizes the fact that in the presence of a deforming unsteady wake, the boundary-value problem we must solve for ϕ is inherently nonlinear even for the irrotational case. In effect, we must satisfy the condition of zero pressure jump, $\Delta p = 0$, on a surface (a wake) whose shape and location is to be determined as part of the solution. Nevertheless, at each time step, we are able to regard the wake surface as known at that instant, just after its relocation during the previous time step.

Also, note that the variable $\bar{\lambda}$ is automatically produced during the computer time-stepping calculations and requires no extra computation.

Velocity Field of the Wake

Since, as noted before, $\bar{\lambda}$ is a coordinate along the wake, using $\bar{\lambda}$ and complex variable notation, the plane two-dimensional velocity field associated with a wake can be written from the Biot-Savart law [57]:

$$u_w(x,y,t) - iv_w(x,y,t) = w_w(x,y,t) = \frac{1}{2\pi i}\int_0^t \frac{d\Gamma(\bar{\lambda})}{d\bar{\lambda}}\frac{d\bar{\lambda}}{z - z_v} \tag{3.20}$$

Here $z = x + iy$ and $z_v = x_v + iy_v$ is the complex location at time t of the fluid element in the wake having circulation $d\Gamma$. In most of our calculations we encountered two wakes, one emanating from the separation point on the upper surface and the other from the separation point on the lower surface. So, the wake associated velocity at a point $z = x + iy$ is obtained by summing the effects of both wakes.

3.3.3 Numerical Modeling of the Wake

Discretization

A discrete vortex wake model was chosen for its simplicity and ease of computational implementation. This approximation to a vortex sheet has a long history of use by many investigators and has been applied to a variety of problems including the roll-up of trailing edge vortex wakes in the Trefftz plane, the evolution of wakes behind

airfoils in unsteady motion and the formation of vortex wakes over slender wings and bodies [71, 57, 62, 20].

For purposes of carrying out the wake integrals, calculating the Impulse and moment of Impulse and determining the non-explicit contribution of the wakes to the velocity field, a "point-vortex" approxiamtion has been used. That is, the wake elements are treated as if their entire incremental circulation were concentrated at a point. However, for calculating the explicit wake associated velocity, the wake elements are given a small constant vorticity core in order to prevent the occurrence of unrealistically large velocities in the neighborhood of any one vortex.

Hence the incremental complex velocity Δw at a point z associated with a single vortex element of strength $\Delta\Gamma$ having a core radius r_c and located with its center at z_v is biven by

$$\Delta w = \frac{\Delta\Gamma}{2\pi i}\frac{1}{z - z_v}$$

for points outside the core, that is when $|z - z_v| > r_c$ and by

$$\Delta w = \frac{\Delta\Gamma}{2\pi i}\frac{(z - z_v)^*}{r_c^2}$$

when $|z - z_v| < r_c$. Here $()^*$ denotes the complex conjugate value of the quantity inside the parantheses. In this manner the incremental velocity of any particular vortex element is always bounded, *i.e.*,

$$\Delta w \leq \frac{\Delta\Gamma}{2\pi}\frac{1}{r_c^2}$$

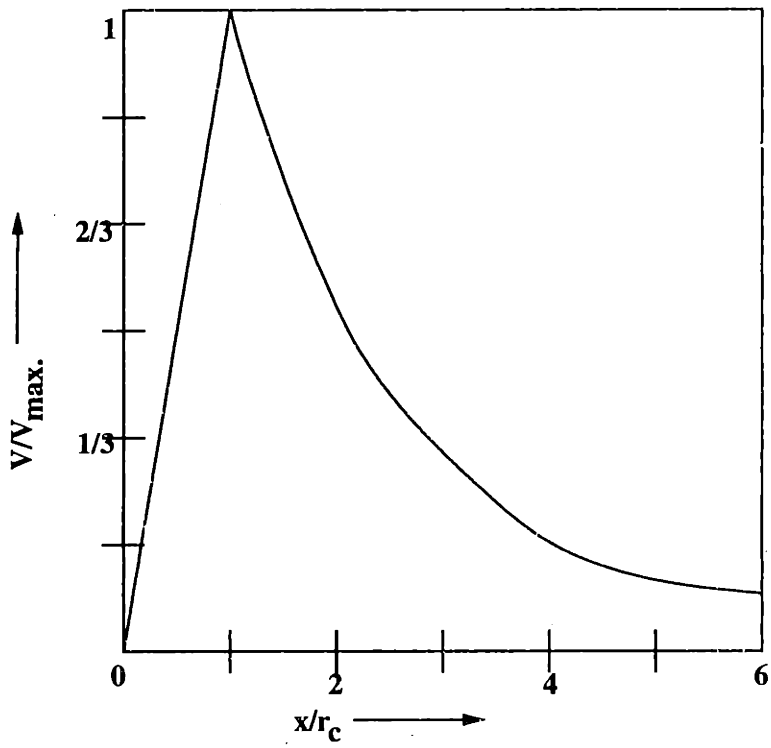

Figure 3.3: Velocity Field of a Rankine Vortex.

This combination of a constant vorticity core with a potential outer flow is of course the well known Rankine vortex. The velocity profile due to such a Rankine vortex is shown in Fig. 3.3.

In the calculations presented, r_c is a user prescribed parameter. It is chosen to be the same for all vortex elements comprising the two wakes and it remains constant in time. (A core size that grows proportional to the square root of time can probably be used tc model the diffusion of a vortex sheet.) For the results to be presented in

the following chapters r_c was chosen such that

$$\frac{r_c}{|w| \Delta t} \simeq 0.5$$

where $|w|$ is the magnitude of the local velocity at which the vortex is placed and Δt is the interval between two consecutive time steps.

The above choice is to some extent arbitrary, but ensures that two consecutive vortices released from the same separation point do not immediately overlap. This particular choice also keeps the vortex sheet being represented by discrete vortices relatively free from instabilities due to machine induced errors.

A row of equidistant point vortices of constant strength is unstable [46] to disturbances of all wavelengths. Whereas, a row of equidistant constant strength vortices with a nonzero core size is neutrally stable to disturbances of wave numbers smaller than a cutoff wave number defined by the strength, radius and spacing of the vortices and unstable to disturbances with wave numbers above the cutoff value [62].

Determining the Position and Strength of New Wake Elements

Positioning the New Elements

The characteristic variable description of the wake traces as described earlier can be used to good advantage in the task of determining where the new wake elements are

to be placed in the flow field. In the present point/finite-core representation of the wake, the j-th vortex of a wake composed of m vortices carries the increments of circulation shed from a separation point in the interval $(j-1)\Delta t \leq \bar{\lambda} \leq j\Delta t$. As such the spatial location of the vortex $z_{v,j}$ is taken to correspond to that of the average value of $\bar{\lambda}_j$ in this time interval, namely

$$\bar{\lambda}_j = (j - \frac{1}{2})\Delta t$$

Alternately, in terms of the previously defined mean drift time $\bar{\tau} = t - \bar{\lambda}$, this point represents

$$\bar{\tau}_j = t - (j - \frac{1}{2})\Delta t$$

It then follows that at time $t = m\Delta t$, before a new vortex has been located to represent the latest addition to the wake, the shifted time field has been mapped in discrete points for values ranging from $\bar{\lambda} = \frac{1}{2}\Delta t$ to $\bar{\lambda} = (m - \frac{3}{2})\Delta t$. This is of course equivalent to mapping the mean drift time field over the interval $\frac{3}{2}\Delta t \leq \bar{\tau} \leq (t - \frac{1}{2}\Delta t)$. In addition, the separation point is where $\bar{\tau} = 0$. Hence all the required information is at hand to locate the mth vortex in the flow field via a consistent scheme of interpolation. The above scheme is equivalent to stating that the new vortex is located on the instantaneous streakline emanating from the separation point.

Strength of New Elements

Referring to the notation used in equations 3.14, the incremental strength of the vortex layer with separtion point at $x = x_A$ on the upper surface is reperesented by a new vortex of strength

$$\Delta\Gamma_A = \Delta t(\frac{1}{2}U_A^2 - U_A u_{sep.A})$$

and the corresponding vortex strength at the separation point $x = x_B$ on the lower surface is

$$\Delta\Gamma_B = -\Delta t(\frac{1}{2}U_B^2 - U_B u_{sep.B})$$

Chapter 4

Validation of the Method

In this chapter we will establish the validity of the method described in the previous chapters by comparing our results for several test cases with those from experiments and calculations by other authors.

4.1 Establishing the Lower Limit on Reduced Frequency

The first issue we want to address here is the range of the reduced frequency within which our method will be applicable. As mentioned in the previous chapter, the

method is an asymptotic approximation, valid in the limit as a number proportional to the square root of the reduced frequency goes to infinity. The physics behind the asymptotic approximation dictates that the approximation is valid when the "Prandtl layer" is much thicker than the "Stokes layer". The boundary layer scaling arguments lead us to the conclusion, continuing with the notation we used in the last chapter, that

$$\frac{\delta_p}{\delta_s} \propto \sqrt{\frac{\omega c}{2U}} = \sqrt{k}$$

When $\delta_p/\delta_s \sim 1$ or lower, the boundary layer can not be divided into distinct "Prandtl layer" and "Stokes layer" and thus the method fails.

This knowledge, however, does not establish the lower limit on k below which the method will not be applicable. It is expected, on the other hand, that the method should be applicable for all higher values of k. This ambiguity associated with the limit on the applicable range of the asymptotic parameter is often encountered in asymptotics [7]. Ultimately, our ability to treat the boundary layer as two distinct layers is based on how distinct the physics of the two layers are. Since, as explained in the previous chapter, the two layers are controlled by distinct physical phenomena, we expect the lower limit on k to be quite low, in fact, a value corresponding to $\frac{\delta_s}{\delta_p} \simeq 1$.

4.1.1 Using the Convergence Characteristics

One way to establish this limit, a widely used one [7], is to see the convergence characteristics of the solution as k is varied.

In order to investigate this limit on k, we have chosen the case of a thin ellipse of slenderness 1/20 placed at an angle of 5^o in an otherwise spatially uniform unsteady stream oscillating by 4% in magnitude but not in direction The solution to this problem was calculated for $k = 4.5$ by Gioulekas [30] using a different representation for the wakes and the potential flow. The Reynolds number is 10^5.

We have calculated the solution for this problem for a range of values of k. The calculation procedure, followed for all problems described in this work, is presented in the previous chapter. The results of our calculation are presented in Fig. 4.1 where we have plotted the number of iterations taken for convergence for several values of k. Here the ratio of the value of C_L calculated at the end of an iteration to the converged value is interpreted as the level of convergence. Note that as k increases, the length of the wake after the same number of cycles of oscillations becomes shorter and shorter, as the drift time allowed for the wake decreases.

Also shown in the same figure is the convergence behavior of a dynamic stall problem to be discussed in the next few chapters. This case involves a modified[1] NACA 0012

[1]The blunt trailing edge was made sharp by tangentially extending the surface contours and

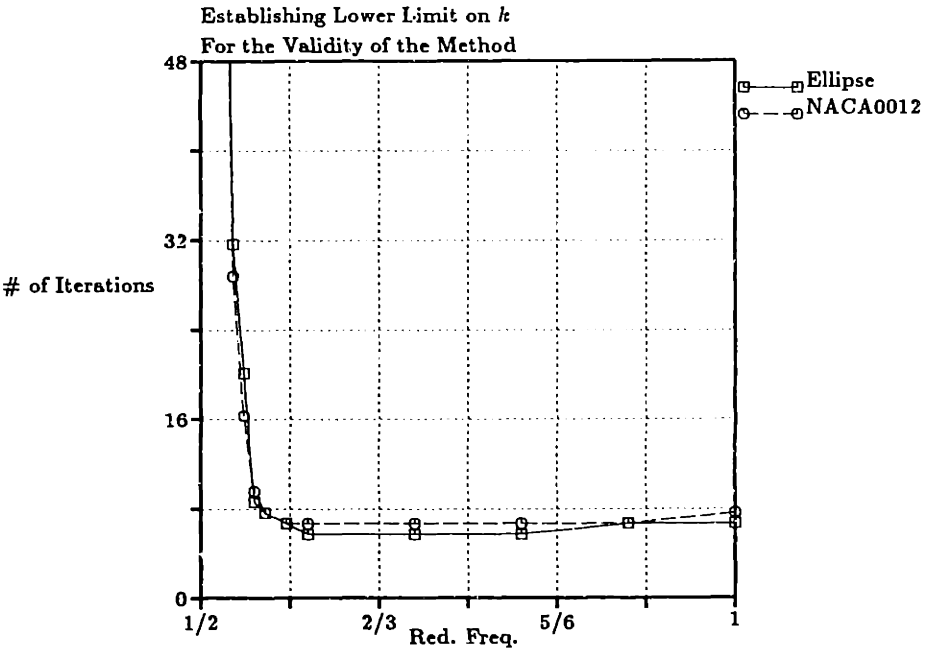

Figure 4.1: Lower Limit on Red. Freq. $k \simeq 0.56$. No convergence was achieved for $k \leq 0.52$. Number of iterations necessary for convergence increase sharply for $k \leq 0.55$.

airfoil oscillating sinusoidally in heave such that its equivalent angle of attack[2] varies between 6^o and 18^o in a flow at $Re = 10^5$.

It turned out that in most of the problems we have encountered, eight iterations were sufficient to reach "convergence", except where noted. Whether the method is converging to the correct value or not is a different question, to be settled by comparing our results with experiments and other calculations. An effort towards that end follows. But first we will estimate the value of δ_s/δ_p for $k = 0.52$, the lower limit on k for which convergence was achieved.

4.1.2 Estimation of δ_s/δ_p as a Function of k

Consider the simple case of a flat plate oscillating sinusoidally parallel to its length at an angular rate ω with a magnitude U_s in an otherwise steady freestream of velocity U_p aligned with the length of the plate. The flow is depicted in Fig. 4.2.

The "Prandtl thickness" of the boundary layer that develops on the plate at a distance x downstream of the leading edge can be shown, from simple boundary layer analysis

---

rescaling the chord to one unit.

[2]Please see the chapters 6 & 7 for an explanation.

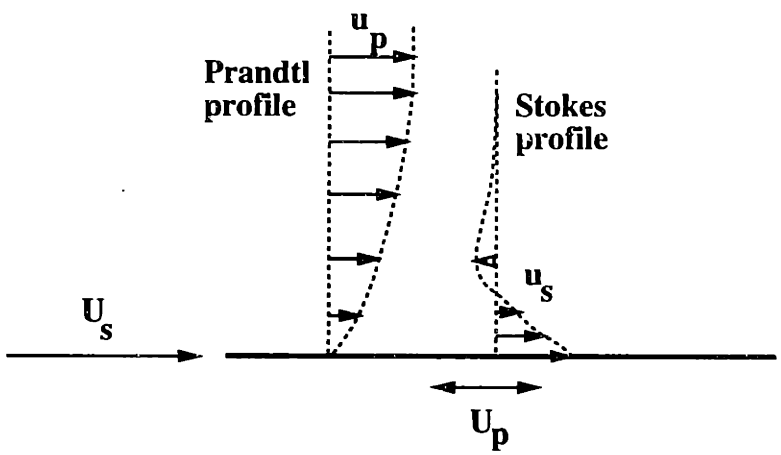

Figure 4.2: Illustration of Stokes and Prandtl profiles on an oscillating flat plate in a freestream.

[72] as well as the method described in the previous chapter, to be

$$\frac{\delta_p}{x} \simeq \frac{5}{\sqrt{Re}}$$

where "Prandtl layer" edge is taken to be the point of 99% freestream velocity.

The "Stokes velocity" $u_s(y,t)$, except in region close to the leading edge[3] of the plate is given by [72]

$$\frac{u_s}{U_s} = e^{-\sqrt{\frac{\omega}{2\nu}}y} \cos\left(\frac{\omega x}{U_p} - \sqrt{\frac{\omega}{2\nu}}y\right)$$

Defining the edge of the "Stokes layer" as the point where the magnitude of the velocity envelope is 1% of U_s and using $k = \frac{\omega x}{2U_s} = 0.52$, we get

$$\frac{\delta_s}{\delta_p} = 0.31 \tag{4.1}$$

It is now clear that this simple estimation procedure justifies the claim we made above. It is useful to note that when U_s is larger, for example around the leading edge suction peak, the Prandtl layer will be thinner, so the above ratio will be larger and the approximation will be less accurate. On the other hand, in the vicinity of a stagnation point $U_p \to 0$, so $\frac{\delta_s}{\delta_p} \to 0$. Therefore the current approximation can be quite accurate locally, in that region.

We will now turn to some comparisons of the results of our calculations to those from experiments and calculations by other authors.

[3]Here "close" can be interpreted as a distance of the order of the Stokes layer thickness δ_s.

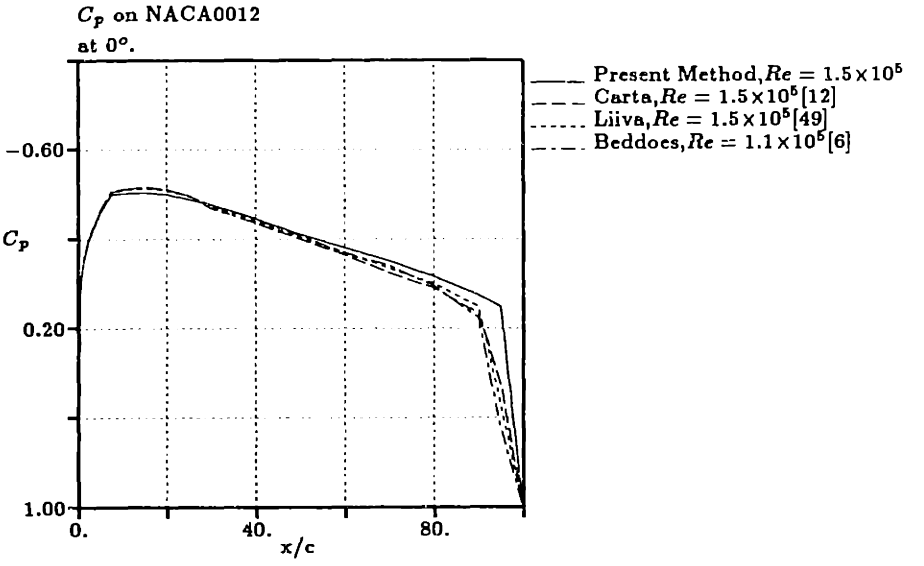

Figure 4.3: Pressure Distribution on NACA 0012 at 0^o Incidence, $Re = 1.5 \times 10^5$.

4.2 Steady Viscous Cases

We will first show our results for some steady calculations and compare them to existing experimental and calculations' results depending on availability.

4.2.1 Viscous Flow on a NACA 0012 Airfoil

First case is the pressure distribution on a NACA 0012 at zero degrees angle of attack. The calculation was done at $Re = 1.5 \times 10^5$. The results are shown in Fig. 4.3. Superimposed on our results are some experimental and numerical results as annotated. All these tests were carried out at different Reynolds numbers as indicated

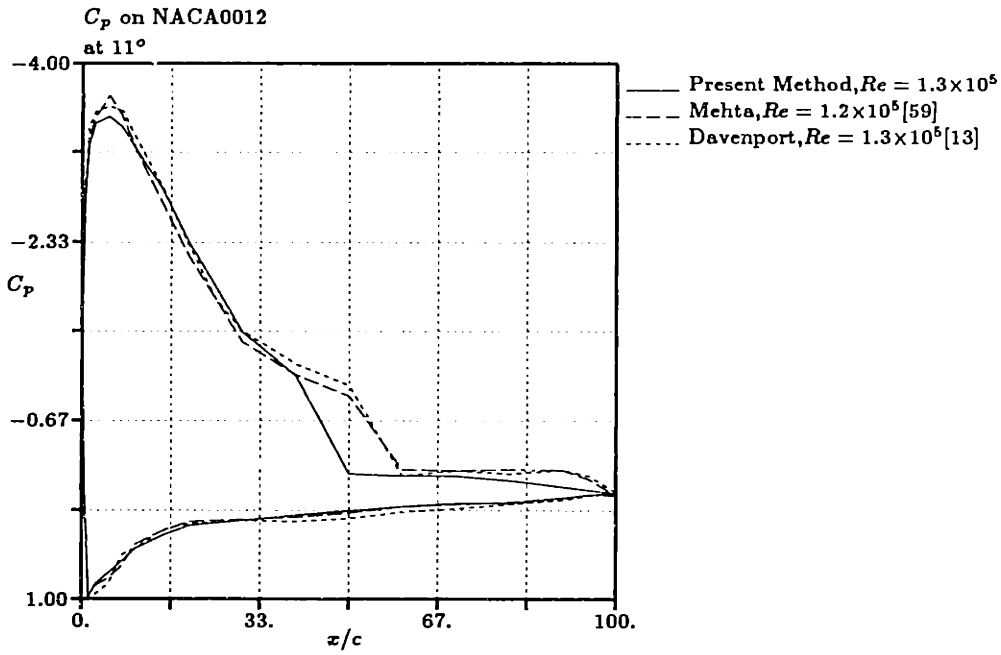

Figure 4.4: Pressure Distribution on NACA 0012 at 11° Incidence, $Re = 1.3\times10^5$.

in the figure. The sudden increase in the pressure at 97% of the chord is due to flow separation.

The next test case, shown in Fig. 4.4, is the flow over a NACA 0012 at 11° angle of attack. Again results from experiments Davenport [12] and calculations by Mehta [59] are superimposed. Our calculation shows flow separation at 47% of the chord, whereas the finite difference calculation and the experiment show separation at 52% of the chord. The Reynolds number corresponding to each source of result is indicated in the figure. Our calculation was performed at $Re = 1.3\times10^5$ to permit a reasonable comparison.

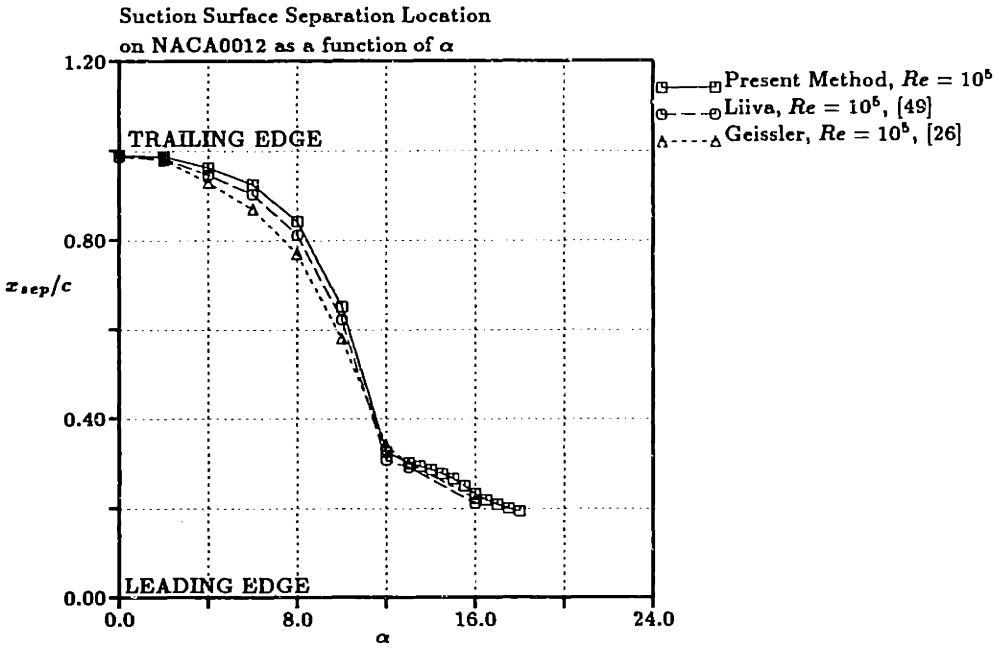

Figure 4.5: Location of Steady Separation Point on the Upper Surface of NACA 0012 as a Function of Incidence Angle, $Re = 10^5$.

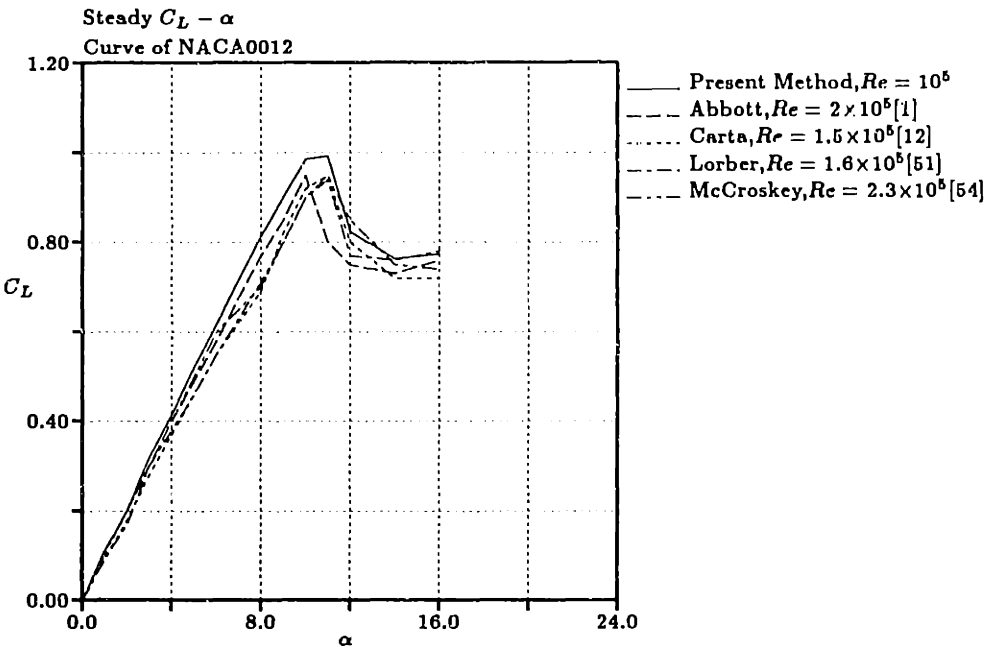

Figure 4.6: Steady lift coefficient of NACA 0012 as a function of incidence angle at $Re = 10^5$

Next, the locations of the steady separation point for a range of incidence angles were calculated and shown in Fig. 4.5. All the existing results available in the literature are also presented in the figure for comparison. Note that all these tests were conducted at different Reynolds numbers as noted in the figure.

In the next test, the steady NACA 0012 lift coefficient as a function of incidence angle is compared with existing results in Fig. 4.6.

In Fig. 4.7 we have shown the calcualated pitching moment coefficient about the quarterchord. Also shown in the same figure are results from experiments by Fukushima

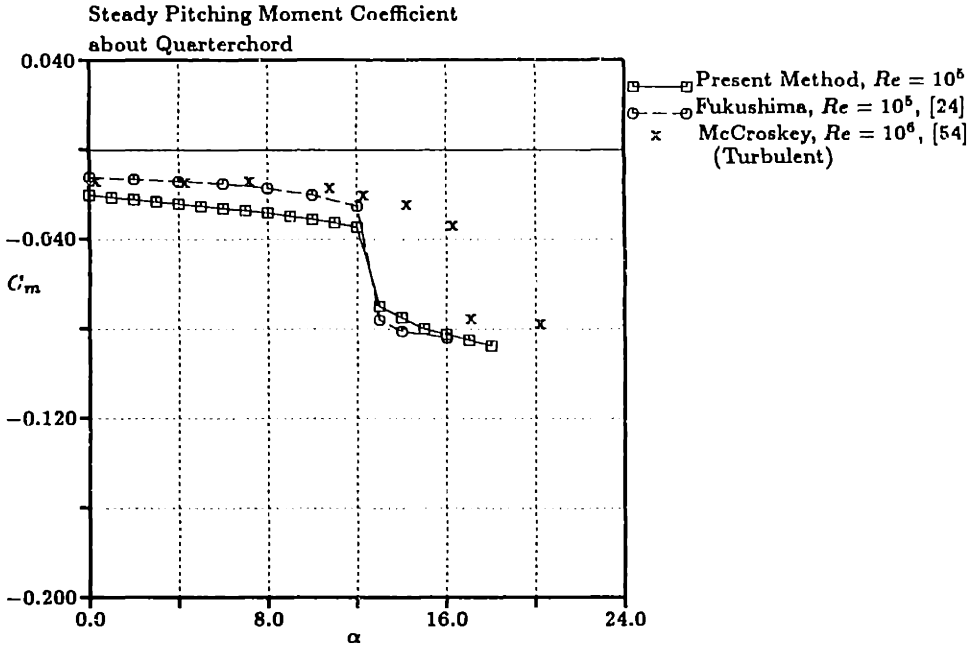

Figure 4.7: Steady Pitching Moment about Quarterchord for NACA 0012 as a function of incidence angle at $Re = 10^5$

[24] and McCroskey [54]. McCroskey's results are for turbulent flow.

4.2.2 Viscous Flow Over a Cylinder

We calculated the viscous flow over a circular cylinder at $Re = 1.7 \times 10^5$ and compared it with the classical results from the experiments of Flachsbart [72]. The results are shown in Fig. 4.8. Also shown in the figure is the pressure coefficient distribution for potential flow over the cylinder. The Reynolds number in Flachsbart's experiment was also 1.7×10^5.

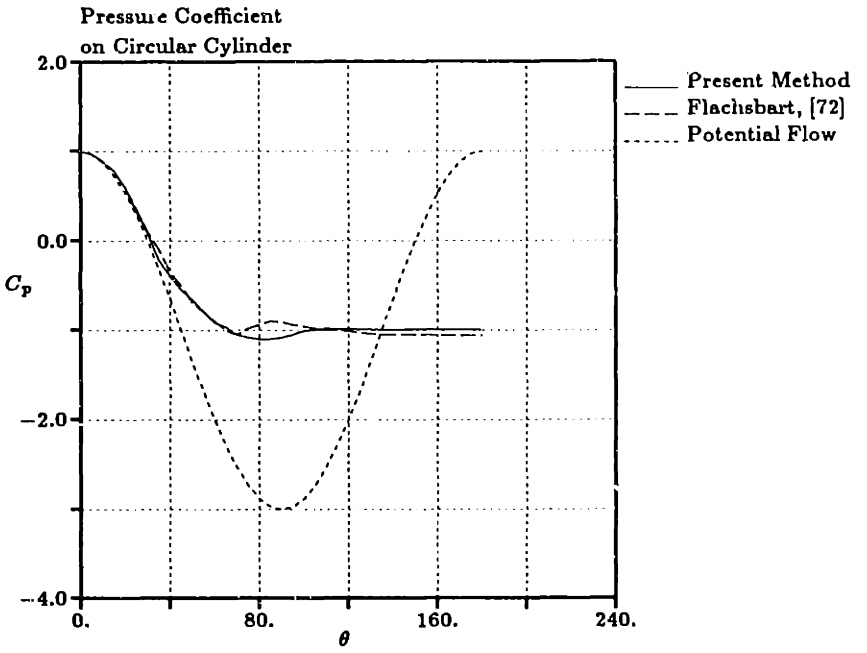

Figure 4.8: Pressure Distribution on a Circular Cylinder at $Re = 1.7 \times 10^5$

4.3 Unsteady Potential Cases

The present method becomes, when the boundary layer analysis option is not exercised, equivalent to a nonlinear unsteady potential method for analyzing the motion of two dimensional airfoils of arbitrary shape with flow separation at any two points on the airfoil to be prescribed by the user. No restrictions on the type of motion or the reduced frequency need be imposed.

The first test we have chosen here is the sinusoidal oscillation in plunging of an airfoil at various reduced frequencies. It is assumed here that the flow is smooth over the

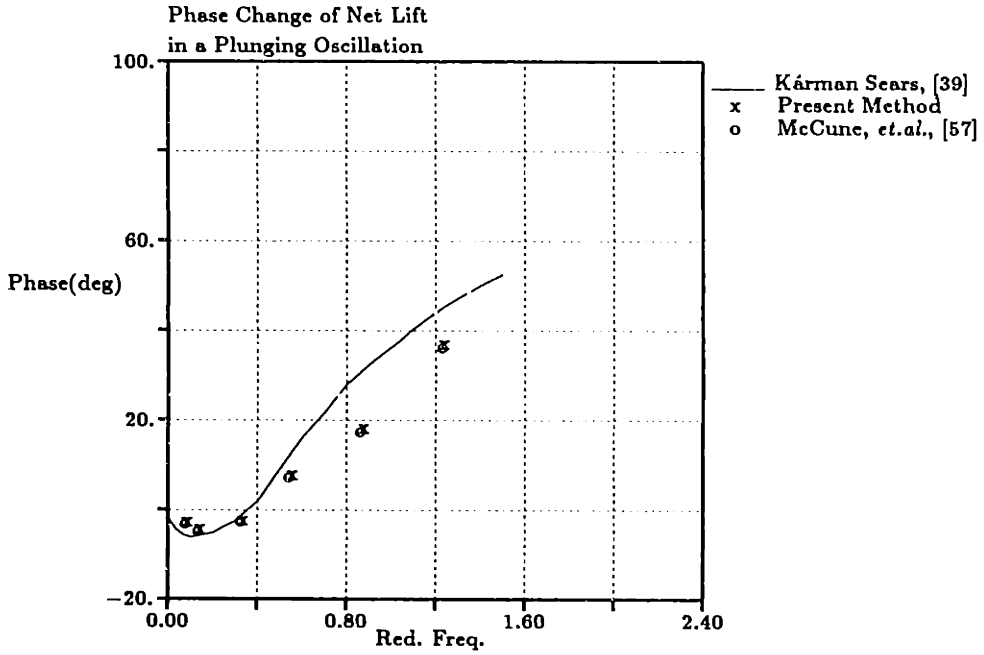

Figure 4.9: Phase change of net lift on an airfoil oscillating in heave.

body and separates only at the trailing edge. The phase of the net lift is plotted in Fig. 4.9 and compared with results from McCune *et. al.* [57] and from the classical linear theory of von Kárman and Sears [39]. Observe that our results are identical to those from [57]. This is because our method becomes, when applied to unsteady potential cases, identical to the one used in [57] except for numerical details. We have elected to test our calculation of the lift-phase, because the phase is very sensitive to inaccuracies [57, 75].

Next, we considered the problem of a flat plate, undergoing pitching oscillations at a reduced frequency $k = 0.3$ such that its angle of incidence changes between 10^o and

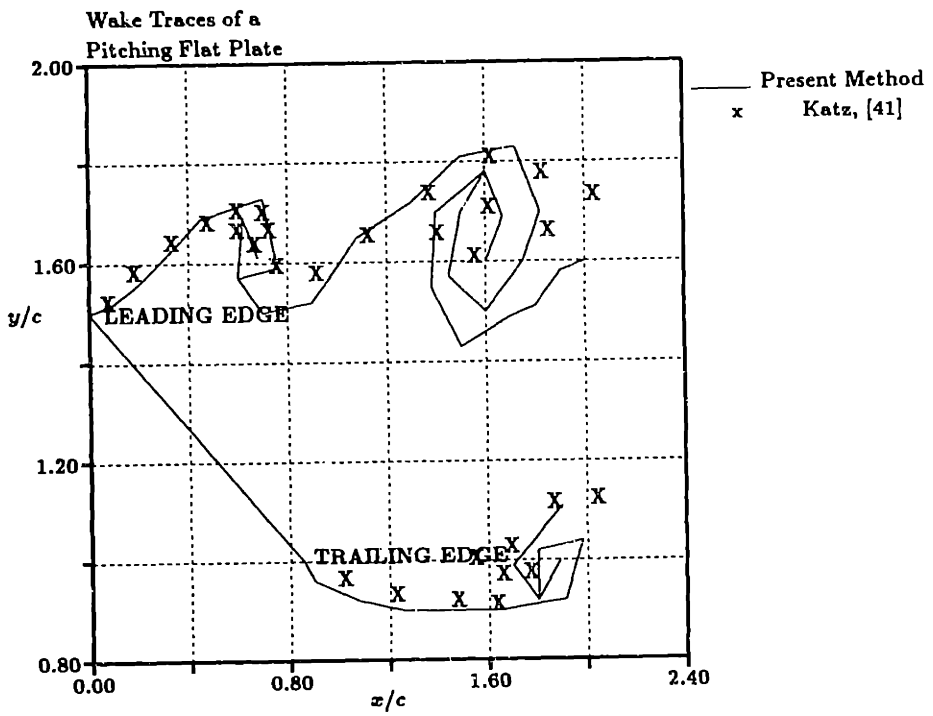

Figure 4.10: Traces of the wakes being shed from the leading and trailing edges of a flat plate pitching at $k = 0.3$ between 10° and 30°.

30° in an otherwise spatially and temporally uniform stream. A trace of the evolution of the wakes from the leading and trailing edge is shown at an instant when the the nominal incidence is 30° in Fig. 4.10. Results from [41] for the same problem are superimposed for comparison.

4.4 Unsteady Viscous Calculations

It has been very hard to find experiments on unsteady viscous flows of the type that we can compare our results to.

The first one we will compare our data with was performed by Mathioulakis and Telionis [53]. In this experiment an ellipse of smoothness ratio 2.96 was placed at 14° inclination in a freestream that oscillates sinusoidally in magnitude by 10% but not in direction. The Reynolds number of the flow was 1.4×10^4 and the reduced frequency was 0.455. Significant amount of data was presented in their paper and the unsteady velocity measurements "near" the suction surface separation point were the most quantitative.

We performed calculations for a flow that was identical to the one described in the above experiment except that the reduced frequency in our calculations was 0.56, the

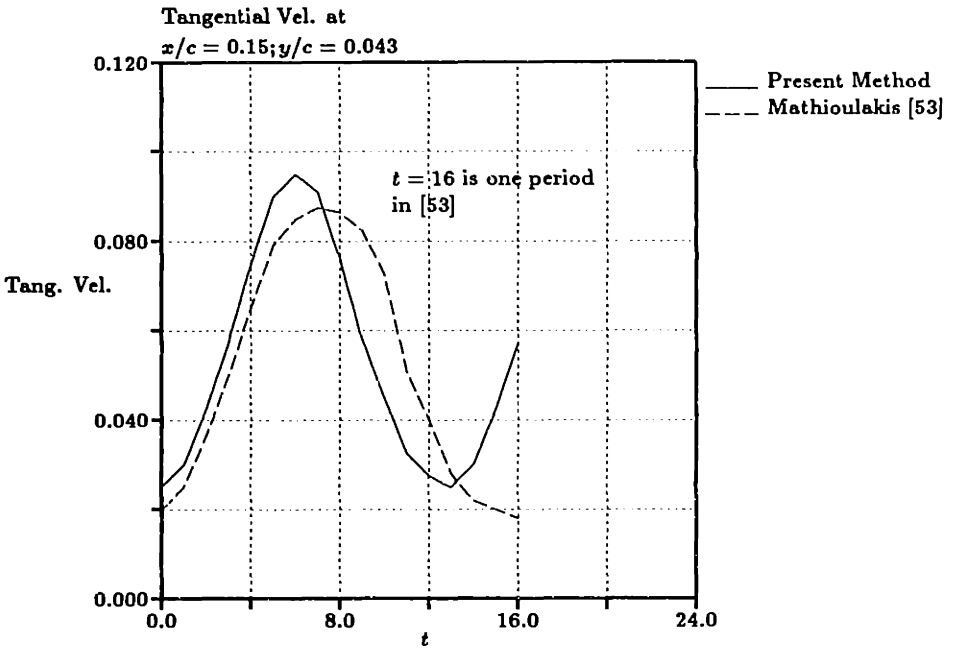

Figure 4.11: Tangential velocities at $x/c = 0.15, y/c = 0.043$ on an ellipse of 2.96 smoothness placed at 14^o in a stream oscillating 10% in magnitude. $Re = 1.4 \times 10^4$. $k = 0.455$ in the experiment, $k = 0.56$ in our calculation.

minimum achieved[4] in our method. We have presented our results in Fig. 4.11 and those from [53]. The tangential velocity is given as a fraction of the mean freestream value.

The next result presented here is the movement of the separation point on a NACA 0012 airfoil oscillating in pitch at a reduced frequency $k = 0.6$ in a $Re = 10^5$ flow

[4]Please see the first section of this chapter.

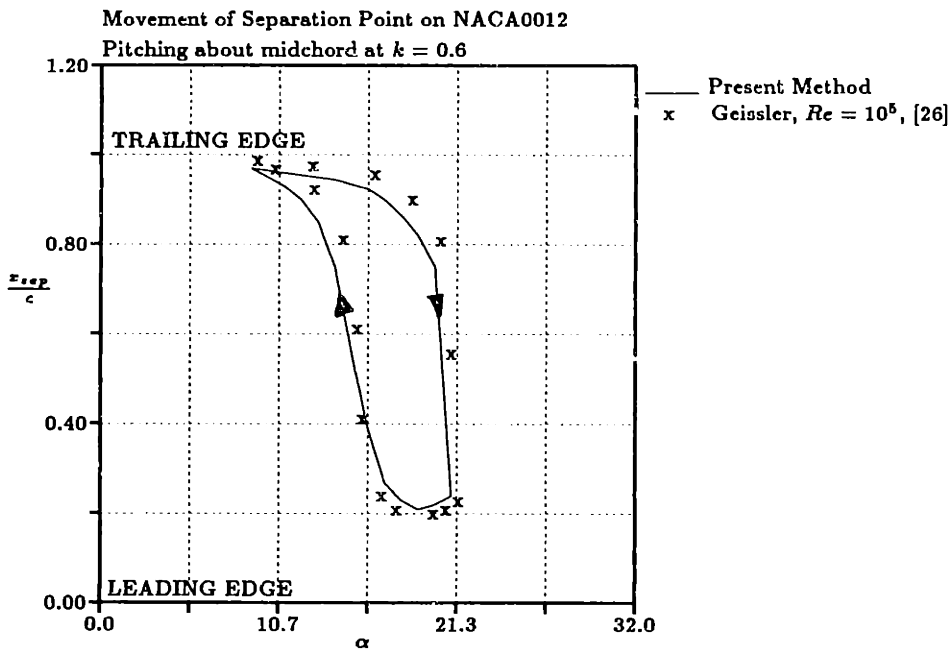

Figure 4.12: Comparison of the movement of suction surface separation point on a NACA 0012 airfoil pitching sinusoidally about its midchord at $k = 0.6$ between 9^o and 21^o, $Re = 10^5$.

such that its nominal incidence angle[5] changes sinusoidally from 9^o to 21^o. The choice of this particular set of parameters permits a comparison with the finite difference calculations performed by Geissler [26]. The results are shown in Fig. 4.12.

[5]Please see the next chapter for a discussion on nominal angle of attack.

4.5 Appraisal of the Method

From the comparisons presented in the previous sections one can place fair amount of confidence in the accuracy of the present method. It is clearly demonstrated that the method calculates accurately steady viscous and unsteady potential flows. There are very limited experiments or computations done on unsteady viscous flows that are in the same range of flow parameters as we are interested in. It is reasonable to conclude, though based only on the limited comparisons we have performed, that the present method seems to perform fairly accurately when applied to unsteady viscous flows also.

In the next chapter we will present the results of our calculations on a NACA 0012 pitching under various conditions.

Chapter 5

Dynamic Stall of a Pitching Airfoil

In this chapter we will present the results of our calculations on a NACA 0012 airfoil pitching under various conditions. First we will describe the characteristics of the flow around the airfoil undergoing rapid sinusoidal pitching oscillations. The pitching oscillation is designed so that the maximum nominal angle of incidence on the airfoil exceeds its static stall angle and the reduced frequency is "high". The effects of varying the rate of pitching and the axis of pitching on the structure and evolution of the flow will be considered next.

5.1 Flow Structure on an Airfoil in Pitch Induced Dynamic Stall

Consider a NACA 0012 airfoil pivoted at midchord in an otherwise spatially and temporally uniform stream and pitching sinusoidally such that its nominal angle of incidence is given by

$$\alpha(t) = \bar{\alpha} + \tilde{\alpha}\sin(\omega t) \tag{5.1}$$

where, as before, $\alpha(t)$ is the instantaneous nominal angle of incidence, $\bar{\alpha}$ is the time average of $\alpha(t)$, $\tilde{\alpha}$ is the magnitude of the oscillation and ω is the rate of oscillation measured in radians per second. For the results presented in this section, we have chosen the following flow parameters:

$$\begin{aligned} \bar{\alpha} &= 12^o \\ \tilde{\alpha} &= 6^o \\ Re &= 10^5 \\ k &= 0.6 \end{aligned} \tag{5.2}$$

Recall that the calculated value of the steady stall angle of incidence for NACA 0012 is 12.4°. At the beginning of the pitch-up phase of the airfoil oscillation cycle, *i.e.*, when the nominal angle of incidence is around 6° and increasing, the flow on the upper surface separates at $1 - 2\%$ upstream of the trailing edge and the flow on the

lower surface remains fully attached. In fact, the lower surface separation point never moves from the trailing edge to any significant degree throughout the oscillation cycle and so the following discussion does not concentrate on the movement of the lower surface separation point.

In this part of the oscillation cycle, the amount of negative (clockwise) vorticity shed into the wake from the upper surface is smaller than the positive (counterclockwise) vorticity shed from the lower surface (trailing edge) into the wake. Thus a net amount of positive vorticity is shed into the wake consistent with the increasing bound ciruculation on the airfoil. At the same time, the upper surface separation point starts to move upstream while the lower surface separation point exhibits no such inclination to move from the trailing edge. The movement of the separation point is shown in Fig. 5.1. It can be observed that the location of the suction surface separation point on the oscillating airfoil is well downstream of that on a stationary airfoil at any given angle of incidence, in this part of the oscillation cycle. The negative pressure peak observed at the leading edge is larger than that on a stationary airfoil at the same angle of incidence and this difference grows as the airfoil pitches further up, as shown in Fig. 5.4. The evolving pressure distribution on the upper surface of the airfoil will be disscussed in much greater detail later.

No further significant developments take place in the flow structure until the airfoil angle of incidence reaches 13^o. By this time, the suction surface separation point has

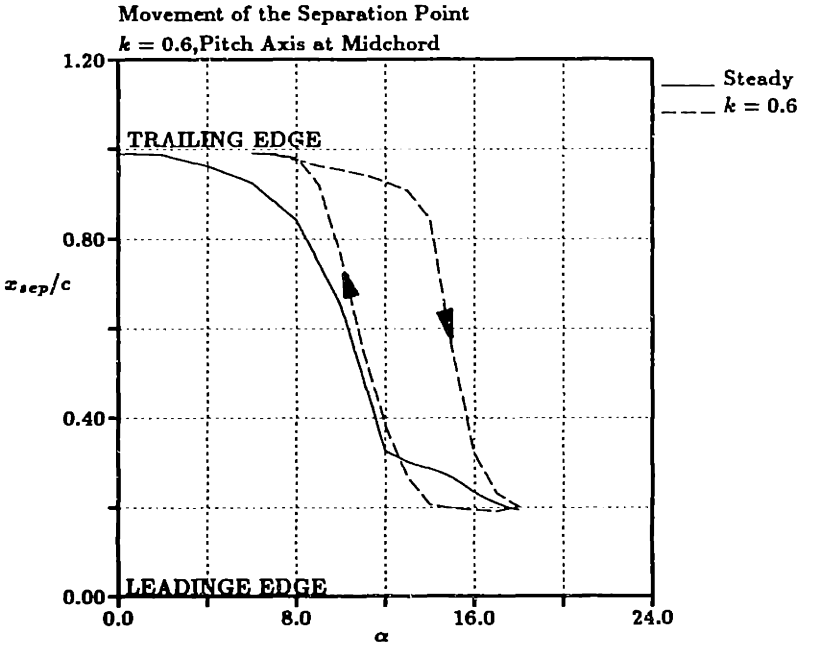

Figure 5.1: Movement of the suction surface separation point on NACA 0012 pitching about midchord at $k = 0.6$, $Re = 10^5$.

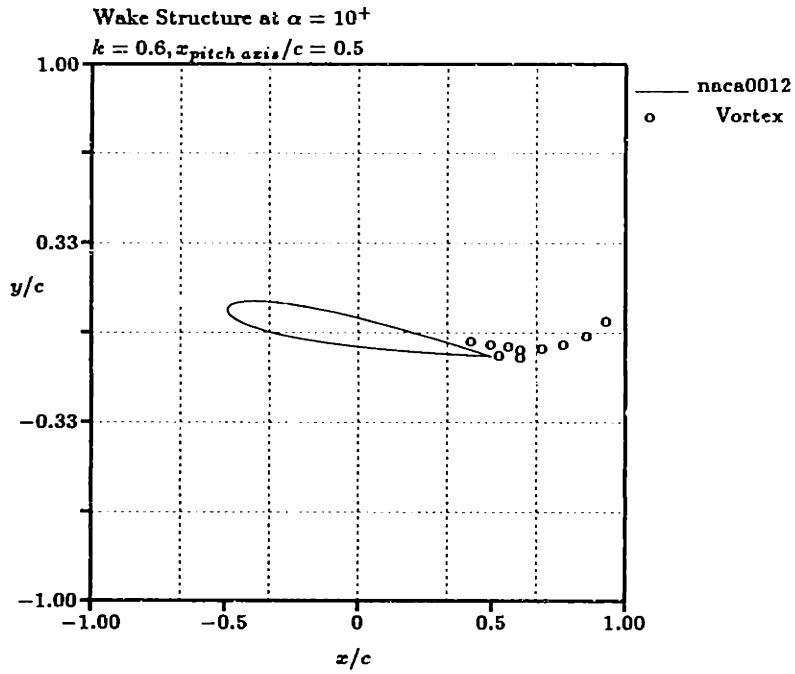

Figure 5.2: Early stages of the evolution of wakes on a NACA 0012 oscillating in pitch. The airfoil is pitching up and its present angle of incidence is $\alpha = 10^o$.

travelled upstream to 20% of the chord from the trailing edge and the net strength of the positive vorticity being shed into the wake has increased.

The wake structure of this evolving flow is shown in Figs. 5.2 and 5.3. The wakes, as mentioned earlier, are modeled by discrete vortices. Fig. 5.2 shows the wakes when $\alpha = 10^o$ and increasing; and Fig. 5.3 presents the wake pattern when $\alpha = 14^o$ and increasing.

But by the time the airfoil has pitched up to $\alpha = 14^o$, an angle well above the static stall angle, the flow structure has significantly deviated from what would exist on a

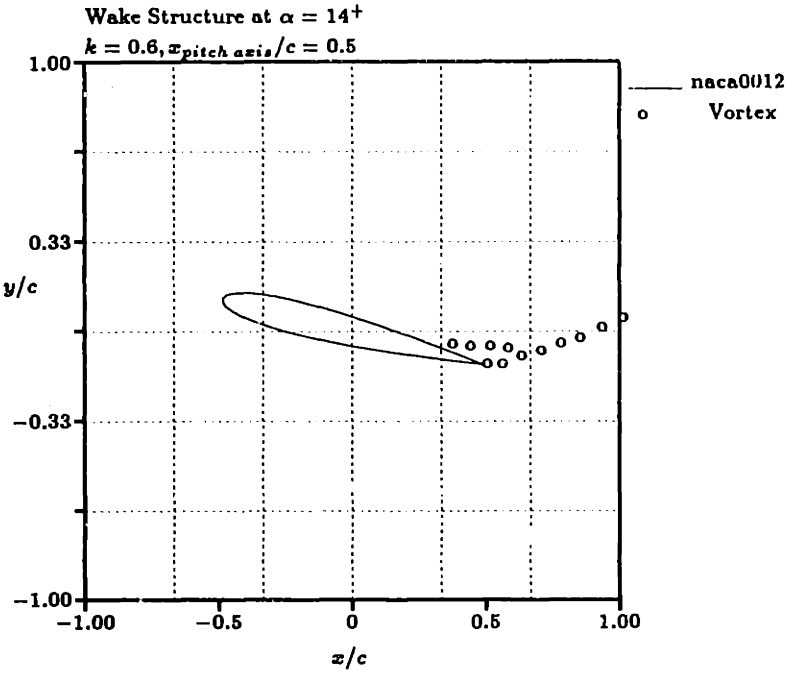

Figure 5.3: Wake pattern on a NACA 0012 oscillating in pitch. The airfoil is pitching up and its present angle of incidence is $\alpha = 14^o$. Observe that the airfoil shows no signs of stalling at 14^o, even though its static stall angle is 12.4^o.

steady aifroil at similar angles of incidence. These deviations are, as can be seen from Fig. 5.3: the separation on the upper surface lags far behind the steady separation point. Consequently the lift is much higher and the moment is smaller on the pitching airfoil than the lift and moment, respectively, on a stalled steady airfoil. In fact, in this phase (nose-up pitch) of the oscillation cycle, the lift and moment on the pitching airfoil are closer to those on an airfoil undergoing a similar motion in inviscid flow (with Kutta condition) than those on a steady airfoil in viscous flow at the same instantaneous angle of incidence [87, 54, 18] as shown in Fig. 5.5.

The lift and the pitching moment for the present are presented in Figs. 5.5 and 5.6. Corresponding results for steady viscous flow and unsteady inviscid flow assuming Kutta are also included to aid comparison.

Shortly after the angle of incidence exceeds 15°, the upper surface separation point moves upstream quite rapidly and reaches 20% of the chord from the leading edge by the time the angle of incidence reaches 17°, as shown in Fig. 5.1.

As the separation point on the upper surface moves towards the leading edge from the trailing edge, an increasingly larger fraction of the total lift on the airfoil is concentrated in the forward portion on the airfoil. This is because, while high suction exists near leading edge area, there is a large pressure recovery on the upper surface aft of the separation point and so this portion of the airfoil does not contribute

significantly to the total lift. These observations can be seen from the surface pressure, lift and moment variations during the oscillation cycle shown in Figs. 5.4, 5.5 and 5.6, respectively.

The pressure coefficient on the upper surface at several angles of incidence is shown Fig. 5.4. The subscripts $+, -$ in the figure indicate whether the airfoil is pitching up or down, respectively. The second peak in negative pressure appearing in the surface pressure profiles corresponding to $\alpha = 16^-, 14^-$ and 10^- will be explained shortly.

The variation of the lift on the airfoil for a complete oscillation is shown in Fig. 5.5. Observe that the lift keeps increasing until the angle of incidence reaches 18°, its maximum value. The behavior of the lift when the airfoil pitches down will be explained below.

The behavior of the pitching moment (calculated about the quarter chord point) during the oscillation cycle is shown next in Fig. 5.6. In this picture, nose-down moment is positive and nose-up moment is negative.

The free shear layer emanating from the upper surface separation point starts to accumulate over the airfoil when the angle of incidence reaches 17°. The free shear layer modeled by discrete vortices starts to roll-up into a large vortex noted by many in the literature [34, 75, 51, 12], *etc.*, as the "primary vortex" or the "dynamic stall vortex".

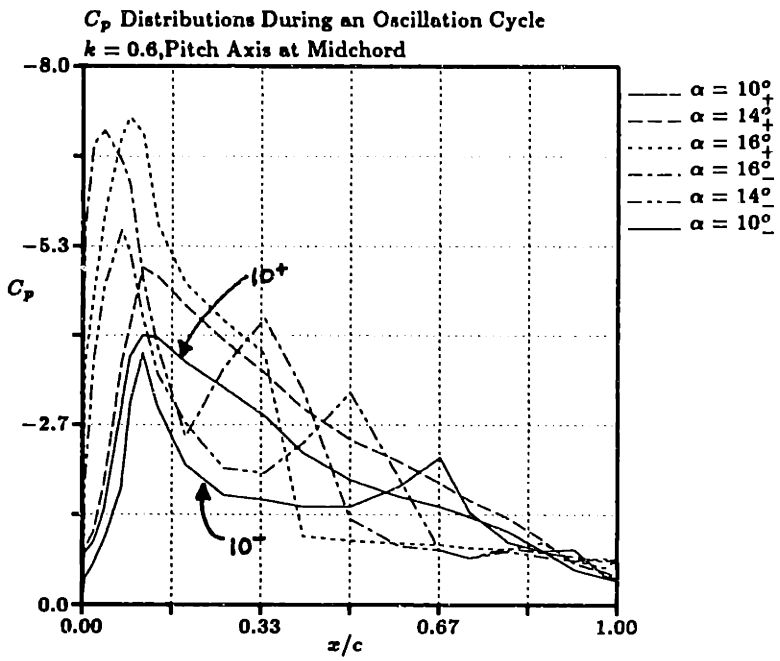

Figure 5.4: Variation of the Pressure Coefficient on the upper surface of NACA 0012 at various angles of incidence. The airfoil is pitching about its midchord at $k = 0.6, Re = 10^5$. The superscripts$+, -$ indicate whether the airfoil is pitching up or down, respectively.

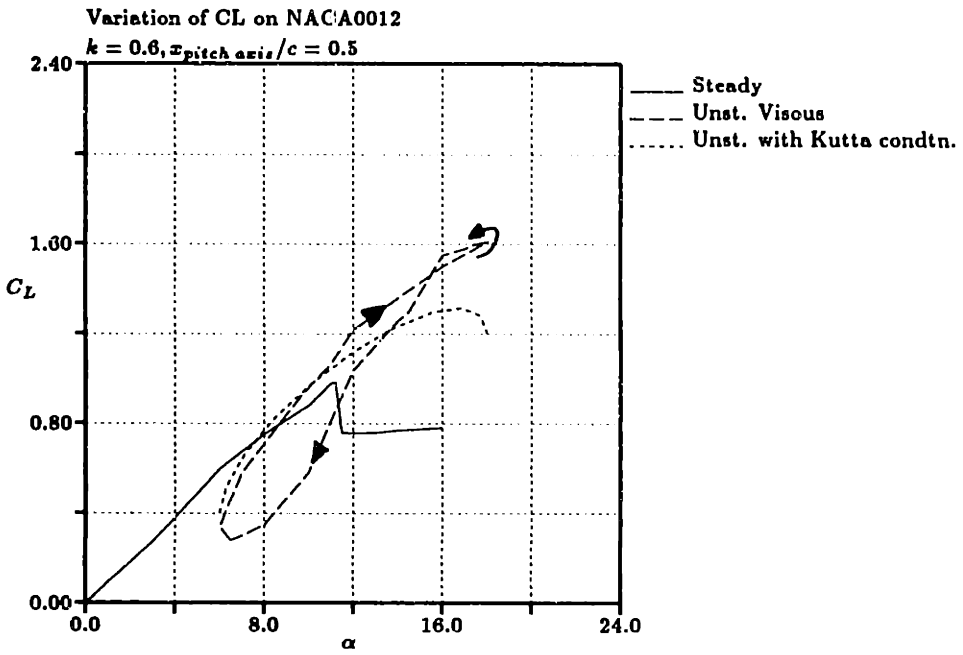

Figure 5.5: Variation of the Lift Coefficient on a NACA 0012 as a function of angle of incidence. The airfoil is pitching about its midchord at $k = 0.6, Re = 10^5$.

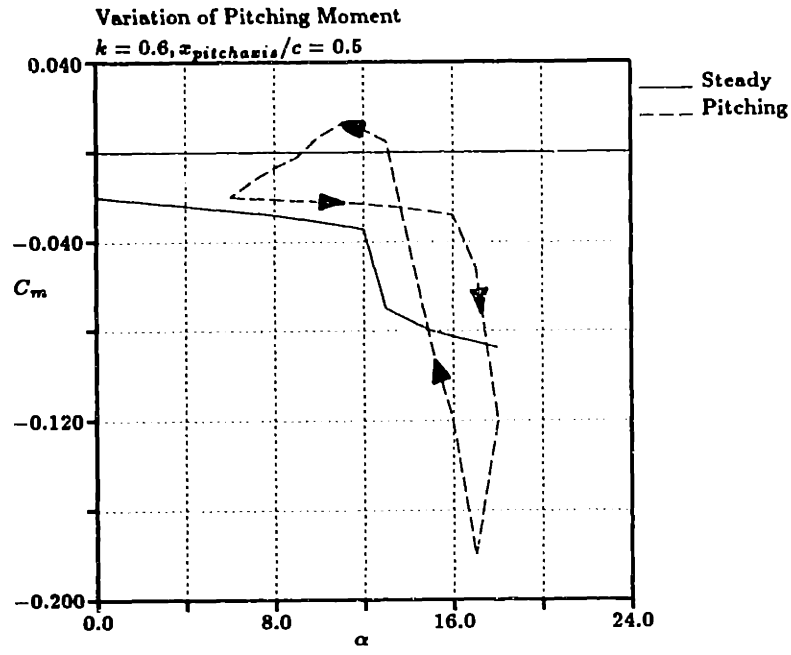

Figure 5.6: Variation of the Moment Coefficient on a NACA 0012 as a function of angle of incidence. The airfoil is pitching about its midchord at $k = 0.6, Re = 10^5$. The pitching moment is measured about the quarter chord point of the airfoil.

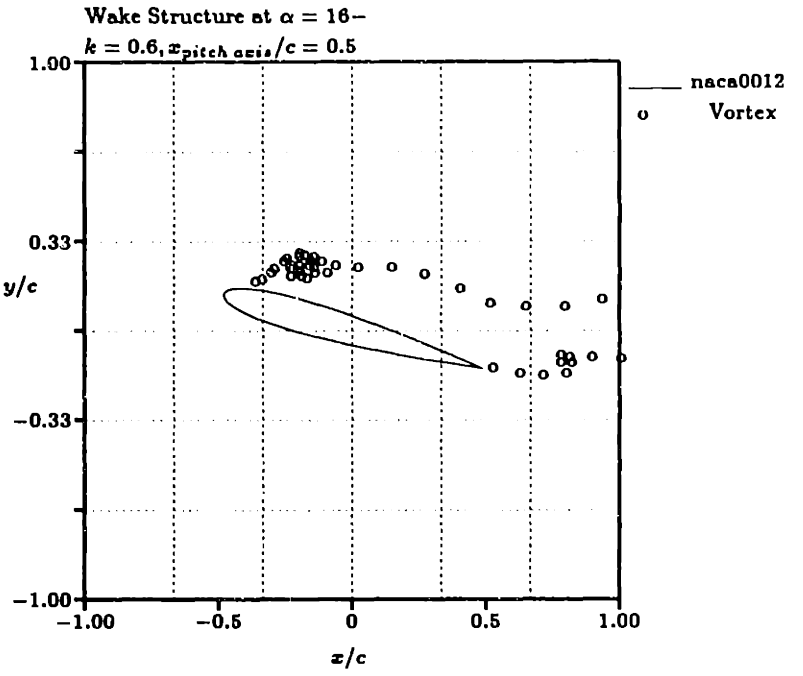

Figure 5.7: Structure of the wake at $\alpha = 16^o$ when the airfoil is pitching down. The Primary Vortex resulting from the roll-up of suction side shear layer, and a much smaller vortex due of the pressure side shear layer roll-up can be observed.

The structure of the wake inculding the primary vortex is shown in Fig. 5.7 when the airfoil angle of incidence is 16^o and decreasing.

The strength of the primary vortex $\Gamma_{p.v.}$ can defined as the sum of the circulation of the vortices contained in the rolled-up portion of the vortex layer. The definition of the primary vortex is some what arbitrary, because there is no precise way to decide which vortex is in the "rolled-up portion" of the shear layer and which is not, except by eye, or by judgement. Nevertheless, to quantify $\Gamma_{p.v}$ in the present model, we have

included in the primary vortex the part of the separated shear layer that is beyond the point at which the shear layer first becomes tangential to freestream.

If the rolled-up portion of the vortex layer contians n discrete vortices, each of strength $\Delta\Gamma$, then

$$\Gamma_{p.v.} = \sum_{i=1}^{n} \Delta\Gamma_i \tag{5.3}$$

where the subscript i indicates the i-th vortex in the rolled-up portion of the vortex sheet. Please see Fig. 5.8 for an illustration. From this illustration and from the above definition of the primary vortex, one can define a reasonable value of "n" and in general $n = n(t)$.

The location $(x_{p.v.}, y_{p.v.})$ of the primary vortex can be defined such that the impulse of the system of vortices contained in the rolled-up portion of the free vortex sheet matches that of the primary vortex. Thus, if (x_i, y_i) are the coordinates of the i-th vortex, then

$$\begin{aligned} x_{p.v} &= \frac{1}{\Gamma_{p.v.}} \sum_{i=1}^{n} (x_i \Delta\Gamma_i) \\ y_{p.v} &= \frac{1}{\Gamma_{p.v.}} \sum_{i=1}^{n} (y_i \Delta\Gamma_i) \end{aligned} \tag{5.4}$$

Observe that, according to this definition, the location of the primary vortex as defined above is identical to the centroid of vorticity of the vortex system under consideration. The strength and location of the primary vortex as defined above do not allow for the

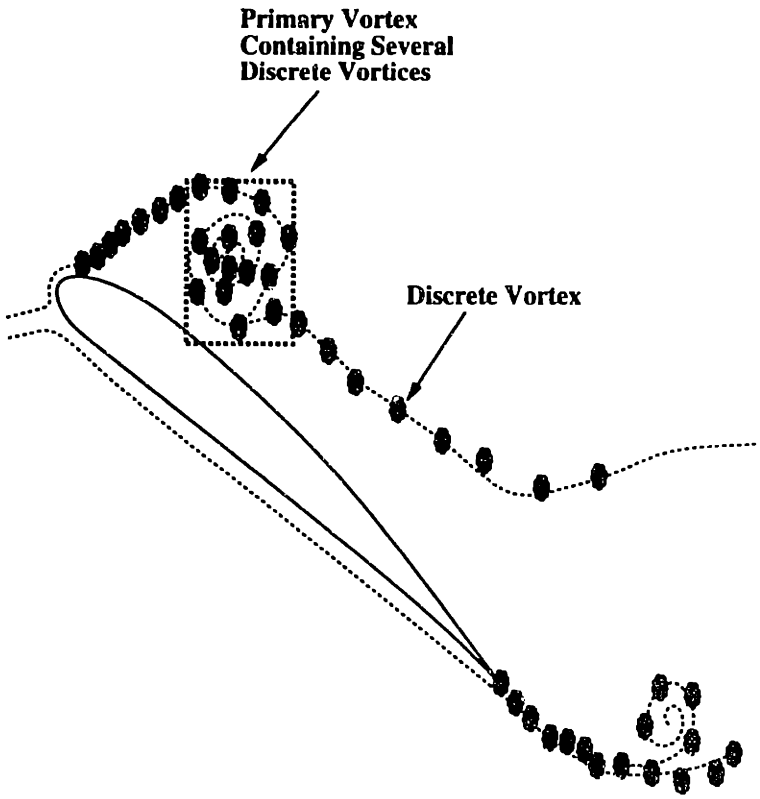

Figure 5.8: Illustration of the definition of the Primary Vortex.

moment of imulse of the primary vortex to match that of the discrete vortex system. In fact, it turns out that if we were to require that the first and all higher moments of the impulse (along with total circulation and impulse) of the original vortex system be preserved in the new vortex system we are seeking to find, then the new system must contain the same number of vortices as the old one.

Using the above definitions for the strength and location of the primary vortex we are able to track its evolution and movement.

The primary vortex continues to drift downstream while it also grows in strength for a short while after the airfoil reaches its maximum nominal angle of incidence. At around the point when the incidence reaches 16^o while the airfoil is pitching down, the primary vortex breaks off from its feeding sheet. It then continues to drift downstream, at a speed only slightly higher than that when it was attached to its feeding sheet. The streamwise drift speed of the primary vortex is shown as a function of time normalized by unit convection time in Fig. 5.9.

This figure needs a little explaining. The horizontal scale is the time nondimensionalized by unit convection time:

$$\tau = \frac{tU}{c}$$

Using the above definition and that of the reduced frequency, k, equation 5.1 can be

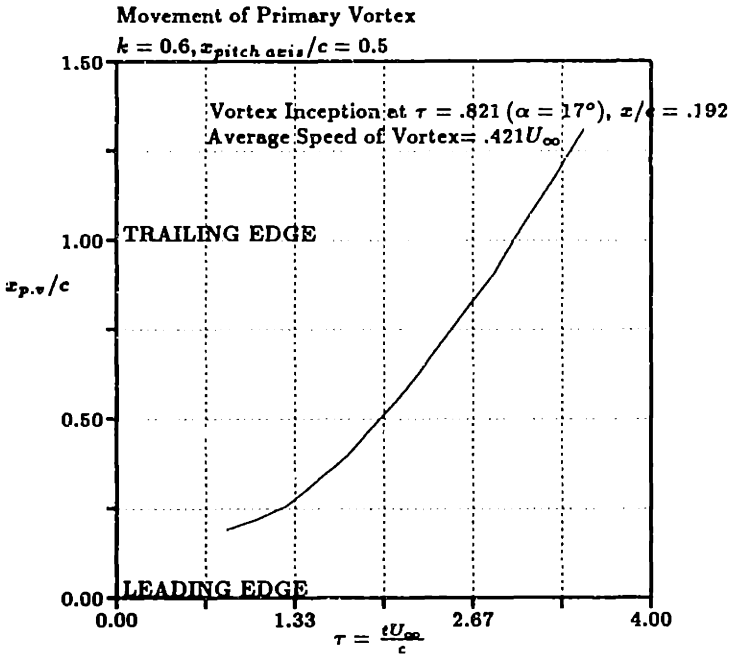

Figure 5.9: Movement of the Primary Vortex as a function of time nondimensionalized by unit convection time c/U. $\tau = 0$ corresponds to $\alpha = 12°$ and increasing; $\tau = 1.309$ corresponds to $\alpha = 18°$; $\tau = 2.618$ corresponds to $\alpha = 12°$ and decreasing; $\tau = 3.927$ corresponds to $\alpha = 6°$.

rewritten as:

$$\alpha = 12° + 6° \sin(2k\tau) \tag{5.5}$$

Thus we can identify the orientation α of the airfoil at any given time τ. For example, $\alpha = 17°$ and increasing, corresponds to $\tau = 0.821$. It is the time at which the primary vortex first appears. $\tau = 3.927$ is the time at which the airfoil completes the cycle of oscillation and reaches $\alpha = 6°$.

The suction surface separation point remains in the neighborhood of the leading edge until the angle of incidence decreases to 15° ($\tau = 2.182$) when the airfoil is pitching down. It then moves downstream rather quickly to about 85% of the chord by the time the angle of incidence reaches 10° after which it slowly creeps further towards the trailing edge. These changes can be seen in Fig. 5.1.

The lift on the airfoil continues to increase, as shown in Fig. 5.5, until the airfoil reaches its maximum nominal incidence 18° with no signs of stalling. This is because, as shown in Fig. 5.1, the separation point remains well behind the vicinity of the leading edge until $\alpha = 16°$. So the flow on the airfoil remains essentially attached and unstalled resulting in large increments in lift beyond the static stall value.

Even after the airfoil starts to pitch down, as shown in Fig. 5.9, the primary vortex stays in the neighborhood of the leading edge and maintains a large low pressure area in its surroundings. This explains the second peak in negative pressure appearing in the surface pressure profiles corresponding to $\alpha = 16^-, 14^-$ and 10^- in Fig. 5.1. As the angle of incidence decreases from 16° to 10° the pressure peak drifts downstream indicating that the primary vortex is traveling downstream. The position of the primary vortex and the wake structure at $\alpha = 10°$, when the airfoil is pitching down, are shown in Fig. 5.10.

It can be seen from Fig. 5.5 that the lift on the airfoil does not decrease abruptly

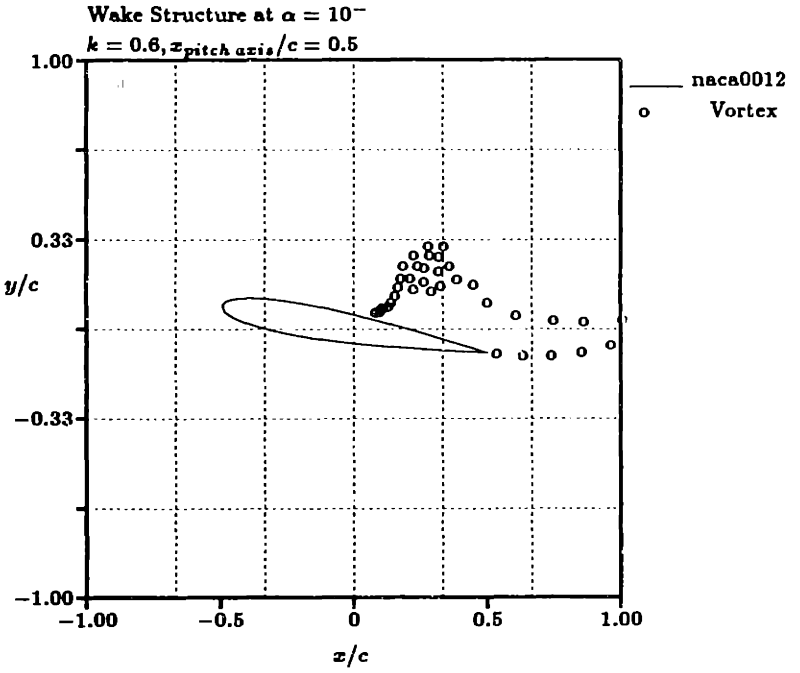

Figure 5.10: Structure of the wake and the position of the primary vortex at $\alpha = 10°$ when the airfoil is pitching down.

as the airfoil starts to pitch down from $\alpha = 18^o$ even though flow separation now occupies most of suction surface. Due to the transient low pressure region created on the suction surface by the traveling primary vortex, the lift on the airfoil remains close to its maximum even after the separation point has traveled all the way up to the leading edge. As the primary vortex drifts downstream, its transverse distance from the airfoil increases. Therefore the intensity of the low pressure casued by its presence diminishes. So its contribution to the total lift on the airfoil decreases. But at same time the separation point on the airfoil also moves towards the trailing edge, thus regaining more and more lift on the airfoil. The combination of the these two conteracting effects is that the lift on the airfoil drops only gradually when the airfoil is pitching down from its maximum nominal incidence.

If the rapidity of the airfoil motion was much less, *i.e.*, if k were small enough so that no roll-up of the suction-side shear layer occurs, the primary vortex wound not exist, so the related low pressure region would not be present and then one would expect the lift on the airfoil to drop as soon as the airfoil starts to pitch down from its maximum incidence. This kind of flow behavior can in fact be observed in all of the experiments conducted [12, 49, 54, 51] in which $k \leq 0.15$.

We are now in a position to explain the moment diagram also. When the airfoil is pitching up, the suction side separation point remains near the trailing edge until $\alpha = 13^o$. Therefore pitching moment remains small and negative. But as soon as

the separation point jumps to the vicinity of the leading edge at around $\alpha = 17^o$, most of the lift on the airfoil is due to the small unseparated region near the leading edge and the presence of the primary vortex in the neighborhood of the leading edge. Therefore the pitching moment plunges to a large negative value. After the airfoil starts to pitch down, the travelling primary vortex passes the quarter chord point (about which moments are measured) and so the pitching moment starts to recover. The pitching moment becomes positive at $\alpha = 13.1^o$ during the pitch down phase of the oscillation, indicating that more of the lift is due to the presence of the primary vortex, which by now, has travelled past the quarter chord point. Soon after, the moment starts to decrease and becomes negative, as the contribution of the distant primary vortex to the total lift becomes smaller and smaller.

The airfoil has now completed a full cycle of oscillation during which it has produced the most interesting and exciting flow phenomena as presented above. Because of the limitations of the method that we have adopted, some of the flow phenomena observed in dynamic stall experiments such as the leading edge bubble formation, flow transition to turbulence, secondary separation, shock wave and its interaction with the boundary layer, etc., are not captured in the above discussion. Nevertheless, our simple and fast method is able to predict all the essential features of dynamic stall.

5.2 Effects of increasing the Reduced Frequency on Dynamic Stall phenomena

In this section we will investigate how changing the reduced freqency affects the flow behavior on a pitching airfoil. Calculations were performed for $k = 0.9, 1.2$, in addition to $k = 0.6$. The results are presented below and the effects of varying the reduced frequency on various flow features are discussed.

A considerable of body of experimental literature describing the effects of varying the reduced frequency on dynamic stall phenomena exists [22, 89, 37, 52], *etc.* However most of these experiments were conducted at lower ($k \leq 0.3$) reduced frequencies and on airfoils pitching up at a constant rate. Our calculations are compared with all the available relevant experimental results.

Since the processes of diffusion and convection of vorticity, which establish the circulation or lift on the airfoil, require finite time, the main effect of increasing the reduced frequency is a delay of dynamic stall events. This is an angular delay and not a time dalay.

First the movement of the separation point is tracked and is plotted in Fig. 5.11 for all the three different reduced frequencies under consideration.

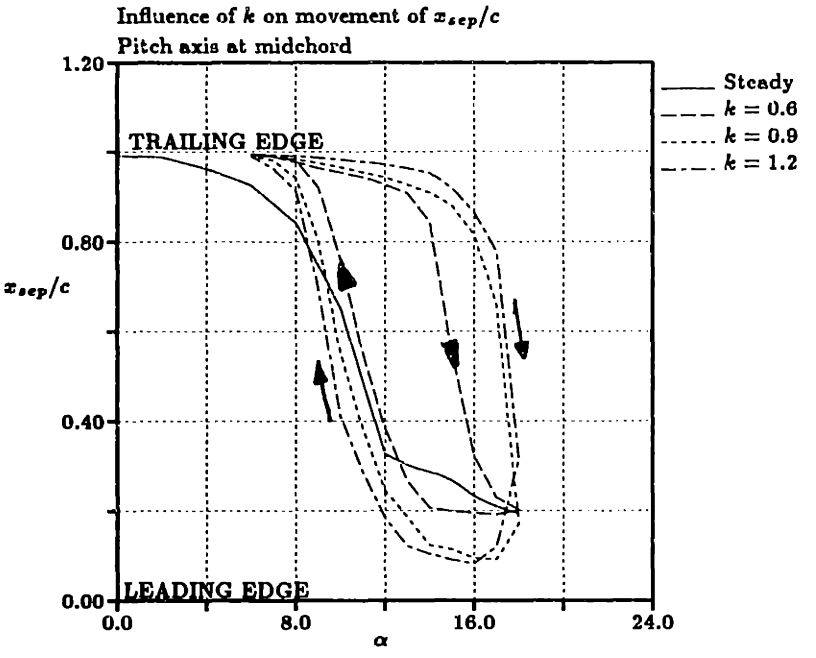

Figure 5.11: Effect of varying k on the movement of the suction surface separation point during a pitching oscillation of a NACA 0012. The axis of Pitching is situated at midchord.

It can be observed that during the intial poriton of the pitch-up phase *i.e.* when $\alpha = 6 - 14°$, the separation point propagates upstream at an increasingly smaller rate as the reduced frequency increases. In other words, there is an *angular* delay in the onset of dynamic stall due to an increment in k. The reason for this pattern is the fact that as the reduced frequency increases at the same Reynolds number, the ratio between the time scales associated with diffusion and unsteadiness decreases. On the other hand, the propagation of the separation point during the last part of the pitch-up phase, *i.e.* when $\alpha = 15 - 18°$, becomes more abrupt with increasing frequency. It can also be seen from this figure that as the reduced frequency increases, the separation point stays in the vicinity of the leading edge, for longer angular intervals, but not necessarily longer time intervals.

It can also be observed from the same figure that, when the airfoil is pitching down, downstream movement of the reattachment point on the upper surface occurs at a slower rate as the reduced frequency is increased. The reason for this becomes apparent when we present the changes in the evolution of the primary vortex due to increasing the frequency. Both these results are in qualitative agreement with experiments mentioned above. Quantitative comparison is not possible, because these experiments were conducted at much lower k and constant rate of pitch in turbulent flows.

As a consequence of the delay in the upstream propagation of the separation point

during the pitch-up part of the cycle, the onset of formation of the primary vortex is delayed also. Again, it should be emphasized that this is an angular delay, not necessarily a temporal delay. It is also observed that the angular duration for which the primary vortex is attached to its feeding sheet, *i.e.*, the duration for which it grows in strength, decreases as the reduced frequency increases. Fig. 5.12 shows the formation and evolution of the primary vortices for the three reduced frequencies. The numerical values are summarized in the following table.

Red. Freq. (k)	Inception time ($\tau = \frac{Ut}{c}$)	Inception Angle (α)	Ave. Speed ($\frac{U_{vortex}}{U}$)	Strength ($\frac{\Gamma_{p.v.}}{Uc}$)
0.6	0.8211	$17^{o,+}$	0.421	0.592
0.9	0.8727	18^{o}	0.378	0.763
1.2	0.8423	$17.4^{o,-}$	0.365	0.865

The reason for this is that, while the propagation speed of the separation point is governed by the evolution of the boundary layer structure (viscous phenomena) as well as variations in the external flow (convective phenomena), the drift speed of a vortex placed in the neighborhood of an airfol is largely independent of the viscous effects. Therefore, the primary vortex responds more readily to changes in k than does the propagation characteristic of the separation point. In other words, as the reduced frequency increases the angular delay in the onset of formation of the primary

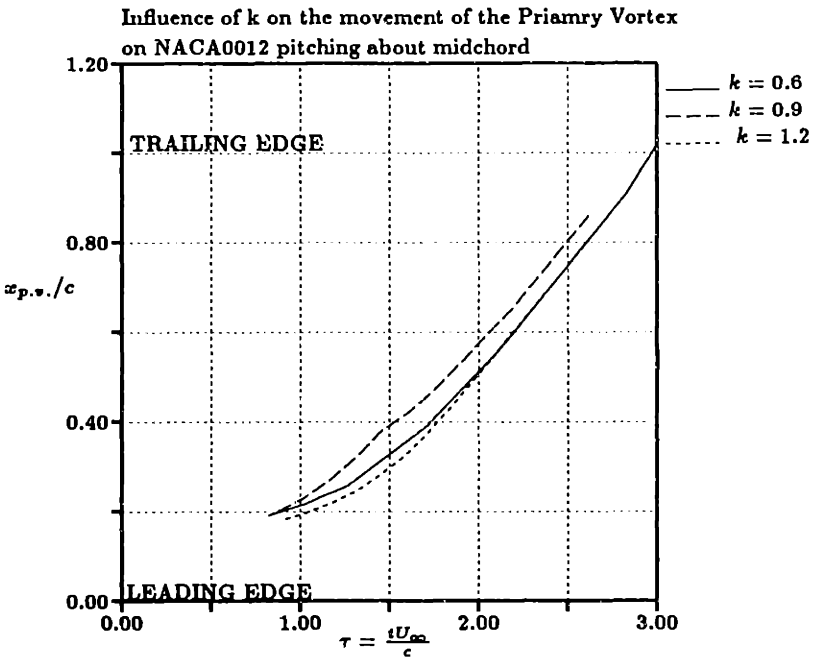

Figure 5.12: Effect of increasing k on the evolution of Primary Vortex.

vortex is larger than the angular delay in the time at which the primary vortex stops growing in strength.

The strength of the primary vortex increases as the reduced frequency increases. Please see Fig. 5.13 where we have plotted the strength of the primary vortices for all three reduced frequencies under consideration. While the fact that the duration for which the primary vortex remains attached to its feeding sheet decreases with increasing frequency tends to decrease the strength of the vortex, the higher external velocity and the larger negative $C_{p_{max}}$ attained at the leading edge due to increasing reduced frequency, tend to add to the strength of the vortex.

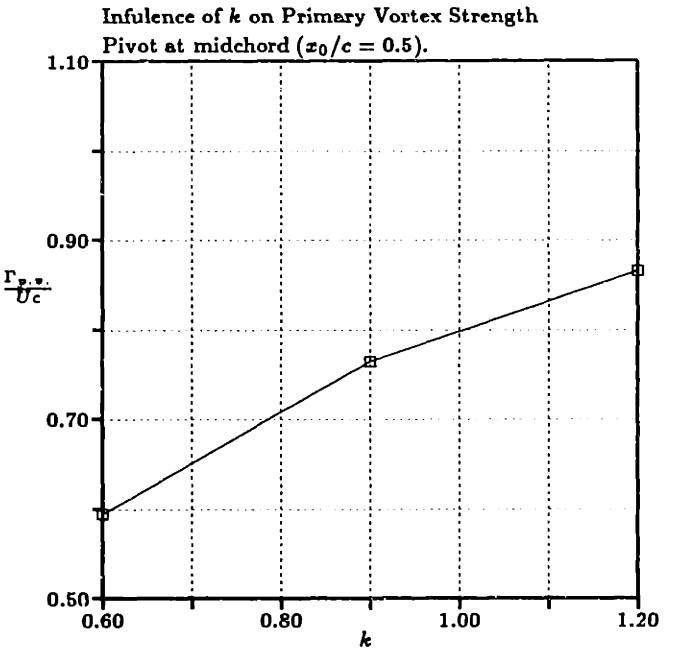

Figure 5.13: Variation in strength of the primary vortex due to increasing k.

Also, as the reduced frequency increases, the separation point penetrates closer to the leading edge and so the location of primary vortex inception moves close to the leading edge, as shown in Fig. 5.12. The reason for this is that as the frequency increases, the negative pressure peak reached at the leading edge becomes stronger, for example as shown in Fig. 5.15. Aft of the negative pressure peak, the pressure recovery (adverse pressure gradient) also intesifies with increasing frequency. This causes the movement of the separation point to be more abrupt (as mentioned earlier) and its penetration deeper towards the leading edge. The increasing upstream penetration of the separation point with increasing reduced frequency also tends to work in favor of increasing the strength of the primary vortex.

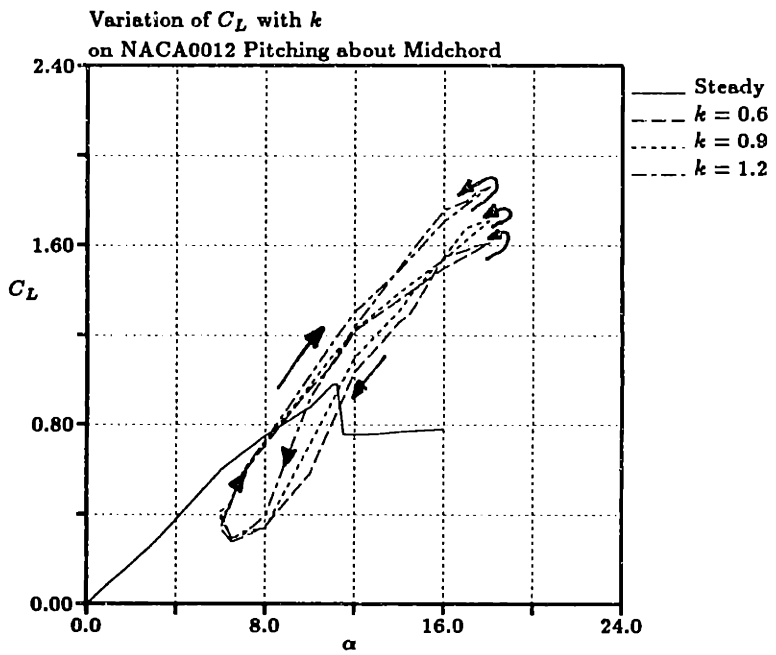

Figure 5.14: Lift hysteresis loops for reduced frequency $k = 0.6, 0.9, 1.2$ on a NACA 0012 oscillating in pitch about its midchord.

Fig. 5.14 shows the variation of lift on the airfoil during a cycle of oscillation for the three reduced frequencies. The lift during the pitch-up part of the cycle increases as the reduced frequency increases. This is apparent from the results already presented, namely, the propagation of the separation point is dalayed with increasing reduced frequency and so the airfoil retains more lift.

The lift on the airfoil during the beginning part of the pitch-down phase of its oscillation is higher than that at corresponding nominal angles of incidence during the pitch-up phase of the oscillation. This phenomena becomes more prominent and per-

sists longer (in angular sense) as the reduced frequency increases. The reason for this peculiar effect is associated with the delay in the propagation of the separation point and the associated onset of formation of the primary vortex. For example, at $k = 1.2$ the separation point does not reach its most upstream location until the airfoil pitched *down* 0.6^o from its maximum nominal angle of incidence. And even after the separation reaches the leading edge, all the shed vorticity accumulates helping the airfoil retain most of its maximum lift. The decreasing speed of the primary vortex with increasing reduced frequency also adds to this effect.

It can also be observed that the lift at lower angles of attack also, *i.e.* at $\alpha = 6 - 10^o$, during both the upstroke and the downstroke, is larger for higher k.

This happens during the upstroke because of, as explained before, the delay in the movement of the separation point. Though the accelearion of the airfoil is larger for higher k, apparent mass effects do not contribute to lift, because the airfoil is pitching about its midchord. There are two reasons why the airfoil is able to retain more lift at higher k during the downstroke. The first is that since the airfoil is pitching down at a qicker rate, the primary vortex remains on the airfoil for longer angular interval. The second reason is that the speed of the vortex, as shown in Fig. 5.12 decreases with increasing k. The delayed downstream propagation of the separation point (reattachment point) during the downstoke at higher k, as shown in Fig. 5.11, counters, to some extent, the effect of the two phenomena mentioned above.

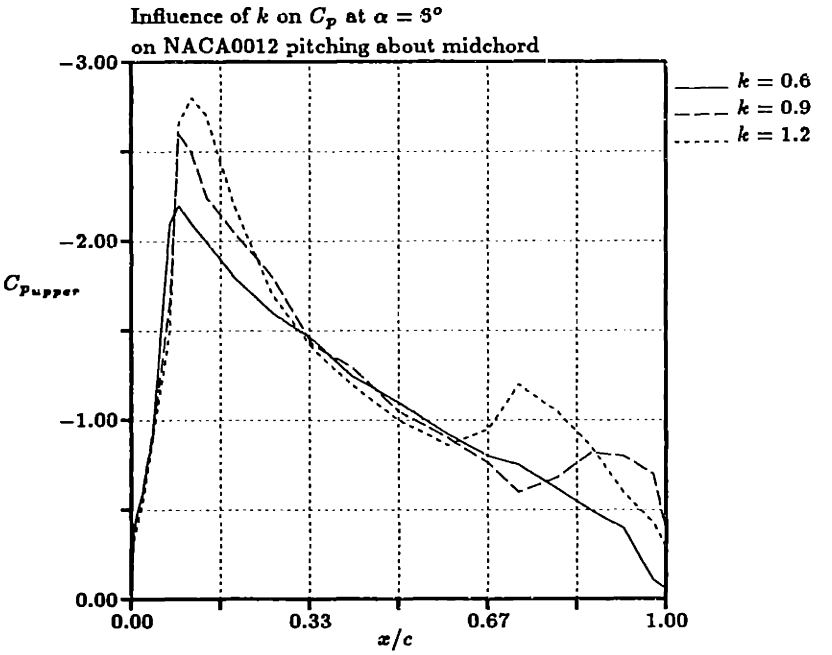

Figure 5.15: Comparison of suction surface pressure distributions at $\alpha = 6^o$ for $k = 0.6, 0.9, 1.2$. Observe the presence of negative pressure peaks caused by a passing primary vortex in the profiles corresponding to $k = 1.2, 0.9$. The pressure distribution on the airfoil at $k = 0.6$ indicates that the vortex has travelled past the trailing edge in this case.

Fig. 5.15 shows influence of a passing primary vortex on the suction surface pressure distribution when the airfoil has just completed the oscillation cycle, *i.e.* $\alpha = 6°$, during which the primary vortex was produded. For $k = 0.6$, the vortex has drifted beyond the trailing edge and causes no discernible perturbation to the pressure profile. For $k = 0.9, 1.2$, however, the primary vortex is still in the neighborhood of the trailing edge, causing negative pressure peaks at $x/c = 0.92, 0.76$, respectively.

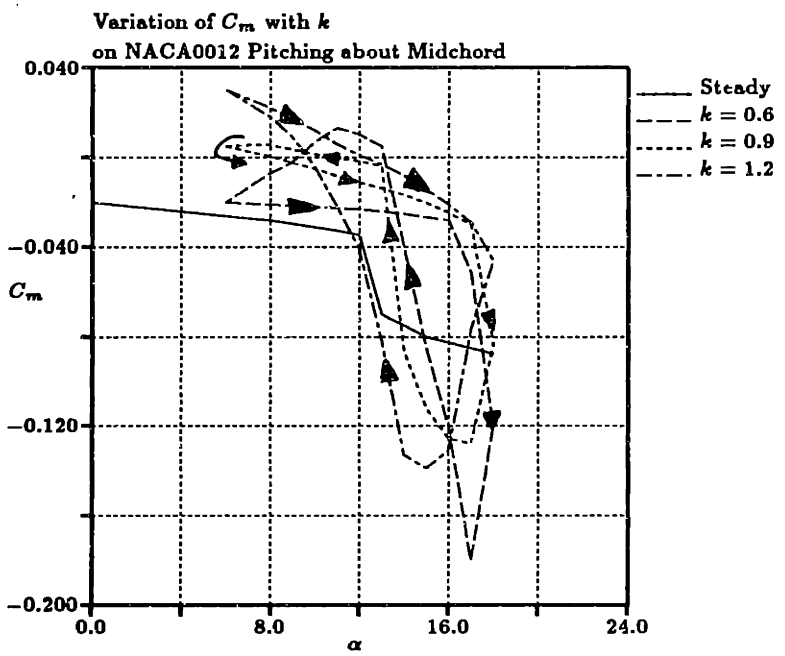

Figure 5.16: Influence of k on the Pitching Moment hysteresis loops for a NACA 0012 pitching about its midchord.

Next let us consider the pitching moment (about quarter chord) variation and the influence of increasing k on it. The variation of the pitching moment over a cycle of oscillation at the three reduced frequencies are plotted in Fig. 5.16.

Observe that the C_m at the beginning of the oscillation cycle, *i.e.* at $\alpha = 6^o$, increases from a negative value to a positive value as the reduced freqency increases from 0.6 to 1.2. There are two factors that cause this effect.

The first is that, as seen in Fig. 5.15, for the higher frequencies, the primary vortex causes a negative pressure peak near the trailing edge. This pressure difference,

though small, can have significant influence on C_m because of its distance from the quarter chord.

The second is the apparent mass effect. At $\alpha = 6^o$, the airfoil experiences its largest angular acceleration. Since the airfoil is pitching up, the apparent mass related moment on the airfoil would be counterclockwise (positive). Also recall that, since $\ddot{\alpha}$ is proportional to ω^2, the apparent mass contribution to C_m would be proportional to k^2. This means that the apparent mass contribution to C_m when $k = 1.2$ is four times that when $k = 0.6$. Theodorsen's [8] linear unsteady airfoil theory gives the apparent mass contribution to C_m at $\alpha = 6^o$ and $k = 1.2$ to be $+0.12$. The corresponding value for $k = 0.6$ is 0.03.

As the airfoil pitches further up, C_m for all the reduced frequencies decreases, due to the increasing concentration of lift in the neighborhood of the leading edge. This trend is more drastic (in angular sense) in the lower frequency cases because of, again, the increasing delay in the upstream propagation of the separation point at higher frequencies.

As the airfoil starts to pitch down from its maximum nominal incidence, the extent of overshoot of the recovering C_m into the clockwise (positive) regime decreases as the reduced frequency increases. The reason for this is that the primary vortex strength (and so the magnitude of the associated negative pressure peak) decreases

with increasing frequency. In addition, the vortex travels with smaller speed at higher frequencies, causing the recovery of C_m to occur less rapidly.

When the airfoil approaches $\alpha = 18^o$, the apparent mass contribution to the total moment is equal in magnitude to its contribution when $\alpha \simeq 6^o$. But as a fraction of the total moment its significance is much smaller because both the size and movement of the primary vortex play a dominant role when $\alpha \simeq 18^o$.

We can now conclude that, while increasing the reduced frequency causes many quantitative changes in the flow features associated with dynamic stall, the main qualitative features that characterize dynamic stall remain intact for the domain of the reduced frequency range considered here. The same conclusion can not, however, be drawn for very high reduced frequencies *i.e.*, $k \geq 2$. We know also that, as explained in chapter 1, for low reduced frequencies above the quasi steady range, *i.e.*, $0.05 \leq k \leq 0.3$ the nature of the hysteresis loops are somewhat different.

It appears from our calculations for $k = 1.2$ (and $k = 1.5, 2$ though not presented here) that, for frequencies around 2, there would be at least one vortex present in the vicinity of the airfoil throughout the oscillation cycle and during some parts of the cycle there will be two. (It can then be easily inferred that at higher frequencies, the number of vortices will grow.) Then the interaction of these two vortices can have significant effects on the forces and moments on the airfoil. As the reduced frequency

increases further, there will be multiple vortices in the vicinity of the airfoil. But our calculations indicate, consistent with common sense, that the strength of these vortices will reach a finite asymptotic limit as the frequency is further increased. So it appears that, as the frequency increases the extent and thus the significance of rolling-up of the shear layer diminishes.

At such high frequencies, the airfoil sheds one vortex at each extreme angular point during its oscillations. For such flows, the above method will be unwieldy and difficult to implement as the separation point movement becomes extremely rapid and the present method can introduce significant errors. A simpler potential flow model that treats the leading and trailing edge of the airfoil as sharp edges shedding vortices at some cleverly designated times would probably work better.

Though the results presented above and the explanations given concerning the effects of pitch rate on dynamic stall are for the pitch axis located at midchord, they are qualitatively valid for any typical pitch axis location downstream of the leading edge but can not be generalized for other locations of the pitch axis. For instance, for the pitch axis located upstream of the leading edge, increasing the reduced frequency will promote rather than delay separation.

The effects of moving the pitch axis location on the flow features associated with dynamic stall will be discussed next.

5.3 Effects of Pitch Axis Location on Dynamic Stall Phenomena

Although the effects of axis location have not been investigated as extensively as those of the reduced frequency, they are very important in locating control surfaces and configuring swept lifting surfaces on missiles and aircrafts. With clear understanding of its effects on dynamic stall, the pitch axis location can be used as a design parameter to either offset or enhance some of the effects of pitch rate on the stability of the vehicle. Understanding pitch axis influence is also important when correlating experimental measurements obtained for a variety of pivot locations.

In addition to the data already presented for the pitching oscillations of NACA OO12 with the pitch axis located at $x_0/c = 0.5$, we will, in this section discuss results for $x_0/c = 0.25, 0.75$. We kept the reduced frequency unchanged at $k = 0.6$.

We will first show what has by now emerged as the fundamental feature of dynamci stall, namely the movement of the separation point. Since we will be comparing the effects of the location of the pitch axis for the same reduced frequency, we can plot the results as functions of time (appropriately nondimesionalized) instead of the angle of incidence of the airfoil.

Fig. 5.17 shows influence of the pitch axis location x_0 on the movement of the

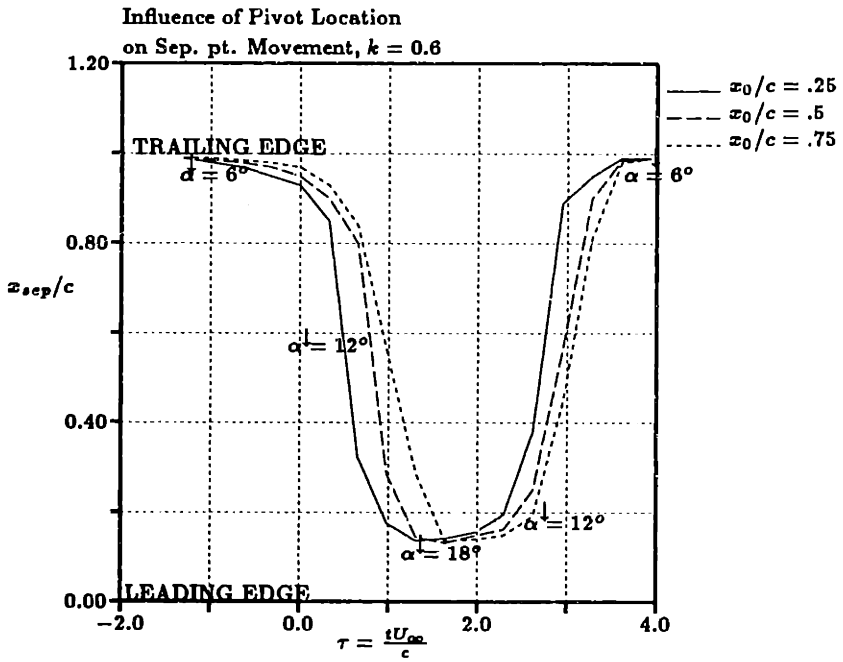

Figure 5.17: Variation in the propagation of separation point for three different pivot locations.

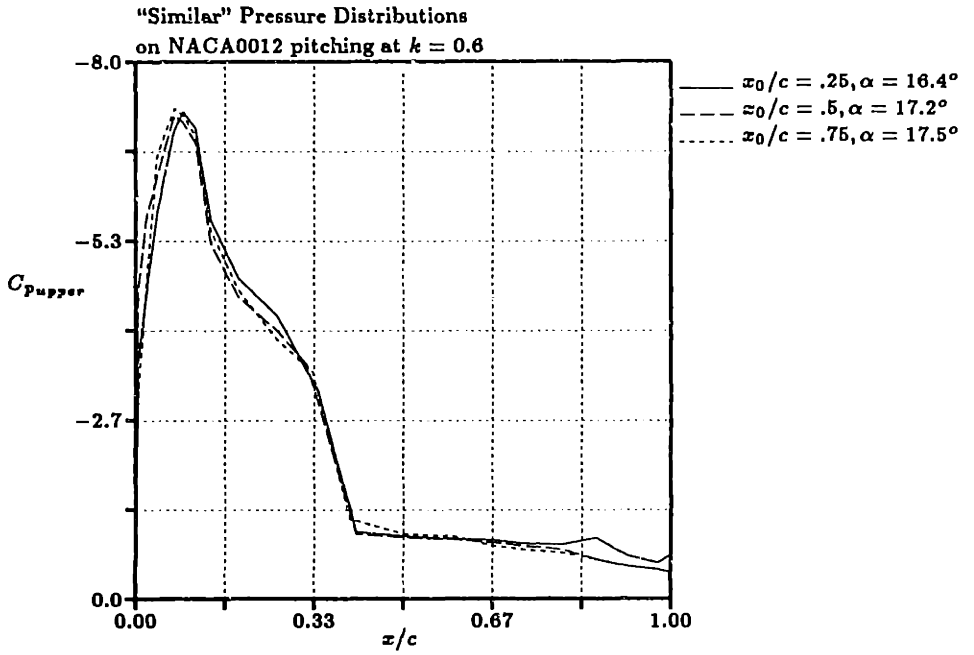

Figure 5.18: C_p distributions on the airfoil suction surface for pitch axis location at $x_0/c = .25, .50, .75$. The time (or angle) at which the C_p is taken on each airfoil is chosen so that the difference in those times is equal to the time or angular delay in dynamic stall events caused by shifting the pitch axis location.

separation point for $k = 0.6$ as function of time. It can be observed from the former figure that shifting the pitch axis from the quarterchord to further aft of the leading edge delayed the separation process but not its propagation characteristics. This observation is supported by the C_p distributions plotted in Fig. 5.18.

Consequently, the time of inception of the primary vortex, as shown in Fig. 5.24 is delayed as the pitch axis is moved further towards the trailing edge, though the

location of the vortex inception is not strongly influenced to the best of our perception.

These observations are in qualitative agreement with those of Helin and Walker [35] who conducted flow visualization experiments on NACA 0015 in dynamic stall due to constant rate pitch-up motion with $k = \frac{\dot{\alpha}c}{2U} = 0.1, 0.2, 0.3; x_0/c = 0.25, 0.50, 0.75$ and $Re = 4.5\times10^4$. The same conclusions were drawn by Visbal and Shang [88] from his numerical studies using a Navier-Stokes solver. They investigated the flow over a NACA 0015 undergoing dynamic stall due to constant rate pitch-up motion at $k = \frac{\dot{\alpha}c}{2U} = 0.1, 0.3; x_0/c = 0.25, 1.0; M_\infty = 0.2$ and $Re = 10^4$. Jumper *et. al.* [37] conducted experiments on a NACA 0012 pitching up constant rates with $k = \frac{\dot{\alpha}c}{2U} = 0.05, 0.1, 0.2; x_0/c = 0.25, 0.50, 0.75$ at $Re = 10^5$. Their results also supprort the conclusions drawn here.

The influence of moving the pitch axis x_0 on the variation of C_L is shown in Fig. 5.19. Observe that as x_0 is moved further towards the trailing edge, C_L at a given α decreases. There are two reasons for it.

The first is that, when the airfoil pitches-up at a rate $\dot{\alpha}$ about a point x_0 away from the leading edge, the leading edge moves relative to the fluid and perpendicular to the airfoil chord, as shown in Fig. 5.20, at a speed $W_{l.e.}$ given by

$$W_{l.e.} = \dot{\alpha}x_0 = \tilde{\alpha}x_0\omega\cos(\omega t) \tag{5.6}$$

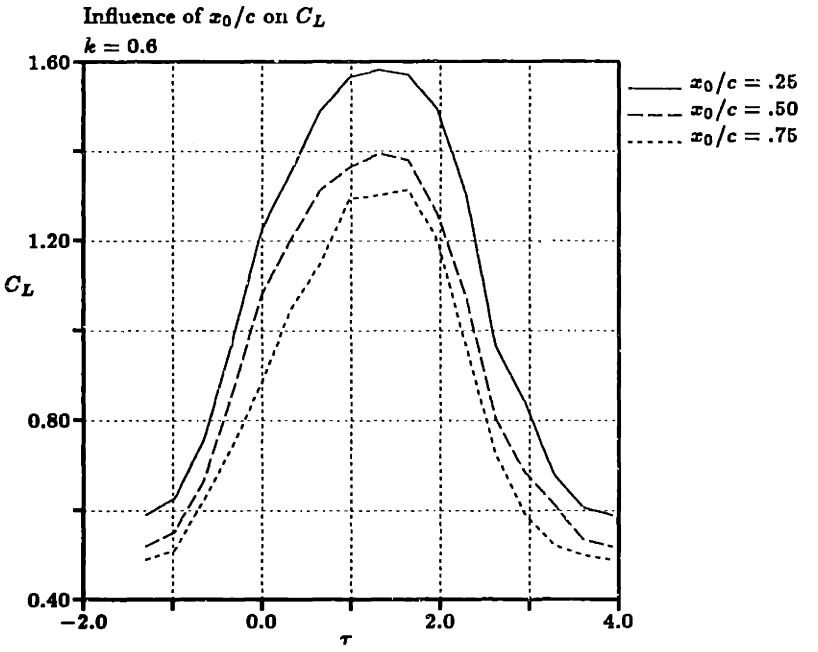

Figure 5.19: Effect of moving the Pitch Axis on the Variation of C_L during a cycle of oscillation for a NACA 0012 pitching at $k = 0.6$

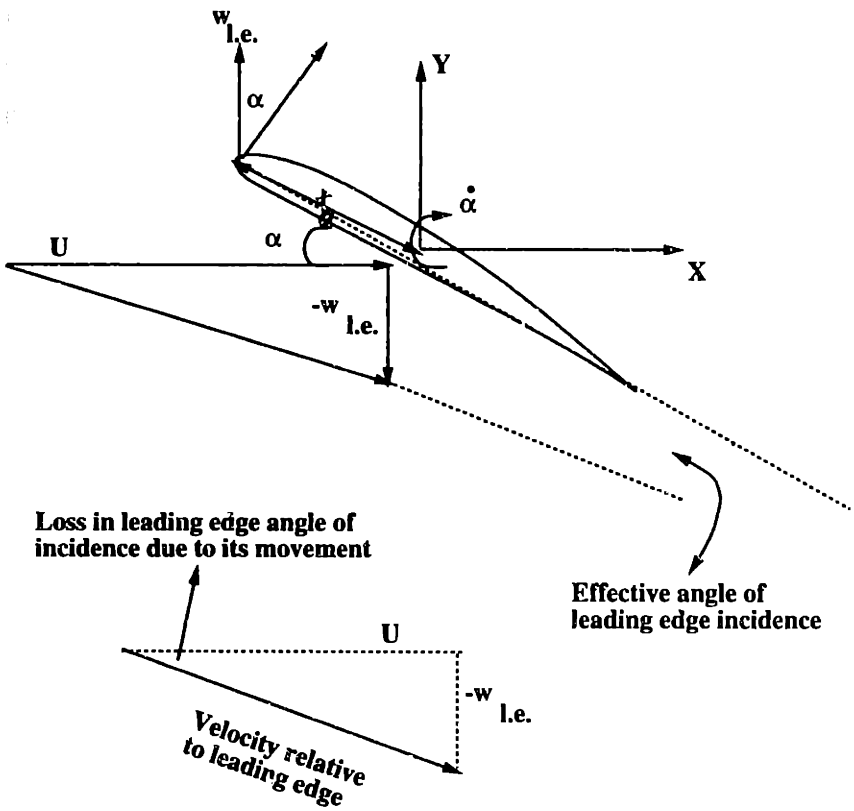

Figure 5.20: Illustration of Effective Angle of Incidence at the leading edge

where we used Eq. 5.1. This speed $W_{l.e.}$ has a component perpendicular to the freestream

$$w_{l.e.} = W_{l.e.} \cos \alpha \tag{5.7}$$

where α is the nominal angle of incidence of the airfoil with respect to the freestream U_∞ as given in Eq. 5.1. Thus the effective angle of incidence at the leading edge has decreased and now it is given by

$$\alpha_{eff} = \alpha - \arctan(\frac{w_{l.e.}}{U}) = \alpha(t) - \arctan\left(2k\tilde{\alpha}\frac{x_0}{c}\cos(\alpha)\cos(2k\tau)\right) \tag{5.8}$$

Thus $\frac{x_0}{c}$ emerges as a new nondimensional parameter characterizing the flow. Figs. 5.21, 5.22 show α_{eff} as a function of ωt and α, respectively for the three pivot positions that are of interest to us. It can easily be seen that α_{eff} differs significantly from α, by up to 20% at $\alpha = 12^o$ when the velocity of the leading edge with respect to the pivot is a maximum. It can also be observed that the difference increases with the distance of the pivot position from leading edge.

One can see from the above equation that when $cos(2k\tau)$ is not changing rapidly with τ, *i.e.* when $\tau \simeq 0 \Rightarrow \alpha \simeq 12^o$, $k\frac{x_0}{c}$ can be regarded as one parameter, *i.e.* increasing k has the same effect on $(\alpha - \alpha_{eff})$ as increasing x_0/c by the same amount, lending support to the proposition that there are certain similarities between the effects of increasing k and increasing x_0/c.

It is now clear that when $\frac{x_0}{c} \geq 0$, as this parameter increases, the effective angle of

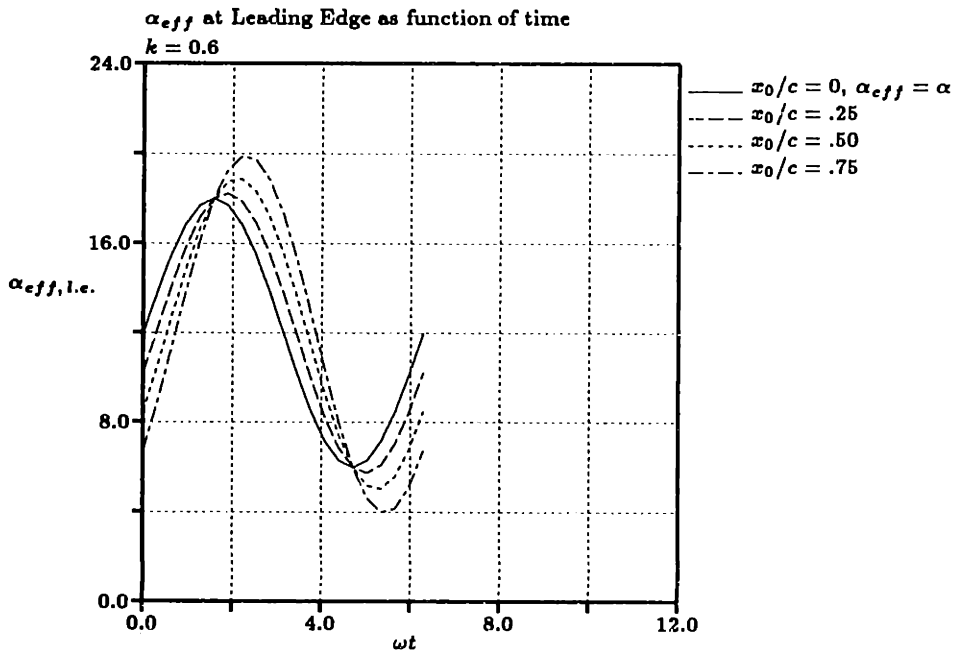

Figure 5.21: Effective angle of leading edge incidence as a function of time for three pivot positions at $k = 0.6$.

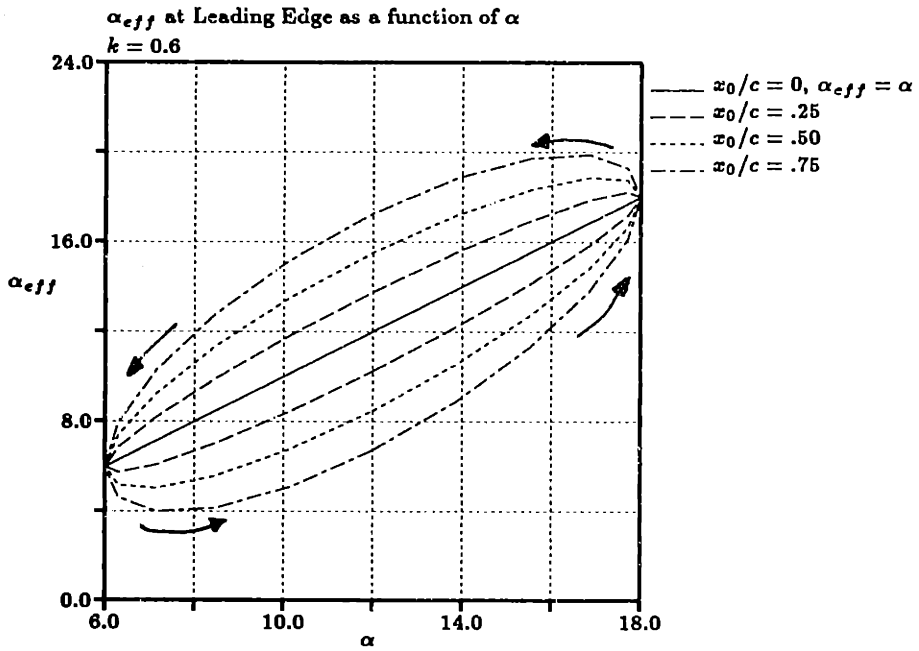

Figure 5.22: Effective angle of leading edge incidence as a function of nominal angle of incidence for three pivot positions at $k = 0.6$.

incidence on the airfoil decreases and so C_L also decreases. When the airfoil is at small angles of incidence this effect is largely potential and linear, *i.e.* as $\frac{x_0}{c}$ increases, it appears as if the leading edge acquired a negative camber.

When the separation point remains fairly close to the trailing edge, we can draw important information from Theodorsen's [8] linear unsteady airfoil theory. Nonlinear theories, such as the one forwarded by McCune [57] can be also be used for this purpose. In Fig. 5.23 we have plotted results from our nonlinear potential analysis for the cases presently being discussed. (Theodorsen's linear theory gives essentially the same results, except for the higher end of the angle of incidence domain, where this comparison is not applicable.) The "camber" effect of moving the pitch axis can be clearly seen in this figure. By comparing this figure to Fig. 5.19, one can observe that the potential results, again, are in fair agreement with the viscous (from present method) results for up to $\alpha \simeq 10 - 14^o$. It can also be seen that this domain of agreement grows with increasing x_0/c.

As the angle of incidence becomes larger, *i.e.* $\alpha \geq 14^o$, the separation point is no longer limited to the trailing edge area and so the difference in the propagation speeds of the separation point will play an increasingly larger role in determining the difference in the lift coefficients of airfoils pitching about different pivots.

The second reason the location of the pitch axis causes a time (and thus angular, since

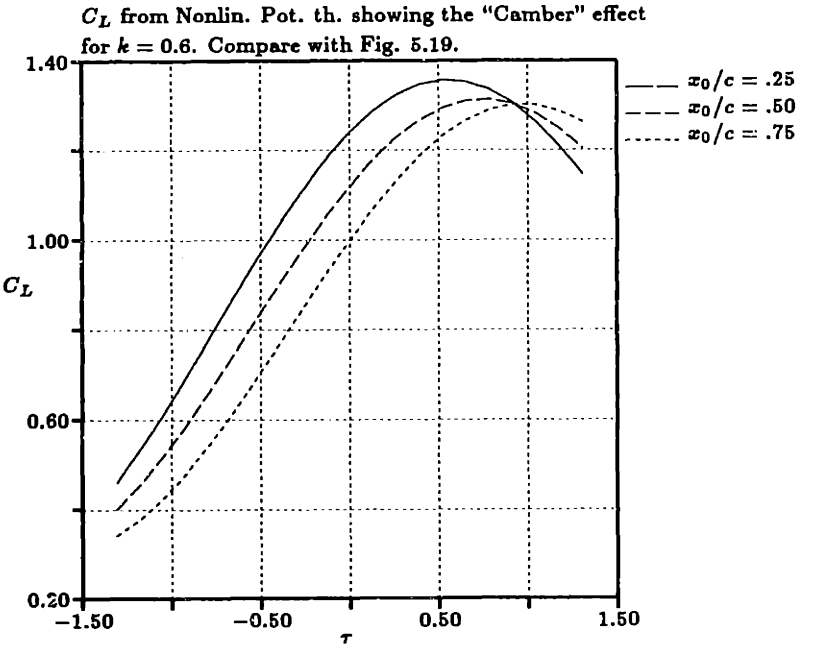

Figure 5.23: C_L from anlytical nonlinear potential theory for three pivot positions at $k = 0.6$. Observe the effect of moving the pivot towards the trailing edge "similar" to introducing negative camber.

k is constant in this discussion) shift in C_L and other dynamic stall events is the rate at which counterclockwise (positive) vorticity is shed from the lower surface boundary layer into the wake. For a fixed reduced frequency, moving the axis upstream of the trailing edge causes it to move at higher speed. This results in an increment in the positive vorticity flux [76], as explained also in chap. 3. This in turn causes the rate of change of bound circulation to increase, according to Kelvin's circulation therorem in Eq. 2.6. Therefore, as the axis is moved upstream from the trailing ege, the accumulation of circulation on the airfoil occurs at a quicker rate, or equivalently, the airfoil attains a higher effective angle of incidence.

Another way of looking at the same effect is to consider the "effective angle of incidence" attained at the leading edge. As the pitch axis is moved downstream, the loss in nominal angle of incidence at the leading edge increases, as given by equation 5.8. Therefore, the magnitude of C_p attained at the leading edge decreases, contributing to an overall reduction in lift at any given nominal angle of incidence, when the airfoil is pitching up.

Although events up to and including the inception of the primary vortex are delayed as the pitch axis is moved towards the trailing edge, the duration of growth and movement of the vortices are not significantly affected, except for the time delay that was already introduced during earlier events. The strength of the vortex increases with increasing pitch axis distance from the trailing edge. The reason for this is

similar to the one presented in the case for increasing reduced frequency at constant pivot location. Namely, as the pivot location moves closer to the leading edge, higher peak velocities are attained there, there by increasing the strength of the shear layer which feeds the primary vortex. The average speeds and the strengths of the primary vortices for all the three pivot locations are shown in Figs. 5.24 and 5.25, respectively. The numerical values are summarized in the table below.

Pivot location $(\frac{x_0}{c})$	Inception time, (τ)	angle, (α)	location. $(\frac{x}{c})$	Ave. speed $(\frac{U_{vortex}}{U})$	Strength $(\frac{\Gamma_{p.v.}}{Uc})$
.25	.7342	$16.3^{o,+}$	.188	.398	.625
.50	.8211	$17^{o,+}$	.192	.421	.592
.75	.8705	$17.2^{o,+}$	.194	.433	.576

It is interesting to recall from the first and second sections of this chapter that a delay in the inception of the dynamic stall vortex allows the airfoil to reach a higher C_L. However, shifting the pitch axis towards the trailing edge also delayed the initiation of the dynamic stall vortex accompanied though, with a reduction in lift. Therefore, one can not assume that further delays in the leading edge vortex inception, *i.e.* the inception of dynamic stall, will always result in higher airfoil lift. However, it appears that moving the pitch axis toward the trailing edge emulates some of the effects of an

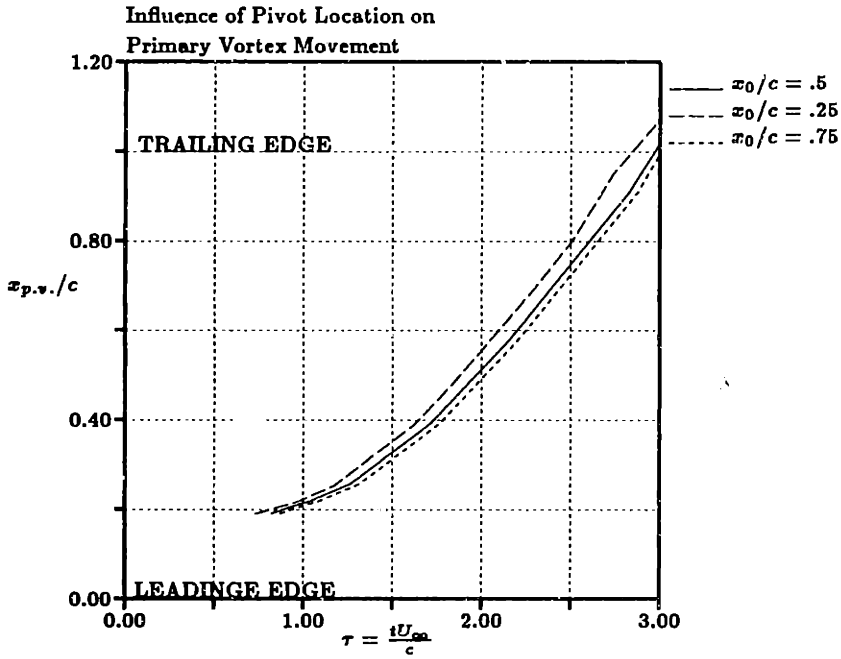

Figure 5.24: Influence of the pivot location on the evolution of the primary vortex for $k = 0.6$.

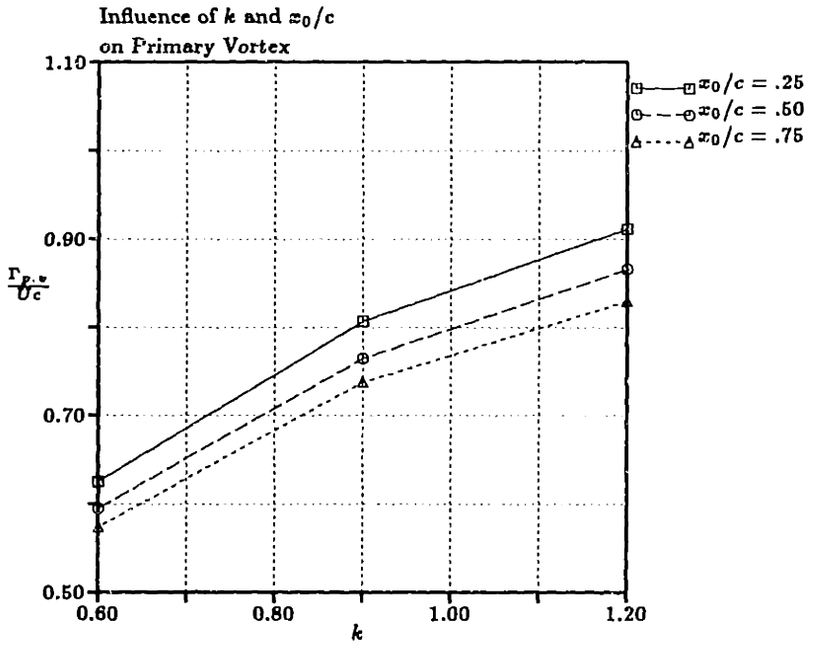

Figure 5.25: Influence of the pivot location on the strength of the primary vortex.

increased reduced frequency. This observation has important implications in aircraft design.

Chapter 6

Dynamic Stall Due to Heaving Oscillations

Helicopter blades (and even high aspect ratio wings) are subjected to both twisting and bending oscillations due to the unsteady loads acting on them. If the instantaneous angle of incidence on a blade section undergoing twisting oscillations exceeds the static stall angle, dynamic stall is likey to occur on the blade, as explained in the previous chapter. In addition, or even in the absence of twisting oscillations, if the blade undergoes bending oscillations, its instantaneous angle of incidence can change significantly from its nominal (or geometric) angle of incidence, as will be explained in the next section. Under such circumstances the incidence angle on the blade can

exceed its static stall angle and cause dynamic stall. It is therefore of significance to understand, particularly for helicopter aerodynamicists, heave induced dynamic stall and its relation to pitch induced dynamic stall.

In this chapter we have presented the results of our calcualtions of the flow on a NACA 0012 heaving in an otherwise spatially and temporally uniform stream. The parameters of the flow are picked such that the heaving oscillations are rapid and large enough to cause dynamic stalling of the airfoil. Next, we have related the flow characteristics present in pitch induced dynamic stall to those present in dynamic stall caused by heaving oscillations. We have then considered the effects of changing an appropriately defined reduced frequency on the dynamic stall characteristics. But first we will define an "equivalent angle of incidence" for a heaving airfoil, based on which a correspondence is drawn between a pitching airfoil and a heaving airfoil.

6.1 Equivalent Angle of Incidence

Consider an airoil at a constant nominal angle of incidence $\bar{\alpha}$ undergoing a sinusoidal heaving displacement $h(t)$ perpendicular to a uniform stream U_∞, as shown in Fig. 6.1. Let this displacement $h(t)$ be given by

$$h(t) = h_0 \cos(\omega t) \tag{6.1}$$

where h_0 is the magnitude of oscillation and ω is, as before, the angular rate of oscillation. So the velocity of the airfoil normal to the freestream is given by

$$\dot{h} = -h_0\omega \sin(\omega t) \tag{6.2}$$

Therefore, the inclination of the flow relative to the airfoil is no longer $\bar{\alpha}$ (with respect to the airfoil chord), but will be a function of the time dependent $\dot{h}$, as shown in Fig. 6.1. The instantaneous angle of incidence on the airfoil or the "equivalent angle" is given by,

$$\alpha_{eq} = \bar{\alpha} - \arctan(\frac{\dot{h}}{U_\infty}) \tag{6.3}$$

For small values of $\frac{\dot{h}}{U_\infty}$, we can write the above equation as

$$\alpha_{eq} = \bar{\alpha} - \frac{\dot{h}}{U_\infty} = \bar{\alpha} + \frac{h_0\omega}{U_\infty} \sin(\omega t) \tag{6.4}$$

Denoting $\frac{h_0\omega}{U_\infty}$ by $\tilde{\alpha}$, we can write the above equation in the familiar form as

$$\alpha = \bar{\alpha} + \tilde{\alpha} \sin(\omega t) \tag{6.5}$$

The reduced frequency of the motion is defined again as

$$k = \frac{\omega c}{2U} \tag{6.6}$$

In the rest of the discussion we will drop the subscripts eq in the equivalent angle and ∞ in the freestream velocity except when noted.

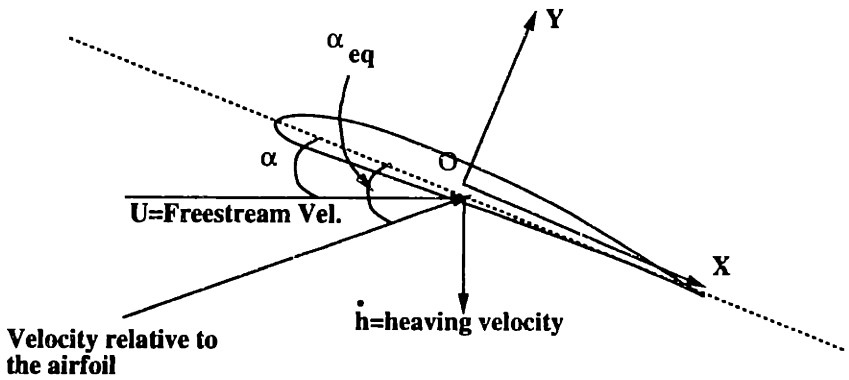

Figure 6.1: Instantaneous Equivalent angle of incidence on an airfoil heaving at constant nominal incidence in an otherwise uniform stream.

6.2 Potential Flow Considerations

Before describing the dynamic stall characteristics of the airfoil in heave, we will investigate some aspects of the potential flows on heaving and pitching airfoils that may help us gain insight into the similarities and dissimilarities in the dynamic stall characteristics of the above mentioned modes of motion.

As mentioned in the last chapter, the effective angle of incidence at the leading edge on an airfoil oscillating in pitch is different from the nominal angle of incidence on the airfoil. It was also shown that this difference contributes to a dealy in the dynamic stall of the airfoil.

Consider now two scenarios, one in which an airfoil is pitching sinusoidally about its quarter chord such that its nominal angle of incidence varies between 6^o and 18^o and the second in which the airfoil is heaving such that its equivalent incidence changes between the same limits.

The α_{eff} at a distance x away from the pivot on the pitching airfoil, given by Eq. 5.8 in the previous chapter, is

$$\alpha_{eff} = \alpha - \arctan(\frac{w(x)}{U}) = \alpha(t) - \arctan\left(2k\tilde{\alpha}\frac{x}{c}\cos(\alpha)\cos(2k\tau)\right) \qquad (6.7)$$

where

$$w(x)\cos\alpha = \dot{\alpha}x\cos\alpha \qquad (6.8)$$

is the normal component of the velocity at the point x due to the pitching motion of the airfoil, *i.e.* it is the "downwash" at x. Therefore on a pitching airfoil the downwash at any angle of incidence has a linear distribution along the chord of the airfoil. On the other hand, the downwash on a heaving airfoil is constant at $\dot{h}(t)$ throughout the chord of the airfoil.

Thus the downwash on a pitching airfoil is similar to what would be present on a steady parabolic camberline, whereas the downwash on a heaving airfoil would be similar to a steady flat plate at an angle of incidence. These situations are illustrated in Fig. 6.2.

The lift on pitching and heaving airfoils can be found from Theodorsen's linear theory [8] as well as many nonlinear methods [57, 75], including the present method. In the linear limit, the sectional lift l_{pitch} on an airfoil pitching sinusoidally between 6^o and 18^o about a point at a distance x_0 away from its leading ege is given by

$$l_{pitch}(x_0) = \pi\rho U c C(k)\left[U\alpha + \left(\frac{3}{4} - \frac{x_0}{c}\right)c\dot{\alpha}\right] + \frac{\pi\rho c^2}{4}\left[U\dot{\alpha} + \left(\frac{1}{2} - \frac{x_0}{c}\right)c\ddot{\alpha}\right] \qquad (6.9)$$

where $C(k)$ is the real part of the Theodorsen's function at the reduced frequency k and

$$\alpha = \bar{\alpha} + \tilde{\alpha}\sin(\omega t)$$

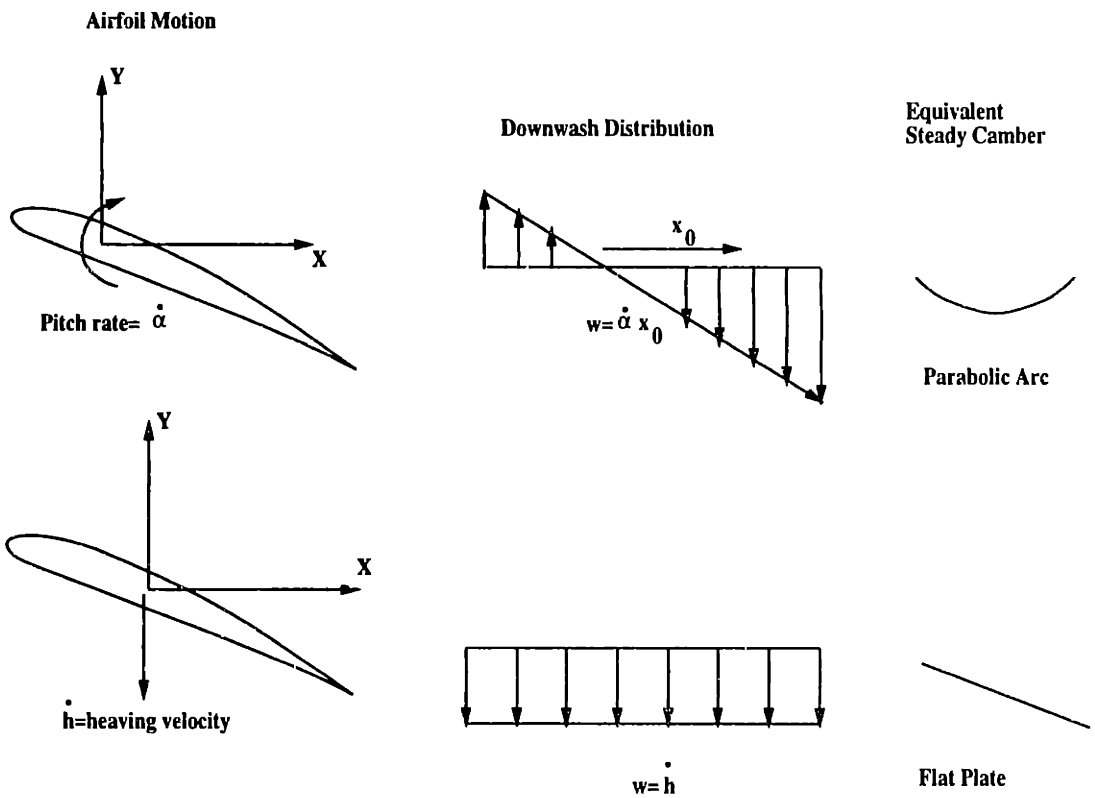

Figure 6.2: Comparison of some aspects of potential flows over pitching and plunging airfoils.

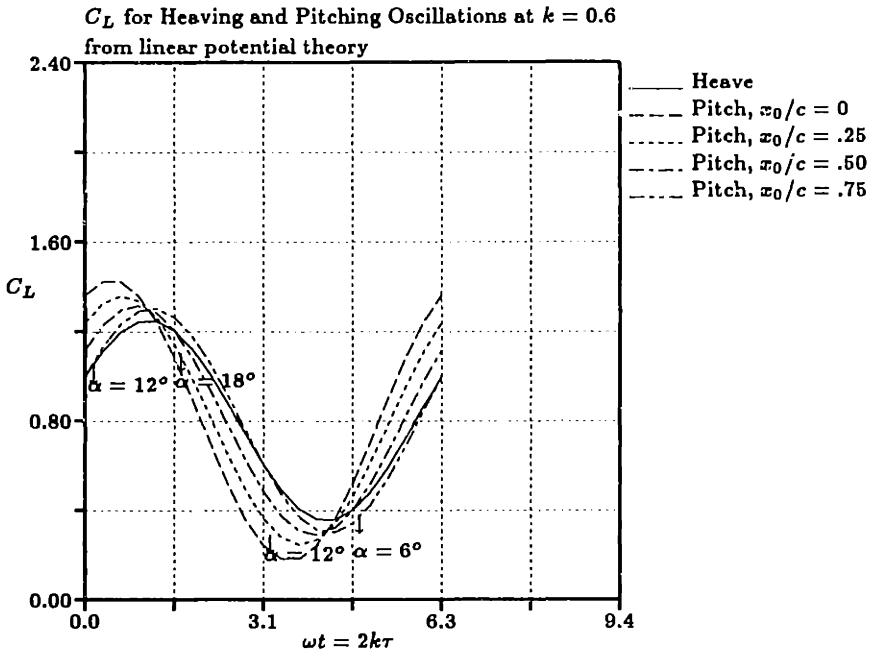

Figure 6.3: C_L from potential theory on heaving and pitching airfoils.

Similarly the lift on a thin airfoil heaving at the rate $\dot{h}$ is given, in the linear limit by

$$l_{heave} = \pi\rho U c C(k)(U\bar{\alpha} - \dot{h}) - \frac{\pi\rho c^2}{4}\ddot{h} \tag{6.10}$$

where we used $\bar{\alpha}$ to denote the nominal angle of incidence of the heaving airfoil.

Using the above equations, results for pitching oscillations about varoius pivots and heaving oscillations are plotted in Fig. 6.3 for $k = 0.6$.

The differences in the results between the C_L for various pivot positions are discussed in the previous chapter. It can be observed that the phase of the lift in the heaving case lags well behind that in the pitching case with pivot at quarter chord. It can

also be observed that the magnitude of $C_{L_{max}}$ for the heaving airfoil is much lower than that in the quarterchord pivot-case. The reason is that, as explained also in the previous chapter, for the pitching cases, during the counterclockwise stroke, α_{eff} near the leading edge is higher as the pivot moves closer to the leading edge. The apparent mass contribution to the lift during the counterclockwise stroke also increases as the pivot moves closer to the leading edge. For the heaving motion the effective angle is equal to the nominal pitching angle.

Therefore we expect the flow behavior in the heaving case to follow closely that of the pitching airfoil with a "rearward" pivot during the early part of the oscillation cycle, *i.e.* when $\alpha : 6^o \rightarrow 12^o$. With reference to the results presented in the previous chapter, this means that, the slope of $C_L - \alpha$ curve during this early part of the cycle will be less for a heaving airfoil than for an airfoil pitching about a "frontward" pivot. Consequently, we expect the dynamic stall events on a heaving airfoil to occur "late" compared to those on a pitching airfoil with pivot close to the leading edge. In addition, we expect the primary vortex strength and $C_{L_{max}}$ reached during the heaving oscillation to be lower than those during a pitching oscillation with pivot around the leading edge. For an explanation of the "dynamic stall delay" in this context, please see the previous chapter.

6.3 Dynamic Stall Characteristics of a Heaving Airfoil

There is a limited amount of experimental literature available on this subject. We know of no theoretical attempts at calculating the dynamic stall characteristics of a heaving airfoil. Liiva, et. al. [49] tested dynamic stall characteristics of airfoils in pitch and heave. These experiments were conducted at reduced frequencies below 0.3. Fukushima and Dadone [24] compared dynamic stall characteristics of airfoils oscillating in pitch and heave at approximately the same reduced frequency. The flow was turbulent and the reduced frequency was below 0.15 in their experiments. Rainey [66] conducted experiments on airfoils oscillating in pitch and finite span wings oscillating in bending (heaving). Their presented results are very limited and no generalized conclusions were reported. Carta [14] conducted experiments on airfoils pitching and heaving in order to compare their dynamic stall characteristics. The Reynolds number in his experiments was close to transition and he used reduced frequencies up to 0.25. We will compare our results and conclusions to those from the experiments reported above, though only qualitative comparisons would make sense beacuse of the difference in flow and geometry parameters. Our results and conclusions, as reported below, agree qualitatively with those forwarded in [14, 24, 49].

We have investigated the dynamic stalling of a heaving NACA 0012 for the following

flow and geometry parameters:

$$\bar{\alpha} = 12^o$$

$$\tilde{\alpha} = 6^o$$

$$Re = 10^5$$

$$k = 0.6 \tag{6.11}$$

The above choice of parameters, same as that in section 1 of the last chapter, will allow us to carry out a comparitive analysis of dynamic stall due to heave and pitch. Note that here, *i.e.* in the heaving problem, α_{eq} is chosen to be equal to the nominal incidence in the pitching problem.

We have plotted in Fig. 6.4 the movement of the separation point for the heaving case. Also included in the figure is the behavior of the separation point for a pitching case with pivot at midchord. It can be observed that no significant difference exists between the movement of the separation points during the early part of the oscillation cycle. As α_{eq} approaches 10^O, the rate of propagation of separation on the heaving airfoil becomes greater. The stalling process, *i.e.* the sudden jump of the separation point from near trailing edge to near leading edge is delayed and happens less abruptly on the heaving airfoil. The last observation, namely that the stalling process occurs later and less abruptly on a heaving airfoil, is in qualitative agreement with experimental evidence reported in [24, 14]. During the second half of the cycle, *i.e.* when the α is decreasing, the separation point on the heaving airfoil retreats at

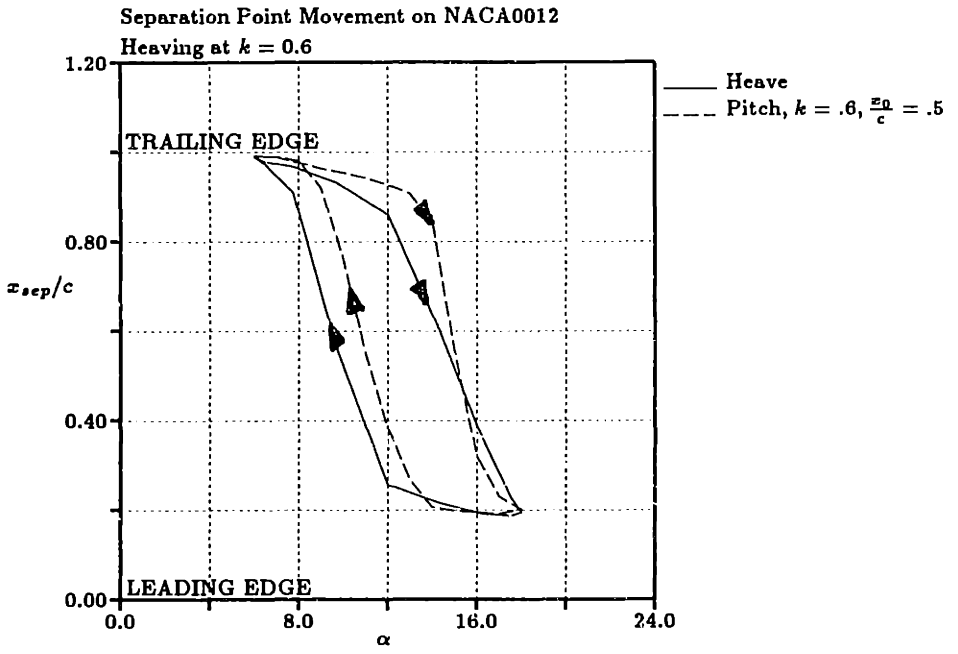

Figure 6.4: Evolution of the suction surface separation point on a heaving airfoil.

a slower rate than its counterpart on the pitching airfoil.

Fig. 6.5 shows that during the early part of the cycle, when the α is between 6^o and 12^o, the $C_L - \alpha$ slope of the heaving cycle is lower than that for the pitching case. Also apparent from the figure is that $C_{L_{max}}$ in the heaving case is lower than that in the pitching case. Both of these results are in agreement with our predictions based on potential flow analysis.

There are two reasons for such behavior. The first is that the peak velocities and peak negative pressures attained at the leading edge are more moderate in the heaving case. The second is linked to the rate of propagation of the separation point,

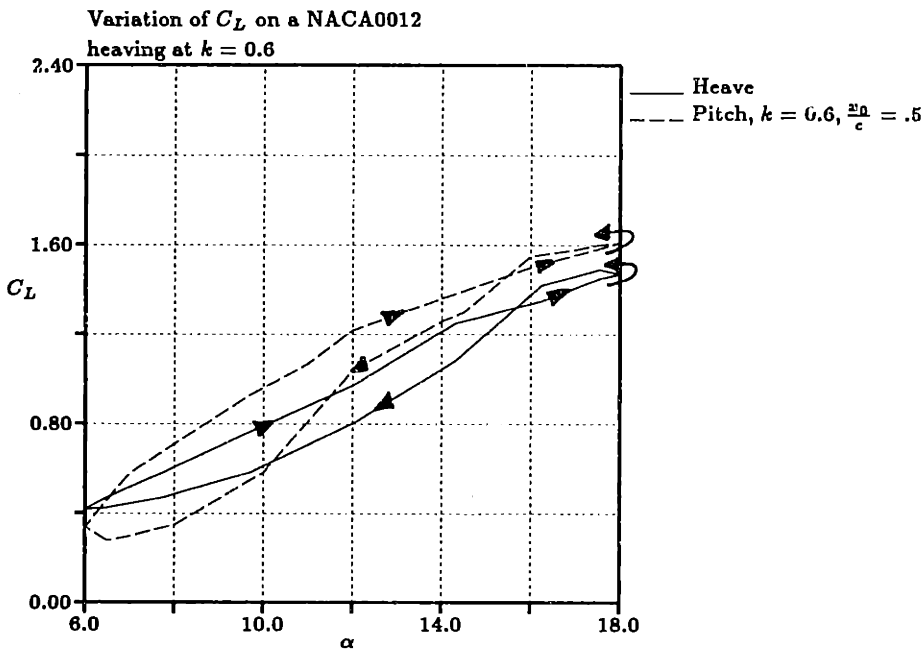

Figure 6.5: Variation of C_L on a heaving NACA 0012 during a cycle of heaving oscillation at $k = 0.6$.

as explained above. Fukushima's experiments [24] have consistently reported lower $C_{L_{max}}$ in heaving than in pitching at the same reduced frequency and between the same angular limits. But results from experiments by Carta [14] show no such pattern. The reason for lack of a consistent pattern in the results of the latter author could be due to the fact that the Reynolds number in his experimemts was very close to the transition number and it varied from case to case between 10^5 and 10^6. Consequently, the occurence and location of flow transition might have changed from case to case affecting the separation location and the pressure distribution. No discussion in this regard was presented in the cited publication.

These results (our results presented above) also indicate that the moment stall will be more moderate, *i.e.* the sudden drop in C_m at the stall angle will not be as precipitious for the heaving case as it was for the pitching case. The behavior of the moment coefficient is shown in Fig. 6.6.

The strength of the primary vortex was calculated to be $\Gamma_{p.v.}/Uc = 0.513$, which is less than that in the pitching case. This is at least partially due to the fact that peak velocities reached at the leading edge are more moderate and the final stages of stalling are less abrupt on the heaving airfoil than on the pitching one, as shown and explained above. The average streamwise speed of the primary vortex is found to be $0.437U_\infty$. This value is not significantly different from those for pitching cases at $k = 0.6$.

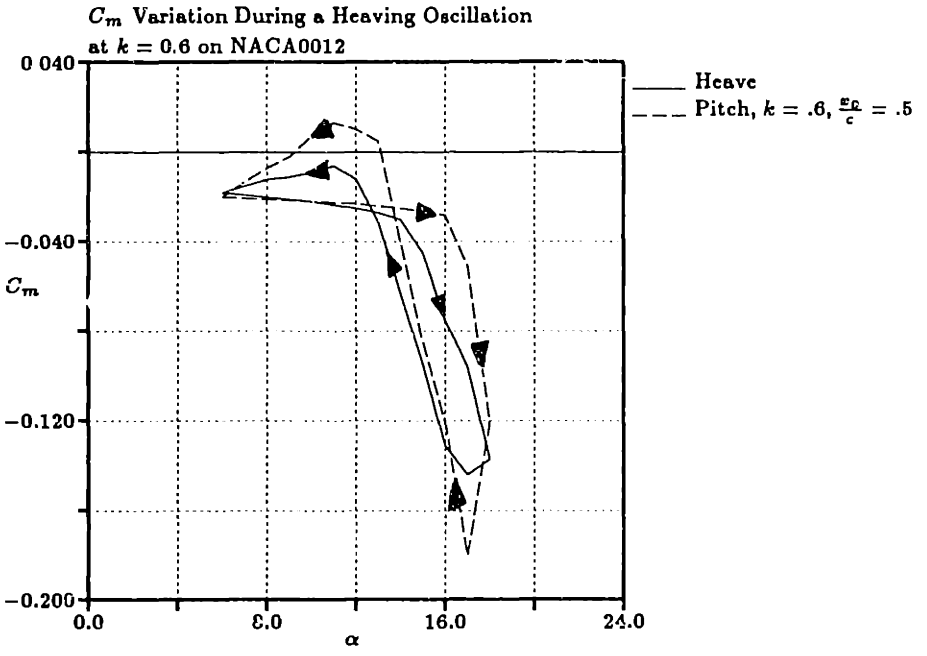

Figure 6.6: Variation of C_m on a heaving NACA 0012 during a cycle of heaving oscillation at $k = 0.6$.

6.4 Effects of Increasing Reduced Frequecy

In addition to the $k = 0.6$ case presented above, we have investigated the flow over a NACA 0012 heaving at $k = 0.9$. The effects of increasing the reduced frequency on the dynamic stall characteristics on a heaving airfoil are largely similar to those on a pitching airfoil. The movement of the separation point towards the leading edge is delayed (in angular sense), the peak velocities and lift coefficients achieved near leading edge have increased, inception of the primary vortex is delayed (angular sense) and the strength of the primary vortex has increased with increasing reduced frequency. These results are shown in Figs. 6.7, 6.8 and 6.9. The physics behind these changes is same as that presented in section 2 of the last chapter. The same effects of increasing the reduced frequency on dynamic stall characteristics were reported in the experiments of [14, 24].

All the important results presented so far and conclusions drawn from these results are summarized in the following chapter.

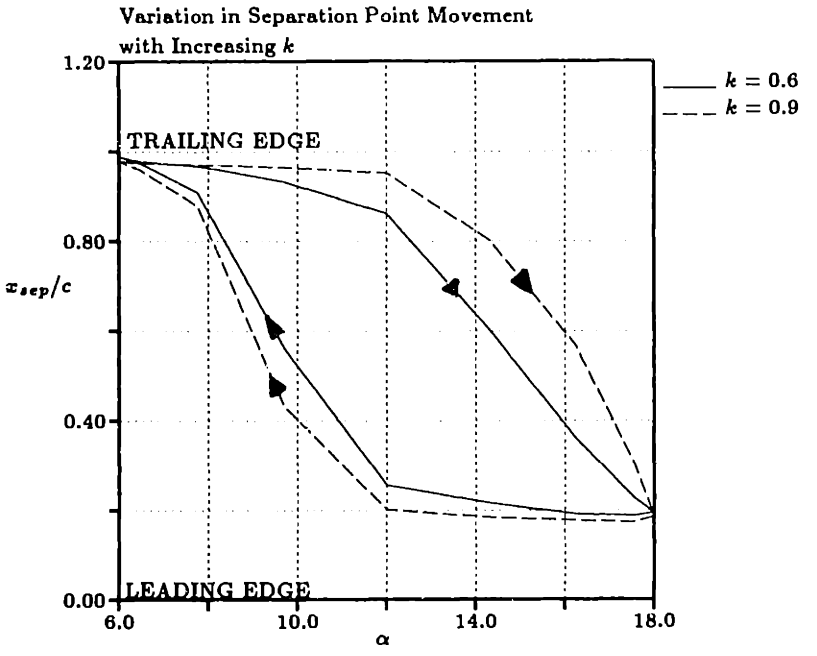

Figure 6.7: Effect of Increasing k on the movement of suction surface separation point on a heaving NACA 0012.

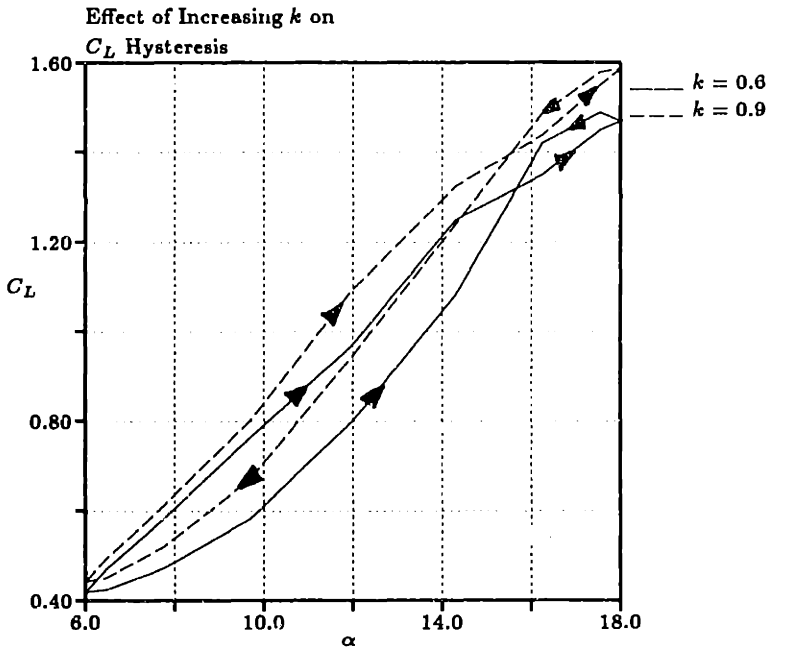

Figure 6.8: Effect of Increasing k on C_L on a NACA 0012 during a cycle of heaving oscillation.

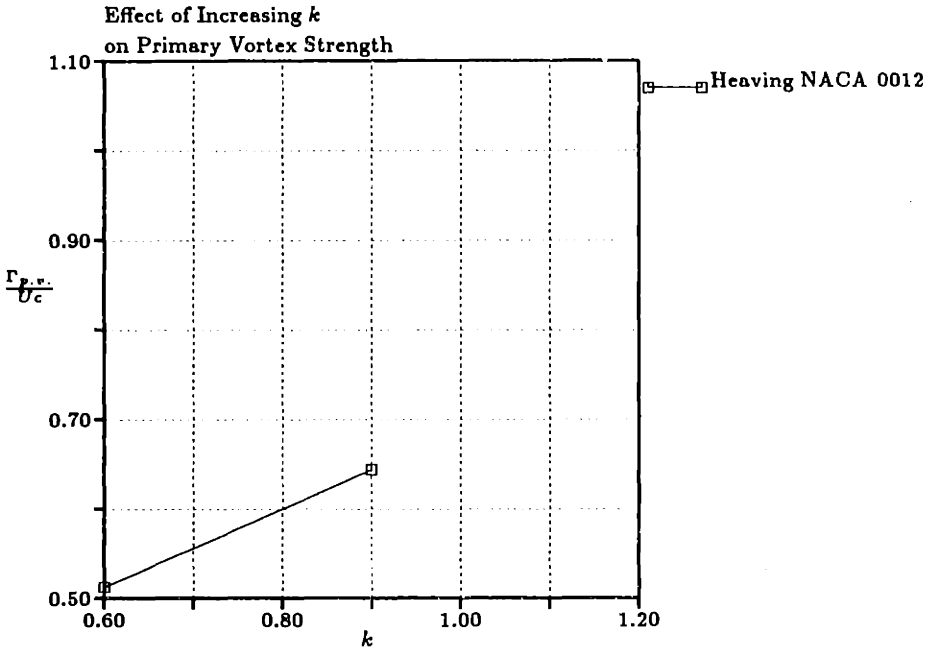

Figure 6.9: Effect of Increasing k on the strength of the primary vortex on a NACA 0012 oscillating in heave.

Chapter 7

Conclusions and Recommendations

7.1 Conclusions

We have calculated the laminar dynamic stall characteristics of a NACA 0012 airfoil using, for the first time, a simple analytic method that clearly explains the various physical processes that together constitute the dynamics stall process. We have investigated the dynamic stall phenomena in a useful high-reduced frequency domain that has, in the past, received comparitively little attention.

We have calculated the effects of increasing the reduced frequency and moving the pivot on the dynamic stall of a pitching airfoil. The primary effect of increasing the reduced frequency was that the stalling processes occured later (in angular sense) but more abruptly. They were accompanied by larger $C_{L_{max}}$, $|C_{m_{max}}|$ and a stronger leading edge vortex ($\Gamma_{p.v.}$). While one of the effects of moving the pitch-axis towards the trailing edge was a delay in the stalling events, however, the $C_{L_{max}}$, $|C_{m_{max}}|$ and $\Gamma_{p.v.}$ attained were smaller. We have also shown that linear potential theory can be used to qualitatively explain/predict these trends.

We have investigated dynamic stall on a NACA 0012 airfoil due to heaving oscillations for a range of reduced frequencies. The dynamic stall characteristics of the heaving airfoil resembled those of an airfoil pitching at the same nominal frequency about a rearward pivot. The effects of increasing the frequency on the stalling process of a heaving airfoil were similar to those on a pitching one.

7.1.1 Calculation Method

The dynamic stall process on a two dimensional airfoil (NACA 0012) oscillating in pitch and heave at various reduced frequencies in laminar incompressible flow was investigated.

The external potential flow was calculated assuming incompressible and inviscid

($Re \rightarrow \infty$) flow around the body. A modern variant of Theodorsen's [84] transformation was used to transform the airfoil to a unit circle. Unsteady Bernoulli equation and a suitably chosen body frame of reference were used for calculating external velocities and pressures on the body.

The unsteady flow in the vicinity of the body was analyzed by using an asymptotic method developed by [50, 29, 30]. This method is applicable in the asymptotic limit when a parameter proportional to the square of the reduced frequency is "large". Using this asymptotic expansion the boundary layer flow is separated into "Prandtl flow" and "Stokes flow" coupled through the wall boundary conditions. The expansion results in a set of simple equations which were solved to obtain the velocities in the boundary layer. An unsteady separation criterion, consistent with the Moore-Rott-Sears [74] separation criterion, developed by [30] as an extension of Stratford's [79] separation criterion for steady flows, was used to calculate the separation points of the boundary layers.

The separated boundary layers, *i.e.* free shear layers, were represented by discrete vortices. Each vortex is convected by the velocity imposed at its location by the airfoil and all other vortices so that all free vortices remain force-free throughout the calculation. Thus the entire flow field is updated at each time step using the Biot-Savart law. The calculation was repeated until convergence was reached.

The validity and accuracy of the method was established by comparing our results to those from many existing experiments and calculations.

7.1.2 Results

Dynamic Stall Due to Pitching

We first investigated the flow evolution during a pitching oscillation of a NACA 0012. The airfoil oscillates sinusoidally between $\alpha = 6^o$ and 18^o about its midchord at reduced frequency $k = 0.6$. Our calculations indicated that:

1. The pressure surface separation point does not move (to any significant distance) from the trailing edge throughout the cycle of oscillation.

2. The suction side separation point, on the other hand moves all the way to within 19% of the chord from the leading edge.

3. The lift on the airfoil continuously increases well beyond its static stall value, as the angle of incidence on the airfoil is increased. The $C_{L_{max}}$ reached was 1.61 at $\alpha = 18^o$.

4. At $\alpha = 17^o$ ($\tau = .821$) when the airfoil is pitching up, vorticity being shed from the suction surface shear layer starts to accumulate forming the primary or dynamic

stall vortex. This process of vorticity accumulation in the vicinity of the leading edge area continues even after the airfoil starts to pitch down.

5. The presence of the primary vortex above the airfoil helps the airfoil maintain high C_L even when the airfoil is pitching down. The vortex starts to move downstream causing a traveling negative pressure peak on the suction surface.

6. The strength of the primary vortex was calculated to be $\frac{\Gamma_{p.v}}{Uc} = 0.6$ and its average streamwise speed $0.42U$.

7. As the separation point moves upstream of the trailing edge, the magnitude of C_m grows, although slowly. When the separation point jumps abruptly to the leading edge area, the value of C_m becomes a large negative number (nose-up moment). The magnitude of C_m continues to grow for a short while even after the airfoil starts to pitch down.

8. As the airfoil continues its clockwise pitch, C_m recovers and becomes positive (nose-down) at $\alpha = 13^o$. This coincides with the time when negative pressure peak associated with the primary vortex travels beyond the quarterchord about which the moment is being measured.

9. During the clockwise pitch, C_L on the airfoil continuously decreases, though it remains above the static value until $\alpha = 11^o$.

10. A little later, the primary vortex passes the trailing edge and its influence on the airfoil continuously diminishes.

11. As the airfoil pitches towards the completion of the oscillation cycle, all the parameters discussed above, *i.e.* x_{sep}, C_L and C_m approach their respective values at the beginning of the cycle.

Effects of Increasing k on Dynamic Stall Due to Pitching

Next we have investigated the effects of increasing the reduced frequency from $k = 0.6$ to 0.9 and 1.2 on the characteristics of dynamics stall on NACA 0012 pitching about its midchord between $\alpha = 6^o$ and 18°. Our major findings are:

1. The propagation speed of the separation point from the trailing edge to the leading edge slows as the reduced frequency increases. Thus the onset of stall is delayed at a higher reduced frequency.

2. The slope of $C_L - \alpha$ curve increases with increasing reduced frequency during the first half of the oscillation cycle.

3. The inception of the primary vortex is delayed (in angular sense) with increasing frequency.

4. Higher peak velocities and velocity gradients are reached in the vicinity of the leading edge as the reduced frequency increased.

5. The separation point penetrates closer to leading edge at a higher reduced frequency.

6. The strength of the primary vortex increases with increasing frequency.

7. The average streamwise speed of the vortex decreases when the reduced frequency is increased.

8. As the reduced frequency increases, the separation point movement towards the trailing edge during the clockwise pitch (reattachment) is inhibited (slowed).

9. The peak positive (nose down) moment attained during a cycle of oscillation increased with increasing frequency. No such pattern was seen in the peak negative moment. The occurance of the latter effect was because of the time of formation and movement of the primary vortex.

10. At $k = 1.2$, two primary vortices could be observed on the airfoil for a significant part of the oscillation cycle.

Effect of the Pivot Location on Dynamic Stall Characteristics

Next, we calculated the effects of moving the pivot from $x_0/c = .50$ to $x_0/c = .25, .75$ on the development of dynamic stall on the airfoil. Our calculations showed that:

1. The separation point movement towards the leading edge is accelerated as the pivot is moved closer to the leading edge and away from the trailing edge.

2. The peak negative pressure and velocity attained near the leading edge increase with increasing upstream-distance of the pivot from the trailing edge.

3. Both of the above results can qualitatively be predicted by analyzing the linear potential flow around an airfoil with smooth leading edge, pitching about various pivots. This analysis leads to the definition of "effective angle of incidence" on a pitching airfoil.

4. As the pivot is moved farther upstream from the trailing edge, the amplitude of separation point excursions from the trailing edge becomes larger.

5. The inception of the primary vortex occurs earlier, strength of the vortex increases and the average streamwise velocity of the vortex decreases when the pivot is moved closer to the leading edge from behind.

6. The peak C_L reached during a cycle of oscillation increases as the pivot moves

closer to the leading edge and away from the trailing edge.

7. Thus, increasing the reduced frequency and moving the pivot closer to the trailing edge, both cause a delay in dynamic stall. But they have opposite effects on $C_{L_{max}}$, the former results in improved $C_{L_{max}}$ whereas the latter leads to a decreased $C_{L_{max}}$.

Dynamic Stall Due to Heaving Oscillations

Finally we have determined the dynamic stall characteristics of NACA 0012 oscillating sinusoidally in heave at constant nominal angle of incidence. Though the nominal angle of incidence on the airfoil remains constant, the heaving velocity of the airfoil causes its effective incidence or "equivalent angle of incidence, α_{eq}" to change resulting in dynamic stall. The definition of α_{eq} provides a basis for comparing the evolution of the flow features on a heaving airfoil with those on a pitching airfoil. We have used $k = 0.6$, $\alpha_{eq} = 12^o + 6^o \sin(\omega t)$ for investingating the heaving case. We compared this heaving case to the pitching problem with pivot at midchord. Our calculations and comparisons indicate that:

1. The separation point on the heaving airfoil moves towards the leading edge, during the early part of the oscillation cycle (when α is increasing from 6° to 12°), more rapidly than on the pitching airfoil.

2. During the first half of the cycle (*i.e.* when α is increasing) the slope of the $C_L - \alpha$ curve is lower for the heaving airfoil than it is for the pitching airfoil.

3. The $C_{L_{max}}$ attained by the heaving airfoil is lower than that attained by the pitching one.

4. The trends in all of the above mentioned results were qualitatively deduced from linear potential flow analysis.

5. The process of stalling, *i.e.* the abrupt jump of the separation point from close to trailing edge to the vicinity of leading edge, is less precipitous on the heaving airfoil.

6. The onset of dynamic stall is delayed on the heaving airfoil compared to that on the pitching airfoil.

7. The moment stall also is less abrupt on the heaving airfoil. The peak negative (nose-up) moment calculated on the heaving airfoil was smaller in magnitude.

8. The strength of the primary vortex on the heaving airfoil was smaller.

9. Even though the above conclusions are so far referred only to the pitching case with midchord pivot, our investigation into the effects of the pivot location on dynamic stall allows us to state that these conclusions will hold for all pivots located upstream of midchord and downstream of leading edge. No generalizations, however, can be

drawn for pivots downstream of midchord.

Effects of Reduced Frequency on Heave Induced Dynamic Stall

The effects of increasing the reduced frequency on dynamic stall characteristics of a heaving airfoil are qualitatively same as those on a pitching airfoil.

7.2 Recommendations for Future Work

The present method can be used without any modifications for analyzing the dynamic stalling of an airfoil oscillating in lunge. In fact, the present method can be used for any combination of linear and rotational motion of the airfoil as long as the magnitude of the reduced frequency of the motion allows splitting the boundary layer flow into "Prandtl" and "Stokes" flows. Analysis of viscous response of a closed body to a passing vortical structure, which constituted a part of the present work, can be carried out using the present method.

Apart from the fact that there exist many practical situations which can be modeled and readily solved by the present method, the scope of the present method can be increased to include such effects of turbulence as flow transition and formation of the leading edge bubble and flow regimes at very high reduced frequencies.

7.2.1 Extending the Range of Applicable Reduced Frequency

The applicability of the present method is limited to reduced frequencies above 0.55. This limitation can be removed by augmenting the method with several of the semi-analytic solutions available for integrating the unsteady boundary layer equations for low reduced frequencies [73, 25, 68]. A particularly elegant and complete integration is being carried out by McCune, [58].

The method can also be extended to very high reduced frequencies, *i.e.* $k \geq 2$. Our calculations indicate that in this range of the reduced frequency there will be two or more primary vortices present on the surface of the airfoil throughout the oscillation cycle. The interaction of these vortices with one another becomes important as it can have significant influence over the forces and moments on the airfoil.

It appears that special attention should be placed on modeling the primary vortices and the shear layers, as our simple discrete vortex model of the shear layer was becoming inadequate as k was approaching 1.5 when the distance between the primary vortices was roughly equal to their streamwise width. At such high frequencies, we observed that the primary vortex, composed of several discrete vortices, was becoming distorted into an oval shaped structure as their streamwise width started to grow much faster than their dimension perpendicular to the freestream. It appears that some merging-like interaction starts to occur at around $k = 2$. It is not clear to us, which

of these observed features are due to inadequacies in our models and which are true flow features.

It was also observed that as the reduced frequency increases, the separation point propagation towards the leading edge is delayed. Also, the movement becomes more and more abrupt with increasing frequency. At the same time, the separation point stays in the leading edge vicinity for longer (in angular sense) with increasing frequency and then towards the end of the cycle, jumps abruptly to the trailing edge. It appears from our calculations that in the limit of very large reduced frequency, the separation point stays at the trailing edge for all of the first half of the oscillation cycle, jumps abruptly to the leading edge, stays there for all of the rest of the cycle and jumps abruptly back to the trailing edge. Then, it would be efficient and accurate to model the flow as fully potential with imposed shedding from trailing and leading edges as mentioned above. The subsequent evolution of the free shear layers can be modeled by using a suitable method from the several available ways [71]. Such an analysis should enable one to handle reduced frequencies well above $k = 2$.

7.2.2 Including the Effects of Turbulence and Leading Edge Bubble

The effects of turbulence and flow transition can be incorporated into the present method by using a suitable turbulence model. For a discussion on turbulence models please see [82]. However, flow transition into turbulence has two primary effects on the flow in the dynamic stall context. The first is that it allows for flow reattachment making it possible the formation of a leading edge bubble. The second is that it delays the ultimate separation of the boundary layer (after transition) helping the airfoil retain more lift. The second of these two effects can be included without resorting to turbulence modeling by developing an unsteady version of Stratford's [67] turbulent separation condition. This subject was discussed in some detail by [30].

The formulation of the conditions which control the formation of the leading edge bubble *i.e.* conditions for flow reattachment, however, may require the introduction of a turbulence model and a prescribed location for the onset of transition. In steady flows condition for the existence of a "closed" bubble *i.e.* a closed streamline, can be formulated. It requires that the total pressure loss of a fluid particle traveling on this streamline when the particle path is tangential to the wall be equal to the total pressure gained by the particle during the rest of its journey along the closed

streamline. In unsteady flows however, streamlines are neither closed nor fixed, there is flow across a streakline and there is constant entrainment into a "bubble", however defined. We are currently working on this subject.

Bibliography

[1] Abbott, I.H. and von Doenhoff, A.E., "Theory of Wing Sections", Dover Publications, 1959

[2] Acharya, M. and Metwally, M., "The Unsteady Pressure Field and Vorticity Production at the Suction Surface of a Pitching Airfoil", AFOSR Workshop on Physics of Forced Unsteady Separation, 1990.

[3] Ashley, H. and Landahl, M.T., "Aerodynamics of Wings and Bodies", Dover Publications, 1965.

[4] Batchelor, G.K., "A Proposal Concerning Laminar Wakes Behind Bluff Bodies at Large Reynolds Number", Journal of Fluid Mechanics, April 1956.

[5] Batchelor, G.K., "Fluid Dynamics", p321-331, Cambridge University Press, 1978.

[6] Beddoes, E.G., "Experiments on Airfoils in Unsteady Motion", USAAL TR-76-24, 1976.

[7] Bender, C.M. and Orszag, S.A., "Advanced Mathematical Methods for Scientists and Engineers", McGraw-Hill Publications, 1978.

[8] Bisplinghoff, R.L., and Ashley, H., "Principles of Aeroelasticity", John Wiley and Sons, Inc., 1955.

[9] Brown, S.N. and Stewartson, K., "Laminar Boundary Layers", Annual Review of Fluid Mechanics, 1972.

[10] Carr, L.W., "Dynamic Stall Progress in Analysis and Prediction", AIAA Paper 85-1769CP, 1985.

[11] Carrier, G.F. and Pearson, C.E., "Partial Differential Equations", Academic Press, 1988.

[12] Carta, F. O., "Prediction of Rotor Instability at High Forward Speeds - vol. 3, Stall Flutter". USAAVLABS TR-68-18C, 1969.

[13] Carta, F. O., "Unsteady Normal Forces on an Airfoil in a Periodically Stalled Inlet Flow", Journal of Aircraft, vol. 4, no. 5, 1967.

[14] Carta, F. O., "A Comparison of the Pitching and Plunging Response of an Oscillating Airfoil", NASA Contractor Report, CR3172, Oct. 1979.

[15] Crimi, P., "A Method for Analyzing Dynamic Stall of Helicopter Rotor Blades", NASA CR-2009, 1972.

[16] Crimi, P., "Analysis of Stall Flutter of a Helicopter Rotor Blade", AIAA Paper no. 73-403, 1973.

[17] Curle, N. and Skan, s.W., "Approximate Methods for Predicting Separation Properties of Laminar Boundary Layers", Aeronautical Quarterly, vol. 8, 1957.

[18] Ericsson, L., "Unsteady Airfoil Stall", NASA CR-66787, 1969.

[19] Dean, W.R., "A Note on the Motion of Liquid near a Position of Separation", Proceedings of Cambridge Philosophical Society, no. 46, 1950.

[20] Drela, M., "Unsteady Airfoil Flow Prediction Method", CFDL TR-90-1, M.I.T., Jan. 1990

[21] Ericsson, L. and Reding, J.P., "Fluid Dynamics of Unsteady Separated Flow, Part II, Progresses in Aerospace Sciences, vol. 24, 1987.

[22] Francis, M.S. and Keese, J.E., "Airfoil Dynamic Stall Performance with Large Amplitude Motions", AIAA Journal, 1985, vol. 23, no. 11.

[23] Freymuth, P., "Further Experimental Evidence of Vortex Splitting", JFM, vol. 152, pp289-299, 1985.

[24] Fukushima, T. and Dadone, L. U., "Comparison of Dynamic Stall Phenomena for Pitching and Vertical Translation Motions", NASA Contractor Report, CR2793, July. 1977.

[25] Geis, T., "Integration of Unsteady Laminar Boundary Layer Equations", Translated from German, *Z. angew. Math. Mech.*, 1959, vol. 36.

[26] Geissler, W., "Unsteady Boundary Layer Separation on Airfoils Performing Large Amplitude Oscillations - Dynamic Stall".

[27] Geissler, W., "Unsteady Laminar Boundary Layer Calculation on Oscillating Configurations Including Backflow, Part I&II", NASA TM-84319, 1983.

[28] Ghia, U. and Ghia, K.N., "Analysis and Control of Low-Speed Forced Unsteady Flow", ASME Symposium on Nonsteady Fluid Dynamics, June 1990.

[29] Gibson, W.E., "Unsteady Laminar Boundary Layers, Ph. D. Thesis, M.I.T., Department of Mathematics, 1957.

[30] Gioulekas, A., "An Alternative to the Kutta Condition for High Frequency, Separated Flows", Ph. D. Thesis, M.I.T., Department of Aeronautics and Astronautics.

[31] Goldstein, S., "On Laminar Boundary Layer Flow near a Position of Separation", Quarterly Journal fo Aeronautical Sciences, no. 15, 1948.

[32] Halfman, R. et. al., "Evaluation of High Angle of Attack Aerodynamic Derivative Data and Stall Flutter Prediction Techniques, NACA TN 2533, Nov. 1951.

[33] Ham, N.D., Torsional Oscillation of Helicopter Blades Due to Stall", Journal of Aircraft, vol. 3, no. 3, 1966.

[34] Ham, N.D., Aerodynamic Loading on a Two-Dimensional Airfoil During Dynamic Stall", AIAA journal, vol. 6, no. 10, 1968.

[35] Helin, H.E. and Walker, J.M., "Interrelated Effects of Pitch Rate and Pivot Point on Airfoil Dynamic Stall", AIAA Paper 85-0130, 1985.

[36] Howarth, L., "The Theoretical Prediction of teh Lift Coefficient for a Thin Elliptic Cylinder", Proceedings of the Royal Society, ser. A, vol. 149, 1935.

[37] Jumper, E.J. *et. al.*, "The Effect of Pitch Location on Dynamic Stall", ASME Forim on Unsteady Flow Separation, 1987.

[38] Karamcheti, K., "Principles of Ideal Fluid Aerodynamics", John Wiley and Sons, Inc., 1966

[39] von Kárman, T. and Sears, W.R., "Airfoil Theory for Non-Uniform Motion", Journal of Aeronautical Science, vol. 5, no. 10, 1938.

[40] Katz, J. and Plotkin, L.,"Low-Speed Aerodynamics", McGraw Hill & Co., 1991

[41] Katz, J., "A Discrete Vortex Method for the Non-Steady Separated Flow Over an Airfoil", Journal of Fluid Mechanics, vol. 102, 1981.

[42] Koochesfahani, M.M. and Smiljanovski, V., "Effect of Initial Acceleration on the Development of the Flow Field of an Airfoil Pitching at Constant Rate", AFOSR Workshop on Physics of Forced Unsteady Separation, 1990.

[43] Koromilas, C.A. and Telionis, D.P., "Unsteady Laminar Separation, an Experimental Study", Journal of Fluid Mechanics, vol. 97, part 2, 1980.

[44] Kreyszig, W.E., "Advanced Engineering Mathematics", Wiley Eastern Publications, 1972.

[45] Kuethe, A.M. and Chow, C-y, "Foundations of Aerodynamics", John Wiley & Sons, 1986.

[46] Lamb, Sir Horace, "Hydrodynamics", Dover Publications, 1945.

[47] Landau, L.D. and Lifshitz, E.M., "Fluid Mechanics", Pergamon Press, 1959.

[48] Lighthill, M.J., "The Response of Laminar Skin Friction and Heat Transfer to Fluctuations in the Stream Velocity, Proceedings of the Royal Society of Aeronautics, Series A, vol. 224, 1953.

[49] Liiva, J., et al., "Two Dimensional Tests of Airfoils Oscillating Near Stall", USAAL TR-68-13, 1968.

[50] Lin, C.C., "Motion in the Boundary Layer with a Rapidly Oscillating External Flow", 9th International Congress of Applied Mechanics, 1956, p155-167.

[51] Lorber, P.F., and Carta, F.O., "Airfoil Dynamic Stall at Constant Rate Pitch at High Reynolds Number" AIAA Paper 87-1329, 1987.

[52] Lorber, P.F., and Carta, F.O., "Unsteady Stall Penetration Experiments at High Reynolds Number", UTRC Report R87-956939-3, 1987.

[53] Mathioulakis, D.S. and Telionis, D.P., "Pulsating Flow over an Ellipse at an Angle of Attack", Journal of Fluid Mechanics, vol. 201, 1989.

[54] McCroskey, L.W., "Dynamic Stall Experiments on Oscillating Airfoils", AIAA Journal, vol. 14, no. 1, 1976.

[55] McCroskey, L.W., "Unsteady Airfoils", Annual Review of Fluid Mechanics, vol. 14, p285-311, 1982.

[56] McCroskey, L.W., "Some Current Research in Unsteady Fluid Dynamics", Journal of Fluids Engineering, vol. 99, p8-38, 1977.

[57] McCune, J.E., *et al*, "Nonlinear Aerodynamics in Severe Maneuver", AIAA Journal, p385-393, March 1990.

[58] McCune, J.E., Professor of Aeronautics and Astronautics, M.I.T., Private Communication.

[59] Mehta, U.B., "Dynamic Stall of an Oscillating Airfoil", Paper no. 23, AGARD CP-227, 1977.

[60] Mezaris, T.B. *et al*, "Separation and Wake of Pulsating Flow, Philosophical Transactions of Royal Society of London, series A, 1987.

[61] Milne-Thompson, L.M., "Theoretical Hyrodynamics", Dover Publications, 1974.

[62] Mondoloni, S.L., "Numerical Method for Modeling Wings with Sharp Edges Maneuvering at High Angles of Attack", Ph.D. Thesis, M.I.T., Department of Aeronautics and Astronautics, 1993.

[63] Morawetz, C., "On the Nonexistence of Continuous Transonic Flow Past Profiles, Coomunications of Pure & Applied Mathematics, vol. 9, 1956.

[64] Ono, K., "Numerical Study onthe Dynamic Stall Process of a NACA 0012 Airfoil", AIAA Paper, 1985.

[65] Patay, S.A., "Leading Edge Separation on an Airfoil Osciallating During Dynamic Stall", M.I.T. ASRL TR-156-1, 1969.

[66] Rainey, A.G., "Measurement of Aerodynamic Forces for Various Mean Angles of Attack on an Airfoil Oscillating in Pitch and on Two Finite-Spin Wings Oscillating in Bending with Emphasis on Damping in the Stall", NACA TR 1305, 1957.

[67] Rosenhead, L., "Laminar Boundary Layers", Dover Publications, 1966.

[68] Rozin, L. A., "Approximate Integration of the Unsteady Boundary Layer Equations", Translated from Russian, NASA Tech. Trans., F-22.

[69] Rumsey, C.L. and Anderson, W.K., "Some Numerical and Physical Aspects of Unsteady Navier-Stokes Computations over Airfoils Using Dynamic Meshes", AIAA Paper 88-0329, 1988.

[70] Sankar, N.L. and Tassa, Y., "Reynolds number and Compressibility Effects on Dynamic Stall of a NACA0012 Airfoil", AIAA Paper, 1980.

[71] Sarpkaya, T., "Computational Methods With Vortices", ASME Journal of Fluids Engineering, vol. 111, 1989.

[72] Schlitching, H., "Boundary Layer Theory", McGraw-Hill Publications, 1979.

[73] Schuh, H., "Calculation of Unsteady Boundary Layers in Two-dimensional Laminar Flow", Translated from German, *Z. Flugwiss.*, 1953, vol. 1.

[74] Sears, W.R. and Telionis D.P., "Boundary Layer Separation in Unsteady Flow", SIAM Journal of Applied Mechanics, 1975, vol. 18.

[75] Sears, W.R., "Some Recent Developments in Airfoil Theory", Journal of Aeronautical Science, May 1956, vol. 23, no. 5.

[76] Sears, W.R., "Unsteady Airfoils with Boundary Layer Separation", AIAA journal, vol. 14, no. 2, 1976.

[77] Shames, I.H., "Dynamics of Rigid Bodies", Wiley Eastern Publications, 1969.

[78] Sisto, F., "Stall-Flutter in Cascades", Journal of Aeronautical Sciences, vol. 20, no. 9, Sept. 1953.

[79] Stratford, B.S., "Flow in the Laminar Boundary Layer near Separation, Report no. 3002, Aeronautical Research Council of London, 1954.

[80] Strickland, J.H. and Graham, G.M., "Force Coefficients for a NACA 0015 Airfoil Undergoing Constant Pitch Rate Motions", AIAA Paper 81-1289, 1981.

[81] Sychev, V.V., "Laminar Separation", Translation from Russian Original, 1972.

[82] Telionis, D.,"Unsteady Viscous Flows", Springer-Verlag, 1981.

[83] Tavares, T.S., "Aerodynamics of Maneuvering Slender Wings with Leading Edge Separation", Ph. D. Thesis, M.I.T., Department of Aeronautical and Astronautical Engineering, 1990.

[84] Theodorsen, T., "Conformal Mapping of an Arbitrarily Shaped Simply Connected Body into a Circle", NACA TN-2864, Jan. 1944

[85] Tijdeman, H. and Seebass, R., "Transonic Flow Past Oscillating Airfoils", Annual Review of Fluid Mechanics, vol. 12, 1980.

[86] Vaczy, C. "Unsteady Separated Flow Fields on a NACA 0012 Airfoil", S.M. Thesis, M.I.T., Department of Aeronautics and Astrionautics, 1984.

[87] Visbal, M.R., "Investigation of Flow Structure Around a Rapidly Pitching Airfoil", AIAA Journal, vo. 27, no. 8, 1989.

[88] Visbal, M.R. and Shang, G.H., "Dynamic Stall of Constant Rate Pitching Airfoil", AIAA Journal of Aircraft, 1990.

[89] Walker, J. et al., "An Experimental Investigation of an Airfoil Undergoing Large Amplitude Pitching Motion", AIAA Paper-0039, 1985.

[90] White, F.M., "Viscous Fluid Flow", McGraw-Hill, Inc, 1974.

[91] Wo, A.M., "Characteristics of Airfoils in an Oscillating External Flow at Low Reynolds Numbers", Ph.D. Thesis, M.I.T., 1990.

[92] Woods, L.C., "Aerodynamic Forces on an Oscillating Airfoil Fitted with a Spoiler", Proceedings of the Royal Society, series A, vol. 239, 1957.

[93] Wu, J.C. et al., "Unsteady Aerodynamics of Rapidly Pitching Airfoils", AIAA Paper-86-1105, 1986.